Description and evaluation of the Atmospheric Radionuclide Transport Model ARTM

Dissertation
zur Erlangung des Grades
„Doktor der Naturwissenschaften“

am Fachbereich Physik, Mathematik und Informatik
der Johannes Gutenberg-Universität
in Mainz

Robert Hanfland

geb. in Kempten

München, den 6. Dezember 2023

1. Berichterstatterin: Prof. Christiane Voigt
2. Berichterstatter: Prof. Holger Tost
2. Berichterstatter: Prof. Dominik Brunner

Datum der mündlichen Prüfung: 18. März 2024

Kurzfassung

Trotz Filtertechniken emittieren kerntechnische Anlagen kleine Mengen von radioaktiven Spurenstoffen in die Luft, deren Einfluss auf die Umwelt in Quellnähe nur schwer detailliert gemessen werden kann. Daher sind schnelle und effiziente Ausbreitungsmodelle nötig, um die Ausbreitung von Spurenstoffen zu überwachen und vorherzusagen. In Deutschland wurde dafür das lagrangesche Atmosphärisches Radionuklid Transport Model (ARTM) entwickelt. Es simuliert die Ausbreitung von Ableitungen aus kerntechnischen Anlagen typischerweise bis zu einer Entfernung von 20 km innerhalb der planetaren Grenzschicht. Solche Transportmodelle müssen sorgfältig validiert werden um sicher zu stellen, dass sie die Ausbreitung von Spurenstoffen wirklichkeitsgetreu abbilden.

Die vorliegende Arbeit beschreibt und erweitert das Model ARTM und zeigt eine Auswertung der dreidimensionalen Ausbreitungseigenschaften von Spurengasen. In einer Sensitivitätsstudie wird der Einfluss von Stabilitätsklasse, Rauhigkeitslänge, Verschiebungshöhe, Quellhöhe und Spurenstofftyp auf die dreidimensionale Ausbreitung der Abgasfahne analysiert. Zudem wird der „well-mixed“ Zustand von fünf Turbulenzmodellen, den Standardmodellen von ARTM 2.8.0 und 3.0.0, einem alternativen eingebauten und zwei weiteren neu implementierten Modellen untersucht. Flugzeuggestützte CO_2 Messungen in der Nähe des Braunkohlekraftwerks Bełchatów (Polen) von der CoMet Messkampagne 2018 erlauben die Bewertung der Modelergebnisse unter sehr instabilen Grenzschichtbedingungen. Ein Modellvergleich mit numerischen Wettervorhersage- und Large-Eddy-Modellen erweitert die Untersuchung auf leicht instabile atmosphärische Bedingungen.

Die Ergebnisse zeigen, dass die Stabilitätsklasse, als Maß für die atmosphärische Stabilität, den größten Einfluss auf die Simulationsergebnisse hat und einen signifikanten Beitrag zur Unsicherheit der Konzentrationsverteilung atmosphärischer Spurengase liefert. Die Verwendung von gemessenen Obukhov-Längen verbessert die Genauigkeit erheblich, da damit die Stabilität als kontinuierliche Größe anstelle einer klassifizierenden parametrisiert werden kann. Das Turbulenzmodell von ARTM 3.0.0 weist die größte Abweichung zum „well-mixed“ Zustand von ca. 20% auf. Alle simulierten Konzentrationen sind in derselben Größenordnung wie die flugzeuggestützten in situ Messdaten. Die Turbulenzeinstellungen von ARTM 2.8.0 und 3.0.0 unterschätzen die Abgasfahnenbreite um bis zu 50%. Die drei anderen Turbulenzmodelle weisen deutlich geringere Abweichungen auf. Im Gegensatz zu sehr instabilen atmosphärischen Bedingungen liefert das Standardturbulenzmodell von ARTM 2.8.0 bei schwach instabiler Atmosphäre vergleichbare Ergebnisse wie die anderer Transportmodelle. Die Ergebnisse dieser Arbeit können dazu beitragen, die Genauigkeit der mit ARTM simulierten Abgasfahnen bei sehr instabilen atmosphärischen Bedingungen durch die Wahl geeigneter Turbulenzmodelle zu verbessern.

Abstract

Despite of filtering techniques, nuclear facilities emit small amounts of radioactive tracers to the air. Detailed measuring of the effects of such discharges to the environment in the vicinity of the emitter covering an area of several square kilometres is very challenging. Fast and efficient atmospheric dispersion models are thus required to monitor and predict atmospheric dispersion of trace species in the vicinity of nuclear facilities. In Germany, the Lagrangian Atmospheric Radionuclide Transport Model (ARTM) was designed for this purpose. It simulates the dispersion of discharges from nuclear facilities typically up to 20 km distance within the planetary boundary layer. Such transport models have to be validated carefully to make sure that they simulate tracer dispersions comparable to reality.

This study shows the description and extension of ARTM as well as the analysis of the three-dimensional dispersion properties and their evaluation. In a sensitivity study, the effects of stability class, roughness length, zero-plane displacement, source height and tracer type on the three-dimensional plume dispersion are analysed. Furthermore, the dispersion of five turbulence models, the default turbulence models of ARTM 2.8.0 and ARTM 3.0.0, one alternative built-in turbulence model of ARTM and two further turbulence models newly implemented into ARTM are studied. Airborne CO_2 observations in the vicinity of the lignite power plant Bełchatów, Poland, during the CoMet campaign in 2018 allow to evaluate the model performance under unstable boundary layer conditions. An intercomparison of ARTM with numerical weather prediction and large-eddy simulation models extend the investigation to slightly unstable atmospheric conditions.

The results show that the stability class, as a parametrisation of the atmospheric stability, causes the largest impact and hence the largest uncertainty in the simulation results. The usage of measured Obukhov lengths substantially improves the accuracy because of its continuous stability parametrisation. The turbulence model of ARTM 3.0.0 show the largest deviation from the well-mixed state by up to approx. 20%. All simulated mixing ratios are in the same order of magnitude as the airborne in situ data. The turbulence setups of ARTM 2.8.0 and 3.0.0 underestimate the plume widths by up to 50%. The three other turbulence models agree better with the observations simulating comparable plume widths. The intercomparison reveals that, in contrast to very unstable boundary layer conditions, the turbulence model of ARTM 2.8.0 delivers comparable results to those of the other transport models under slightly unstable conditions. The results of this work may help to improve the accuracy of plumes simulated by ARTM representing real plumes in very unstable atmospheric conditions by the selection of distinct turbulence models.

Publications

Results of the presented work have been published in:

Hanfland, R., M. Pattantyús-Ábrahám, C. Richter, D. Brunner, and C. Voigt (2022). "The Lagrangian Atmospheric Radionuclide Transport Model (ARTM) - Development, Description and Sensitivity Analysis". In: *Air Qual. Atmos. Health*. DOI: 10.1007/s11869-022-01188-x.

Hanfland, R., D. Brunner, C. Voigt, A. Fiehn, A. Roiger, and M. Pattantyús-Ábrahám (2023). "The Lagrangian Atmospheric Radionuclide Transport Model (ARTM) - Sensitivity studies and evaluation using airborne measurements of power plant emissions". In: *EGUsphere [preprint]* 2023, pp. 1–35. DOI: 10.5194/egusphere-2023-245.

Brunner, D., G. Kuhlmann, S. Henne, E. Koene, B. Kern, S. Wolff, C. Voigt, P. Jöckel, C. Kiemle, A. Roiger, A. Fiehn, S. Krautwurst, K. Gerilowski, H. Bovensmann, J. Borchardt, M. Galkowski, C. Gerbig, J. Marshall, A. Klonecki, P. Prunet, R. Hanfland, M. Pattantyús-Ábrahám, A. Wyszogrodzki, and A. Fix (2023). "Evaluation of simulated CO2 power plant plumes from six high-resolution atmospheric transport models". In: *Atmos. Chem. Phys.* 23.4, pp. 2699–2728. ISSN: 1680-7324. DOI: 10.5194/acp-23-2699-2023.

Contents

Kurzfassung iii

Abstract v

Publications vii

1 Introduction 1

2 Atmospheric dispersion in the planetary boundary layer 7
2.1 Introduction to the planetary boundary layer . . . 7
2.1.1 The vertical structure of the planetary boundary layer . . . 8
2.1.2 Atmospheric turbulence . . . 9
2.1.3 The vertical wind profile in the planetary boundary layer . . . 12
2.2 Introduction to dispersion modelling . . . 19
2.2.1 A brief history of dispersion modelling of air pollutants and radionuclides in the atmosphere . . . 19
2.2.2 Modelling the dispersion of pollutants and radionuclides . . . 21
2.2.3 Overview of the types of atmospheric dispersion models . . . 22
2.2.4 Lagrangian particle dispersion models (LPDMs) . . . 24
2.3 Model evaluation . . . 27

3 The Atmospheric Radionuclide Transport Model (ARTM) 29
3.1 The wind field model TALdia . . . 30
3.1.1 The boundary layer model of TALdia . . . 30
3.1.2 Wind field modelling . . . 34
3.1.3 Boundary conditions . . . 36
3.1.4 Parametrisation of atmospheric stability . . . 36
3.1.5 Coordinate system . . . 38
3.2 The particle dispersion model . . . 39
3.2.1 The transport . . . 39
3.2.2 Particle initialisation and boundary conditions . . . 40

3.2.3 The plume rise . . . 40
3.2.4 Sedimentation, dry and wet deposition . . . 42
3.2.5 Radioactive decay . . . 44
3.2.6 Activity concentration distribution . . . 44
3.2.7 Activity deposition rate distribution . . . 45
3.2.8 γ-cloud shine . . . 45
3.2.9 Sample Error . . . 47

4 The influence of input parameters and turbulence models 53
4.1 Dependence of simulation results on input parameters . . . 53
4.1.1 Methods for the quantification of sensitivity . . . 54
4.1.2 Simulation setup for the sensitivity analyses . . . 57
4.1.3 Evaluation of parameter sensitivity . . . 61
4.2 The mixing properties of turbulence models under unstable conditions 73
4.2.1 Description of the turbulence models . . . 73
4.2.2 Simulation setup for the well-mixed condition test . . . 78
4.2.3 Evaluation of the turbulence models . . . 78

5 Evaluation of ARTM 87
5.1 Comparison of ARTM simulation results with observations . . . 87
5.1.1 Observational data . . . 88
5.1.2 Simulation setups for the model evaluation . . . 90
5.1.3 Evaluation of the three-dimensional dispersion of simulated plumes . . . 94
5.2 Comparison of ARTM to five other atmospheric transport models . 109
5.2.1 Observational data and modelling protocol . . . 110
5.2.2 ARTM simulations . . . 111
5.2.3 Model performance assessment . . . 111
5.2.4 Results and discussion . . . 112

6 Summary 117

7 Outlook 121

List of abbreviations 125

Bibliography 127

Declaration of authenticity 149

Author contributions 151

Acknowledgments/Danksagung **153**

Curriculum vitae/Lebenslauf **155**

Chapter 1

Introduction

Amid the anthropogenic climate change nuclear power plants are widely seen as a possibility of generating carbon dioxide (CO_2) neutral and continuously available electrical energy. Despite the nuclear phase-out of some countries in Europe, the number of countries supporting this technique is still large. In 2021, about 10% of the electrical energy worldwide was provided by 436 nuclear reactors in 32 countries. In the same year, ten reactors were permanently shut down while six new reactors were connected to the grid and 56 reactors were under construction (Gospodarczyk 2022).

Besides the benefits of energy generation from nuclear reactors, there are major concerns about hazardous drawbacks originating from such facilities. This touches not only the fear of nuclear accidents and the largely unresolved questions of long-term storage of nuclear wastes but also the discharges during routine operation or decommissioning. Under routine operation, the process of controlled nuclear fission generates radioisotopes that are spread within the reactor building. During decommissioning, contaminated aerosols are produced due to the cutting and the demolition of contaminated metal or concrete. In both cases, contaminated air is treated using filter techniques and released via ventilation stacks to the atmosphere. Despite the filtering small amounts of radioisotopes may remain in the emitted air.

The monitoring of radioisotopes at the ventilation stack is common practice and obligatory in most countries. However, it is very challenging to quantify the impact of these emissions on the environment in the vicinity of the power plant based on observations. The only alternative to obtain comprehensive local and temporal information about the immissions is from atmospheric dispersion simulations (De Visscher 2014). To ensure public safety, governments all over the world enacted national regulations to use atmospheric dispersion models for monitoring the dispersion of discharges from nuclear facilities to the air.

In the atmosphere the dispersion of tracers largely depends on random motions

of the air and its molecules. These diffusive effects are referred to as molecular diffusion and turbulent motion, respectively. Molecular diffusion is usually neglected in atmospheric dispersion because of its small range compared to turbulent diffusion. Particularly in the planetary boundary layer, which is strongly influenced by interactions with the Earth's surface, the atmosphere is usually turbulent. The concentrations of pollutants thus vary depending on time and location even when the pollution source and the weather conditions are constant. Accurately representing the large number of factors influencing the dispersion is a major challenge for air dispersion models. The result of an atmospheric dispersion simulation can not be expected to correspond in all details to the real-world dispersion (De Visscher 2014).

Nevertheless, it is important that any dispersion model is a sufficiently accurate representation of its corresponding real-world system. This can be tested in a validation process, which often consists of two main parts: i) a sensitivity analysis; and ii) a comparison of simulation results with measurements. The sensitivity analysis investigates the change of the simulation results with variations of the input parameters (Kleijnen 1995). For a simulation model it is important to know whether an observable or unobservable input parameter critically influences the model outcome. The sensitivity analysis shows which input parameters are the most sensitive or important ones. This information can be used to estimate the contribution of uncertainties in the input parameters to the simulation result's uncertainty. The application of an appropriate sensitivity analysis method is a key issue and depends on the complexity of the simulation model. The application of only one analysis method may result in wrong conclusions (Kleijnen 1995).

The comparison of simulation and observations can show whether a model simulates the real world counterpart sufficiently accurately. Following De Visscher (2014), an atmospheric dispersion model successfully simulates its real-world system when the following three criteria are fulfilled:

1. The simulated and the actual hourly average concentrations must not deviate by more than a factor of two for most of the time.

2. The long-time averaged concentrations of the simulation and the observations have to be close.

3. The distributions of the ranked concentration values from simulation and observations have to be very similar when ranking the concentration values at different locations and times from lowest to highest, respectively. It is not required that the simulations and observations at corresponding positions and times have to have the same rank.

This requires the availability of appropriate high quality measurement data sets, which can be an issue. This requirement does not only account for the data that

is compared with simulation results but also for the data that is used to generate input parameters for a model (Kleijnen 1995).

The sensitivity analysis uses the variation on model result characteristics (or target quantities), which indicate the dispersion of tracers. Also, the comparison of simulation results with observations close to the surface of the earth may not be sufficient to draw conclusions about how well the model simulates the dispersion. A data set used for comparison should ideally include measurement points from the entire extent of the modelled atmosphere to cover the dispersion at larger distances from the surface, too.

In this work, the Atmospheric Radionuclide Transport Model (ARTM) is described and its results are analysed and evaluated against measurements. ARTM is a Lagrangian particle dispersion model primarily designed for the dispersion simulation of radionuclides from nuclear facilities under routine operation in the planetary boundary layer at the micro-scale to the meso-γ-scale (approx. 0.5 km to 20 km) (Hanfland et al. 2022). ARTM is in operation at the Federal Office for Radiation Protection and other authorities of Germany for the estimation of exposure of the population for regulatory and authorisation purposes. Over the last 15 years, ARTM was continually developed into a mature model system, but for further improvements more detailed knowledge about the performance of the model is needed. With this work I intend to fill some of these knowledge gaps and to demonstrate possible improvements. First, there is only insufficient information about which input parameters significantly affect the simulation results and which input parameters are thus of special importance. Second, the data base of the validation of ARTM is insufficient. The discharges of nuclear facilities under routine operation are typically released via stacks with often large heights. In contrast to this, previous validation attempts focused of the dispersion close to the surface. During this work, I also found that the description of turbulence under unstable atmospheric conditions needs to be improved. Thus, the aims of this work are summarised as: i) sensitivity analysis; ii) the improvement of the description of the turbulent dispersion; and iii) the evaluation against measurements of emissions from power plants.

Hettrich (2017) performed a first sensitivity study on input parameters such as emission strength, source geometry, roughness length and stability class for ARTM. However, the analysis was based on a case study and was restricted to one single receptor location near the surface without considering the whole simulation domain. Note that such one-receptor studies are very sensitive to wind direction changes and in real cases hard to interpret. Since the concentration distribution at the ground is the result of the dispersion within the simulated planetary boundary layer, it is expected that the variation of input parameters does also influence the entire three-dimensional structure of the simulated exhaust plume.

In this work, I extend the sensitivity analysis of Hettrich (2017) from one specific test scenario to a general simulation setup and study the impact of input parameters on the dispersion structure within the entire three-dimensional planetary boundary layer. In addition to the analysis of concentration data, the particle deposition is studied. I analyse which input parameter has the largest influence on simulation results and causes the largest uncertainty if not properly provided for the simulations.

In regulatory practice, the turbulence of the atmosphere is described by using stability classes because of their simplicity. In ARTM, stability classes are translated into associated Obukhov lengths. However, the Obukhov length is a continuous turbulence parameter and its reduction to six classes causes strong discretisation of the possible magnitudes of dispersion in the model and thus leads to higher simulation errors. It is expected that using measured Obukhov lengths for ARTM might increase the accuracy. Therefore, in this work I study the difference on the range of plume volumes when using the continuous Obukhov length instead of stability classes as turbulence parameter.

In ARTM, turbulent fluctuations are modelled by turbulence models. They consist of two sets of turbulence variables describing the wind speed fluctuation and the correlation time scale in all three dimensions. The formulation of these variables is not unique. In literature, a variety of turbulence models have been proposed, which have been derived from measurement data (Panofsky et al. 1977; Hanna 1982; Gryning et al. 1987; Kerschgens et al. 2000; Degrazia et al. 2000). In ARTM, there are four different turbulence models implemented. Originally, the turbulence model described in the guideline VDI 3783 part 8 (2002) was the standard turbulence model of ARTM version 2.8.0. However, Janicke et al. (2011) showed that there are deviations between simulated and observed wind speed fluctuations at several measurement sites under unstable atmospheric conditions. As a consequence of these findings, the initially recommended turbulence model formulation was modified. In 2021, version 3.0.0 of ARTM was released containing a new turbulence model recommended by the recently updated guideline VDI 3783 part 8 (2017).

Until today, simulations of ARTM with the different turbulence models have only been compared with observations close to the ground or up to 200 m height (Janicke et al. 2011; Martens et al. 2012; Hettrich 2017). Thus, it is not known, whether the structure of the dispersed tracers simulates real dispersion plumes correctly at larger heights.

In this work, I used a new data set of high quality airborne in situ CO_2 measurements of an exhaust plume of a large lignite power plant to compare to the tracer dispersion simulation results of three built-in turbulence models of ARTM focusing on the three-dimensional structure of the plumes. I further implemented

two alternative turbulence models to study differences between them and to evaluate which turbulence model simulates the tracer dispersion closest to the measured exhaust plume under very unstable atmospheric conditions.

This work is organised as follows. In chapter 2, an introduction to the planetary boundary layer is given. It starts with a theoretical background of the vertical structure of the planetary boundary layer and a description of the phenomenon of atmospheric turbulence in the planetary boundary layer. This is followed by a brief historical review of atmospheric dispersion modelling including an overview of the main model types and applications focusing on Lagrangian particle dispersion models. Required steps for the validation of Lagrangian particle dispersion models are followed by an overview of the dispersion simulations performed in this work. In chapter 3, I give an extensive description of the physical and mathematical concepts of ARTM. This includes the description of the applied diagnostic wind field model, the general particle transport model and the characteristic features affecting the transport of radionuclides. These are radioactive decay, dry and wet deposition and the estimation of the γ-cloud shine. In chapter 4, I study the influence of input parameters of ARTM on the simulation results. In the following, three built-in and two newly implemented turbulence models are presented and their mixing abilities under very unstable atmospheric conditions are investigated. In chapter 5, I further present a comparison of CO_2 dispersion simulations of ARTM with airborne in situ measurements. The measurement data allow the evaluation of the three-dimensional structure of the real exhaust plume and are compared with simulations that originate from all five turbulence models. Finally the model is intercompared to five other atmospheric transport models. This includes the comparison of simulation results with airborne remote sensing and in situ observations at two different atmospheric stabilities: slightly unstable and very unstable. The simulations are used to assess the uncertainty of estimation methods of future satellite missions for monitoring greenhouse gas emissions from point sources. A summary of the findings of this work is given in chapter 6 and an outlook is presented in chapter 7.

Chapter 2

Atmospheric dispersion in the planetary boundary layer

Wind is the most important meteorological parameter to describe the atmospheric transport of gases and particulate matter (PM). Besides advection, turbulence is a main contributor to transport and dispersion. There are different types of modelling approaches to capture the behaviour of dispersion numerically. In this chapter a description of some of the fundamental properties of the planetary boundary layer (PBL) is given followed by a brief history of atmospheric dispersion models (ADMs), their applications today and an introduction to the concepts of atmospheric dispersion modelling focusing on Lagrangian particle dispersion models (LPDMs).

2.1 Introduction to the planetary boundary layer

The properties of the PBL differ from other parts of the atmosphere and significantly affect large parts of live living on Earth. According to its vertical thermal structure, the atmosphere can be divided into several parts with the troposphere being the one in contact with the surface of the Earth. On average it reaches a height of approx. 11 km and can be further divided into sublayers. The lowest portion of the troposphere, which is directly influenced by the underlying surface, is called the planetary boundary layer (PBL). In the following, its vertical structure and the general phenomenon of atmospheric turbulence are described. Furthermore, the theoretical background for the estimation of the vertical wind profile in the PBL is given.

2.1.1 The vertical structure of the planetary boundary layer

The PBL is characterised by spatially and temporally variable thickness ($\approx 10\,\mathrm{m}$ – $4\,\mathrm{km}$) with a limiting capping inversion layer above. It responds to surface forcings such as frictional drag, heat transfer or pollutant emissions with timescales of about one hour or less (Stull 1988).

About the lowest 10% of this PBL is known as the surface layer or constant flux layer. In Germany, this layer is also called Prandtl-layer. Within this layer, also often the turbulent fluxes of momentum, heat and moisture vary by less than 10% of their magnitude and the influence of the Coriolis force is weak. The largest part of the PBL, above the surface layer, is called Ekman-layer. It is characterised by decreasing turbulent fluxes with increasing height and the influence of the Coriolis force that results in a rotation of the wind vector with height until it is parallel to the geostrophic wind. The capping inversion on top of the Ekman-layer confines the PBL from the rather laminar wind flows above. It traps pollutants, turbulence and moisture below. The troposphere above the PBL is called the free troposphere or free atmosphere (Stull 1988; Stull 2006; Etling 2008). The finer structure and a generic temperature profile of the PBL for the daytime is illustrated in Fig. 2.1.

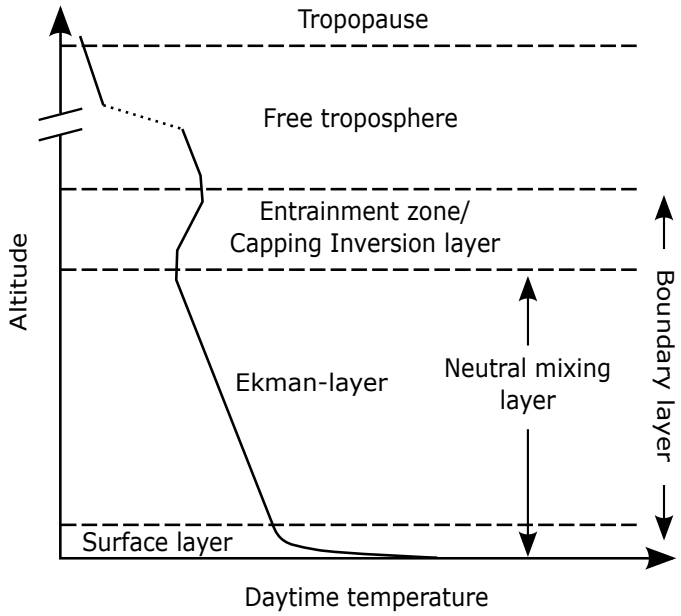

Figure 2.1: Scheme of the vertical temperature profile in the troposphere and its finer structure within the PBL. After Lin et al. (2015).

Depending on the thermal structure of the atmosphere it can be categorised as either unstable, stable or neutral. Supposing an air parcel at an arbitrary location

within the PBL. If this parcel is displaced vertically its temperature changes due to the different pressure. In dry air this temperature gradient is called dry adiabatic lapse rate $\Gamma_\mathrm{d} = -\frac{\mathrm{d}T}{\mathrm{d}z} = 9.77\,\mathrm{K\,km^{-1}}$. If water vapour is a constituent of the air the lapse rate can deviate from the dry adiabatic lapse rate due to condensation of water vapour and the release of heat. The released heat reduces the cooling of ascending air parcels and the lapse rate. This wet adiabatic lapse rate depends on temperature and pressure. If an air parcel is displaced upwards its temperature changes according to dry adiabatic lapse rate if no condensation or evaporation occurs. If its new temperature is larger than the temperature of the surrounding air then it can continue rising and the atmosphere is termed unstable. If the temperature of the displaced air parcel is lower compared to the surrounding air then it would sink back down to lower altitudes and the atmosphere is termed stable. In the case of the displaced air parcel and the surrounding air having the same temperature, the parcel remains at the new position and the atmosphere is termed neutral (Seinfeld et al. 2016).

The PBL is subject to a diurnal variation of the temperature profile depending on the irradiation to the surface, besides the weaker effects of radiation absorption by the atmosphere itself. The absorbed energy at the surface is transferred to the atmosphere via transport processes. Whenever the surface is warm compared to the surrounding air, e.g. due to irradiation by sun light, the air close to the surface becomes warmer, too. Warm air parcels expand and become less dense than their surrounding. Such warm air begins to rise. The PBL becomes thermally unstable. The unstable layer in direct contact with the surface is called the mixed layer and typically occurs at day time. During night time, when the sun light is missing and the surface is colder than the air due to radiative cooling, the air next to the surface cools down, too; the lower atmosphere becomes stable and is called the stable nocturnal boundary layer. This layer does not extend from the surface all the way up to the capping inversion. The portion of the boundary layer between the stable nocturnal boundary layer and the capping inversion is a residual of the daytime mixed layer and is often called the residual layer. Under rather windy and overcast conditions, the PBL becomes neutral due to limited irradiation and radiative cooling (Stull 2006; Seinfeld et al. 2016).

2.1.2 Atmospheric turbulence

Turbulence is part of the atmospheric flow and can be visualised as swirls of different sizes called eddies. These eddies are generated by instabilities of the mean flow and range from global or planetary scale down to molecular scale (Garratt 1992; Stull 2006). The scales of eddies are summarised in Table 2.1. Eddies larger than 200 km are described as two-dimensional turbulence because their horizontal extent is large compared to their vertical extent. Such quasi two-dimensional eddies

Table 2.1: Scales of motion in the atmosphere. Two-dimensional turbulence scales are marked with *, three-dimensional turbulence scales with †. After Stull (2006).

Larger than	Scale	Name
20 000 km*		Planetary scale
2 000 km*		Synoptic scale
200 km*	Meso-α	Mesoscale
20 km†	Meso-β	
2 km†	Meso-γ	
200 m†	Micro-α	Boundary-layer turbulence
20 m†	Micro-β	Surface-layer turbulence
2 m†	Micro-γ	Inertial subrange turbulence
2 mm†	Micro-δ	Fine-scale turbulence
Air molecules †	Molecular	Viscous dissipation subrange

are prevalent in a stably stratified atmosphere such as the stratosphere (Kraichnan et al. 1980; Lilly 1983). Smaller eddies are three-dimensional turbulence (Kraichnan et al. 1980). Large-scale eddies are for instance created by the breaking of large-scale Rossby-waves. Eddies of smaller sizes, as they occur in the PBL, are often created by instabilities of e.g. the already explained rise of warm air caused by solar heating of the surface. Other mechanisms generating turbulence can be the deflection of wind by an obstacle such as a tree or a building or the frictional drag on the air flow over the surface, which causes wind shear producing turbulent eddies. In general, eddies are not stable in space and time; a part of the inertial energy of larger eddies is used for the generation of smaller eddies, which is known as the turbulence cascade. This process ranges from the largest eddies all the way down to the molecular scale, where turbulent kinetic energy is continually dissipated (Stull 1988; Garratt 1992; Stull 2006).

Eddies of different sizes result in the fluctuation of wind speed at different time scales around an average wind speed value. The wind speed fluctuation is quantified by its spectrum shown in Fig. 2.2. The wind speed fluctuations can not be described deterministically but statistically. As proposed by Reynolds, the wind speed components $\vec{u} = (u, v, w)$ in Cartesian coordinates $\vec{x} = (x, y, z)$ can be decomposed as

$$u = \overline{u} + u' \tag{2.1a}$$

$$v = \overline{v} + v' \tag{2.1b}$$

$$w = \overline{w} + w' \tag{2.1c}$$

into a mean or average wind speed $\overline{u}$, $\overline{v}$, $\overline{w}$ and a fluctuation or turbulence part u', v', w' (Reynolds 1895). The turbulence part may vary rapidly with time. The

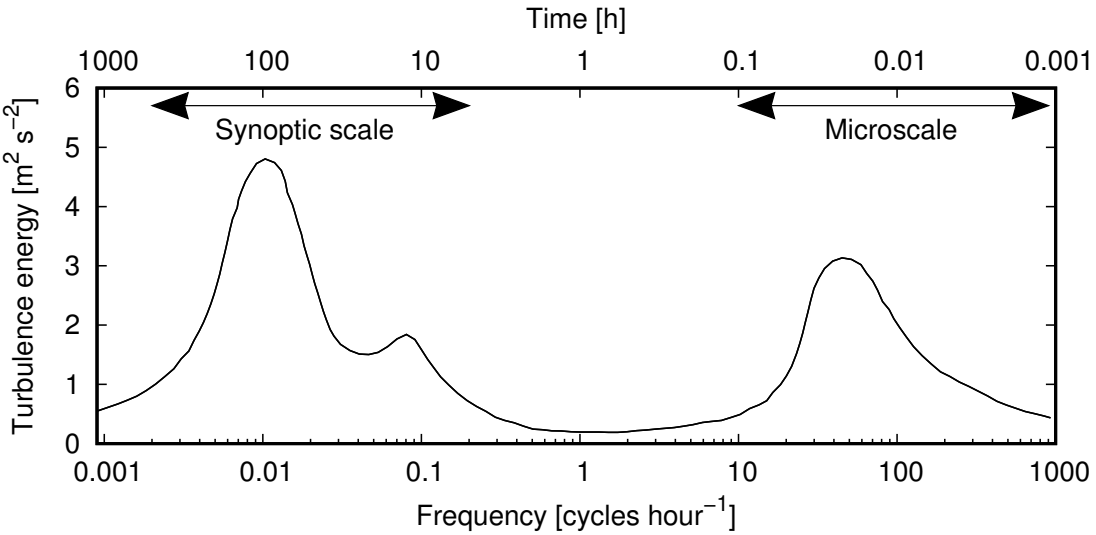

Figure 2.2: Spectrum of horizontal wind speed derived from Van der Hoven (1957) in 100 m height. The graphic shows the turbulence energy over the eddy frequency. After Stull (1988).

intensity of the turbulence in the direction of u is defined as the variance

$$\sigma_u^2 = \frac{1}{N}\sum_{l=1}^{N}(u_l - \overline{u})^2 = \frac{1}{N}\sum_{l=1}^{N}(u_l')^2 = \overline{u'^2} \tag{2.2}$$

with the number of wind speed measurements N and the index $l = 1, \ldots, N$. For the other wind speed components v and w Eq. 2.2 is analogue (Stull 2006). Often, the x-coordinate is chosen parallel the mean wind speed $\overline{u}$ because turbulence along and perpendicular to the mean wind direction can be different.

Fluctuations of wind speed are often accompanied by fluctuations of scalar quantities such as temperature, humidity or pollutant concentration. An example is the rise of warm air heated due to the irradiated surface. The vertical heat flux is the intensity of the co-variation of the potential temperature θ together with the vertical wind speed w. Similar to Eq. 2.2 it is described as the covariance

$$\mathrm{cov}(w,\theta) = \frac{1}{N}\sum_{l=1}^{N}(w_l - \overline{w})\cdot\left(\theta_l - \overline{\theta}\right) = \frac{1}{N}\sum_{l=1}^{N}(w_l')\cdot(\theta_l') = \overline{w'\theta'} \tag{2.3}$$

(Stull 2006; Foken 2016).

The sum of the variances of all wind speed components represents the kinetic energy of the turbulence. The turbulent kinetic energy per unit mass is defined as

$$TKE = \frac{1}{2}\left(\overline{u'^2} + \overline{v'^2} + \overline{w'^2}\right) = \frac{1}{2}\left(\sigma_u^2 + \sigma_v^2 + \sigma_w^2\right) \tag{2.4}$$

(Stull 2006).

2.1.3 The vertical wind profile in the planetary boundary layer

In the PBL the mean wind is highly variable with height above the surface. At the surface the wind velocity is zero. With increasing height the velocity typically increases because of the decreasing influence of the surface. This behaviour is similar to the behaviour of a fluid flow confined by a wall as it is described in classical fluid mechanics. In contrast to the description of classical fluid mechanical systems, the mean wind profile is dependent on the atmospheric stability, too. Furthermore, the wind can be affected by the Earth's rotation. Understanding of the physical processes and their influences on the wind is necessary to be able to describe the dispersion of substances. In the following, the description of wind velocity and wind direction behaviour in the PBL under different atmospheric stabilities is given.

The surface layer in a neutral atmosphere

The wind profile in the lower PBL (surface layer) can be derived theoretically from the Reynolds-averaged Navier-Stokes (RANS) equation for an incompressible flow. The x-component can be given as

$$\frac{\partial \overline{u}}{\partial t} + \left(\overline{u}\frac{\partial \overline{u}}{\partial x} + \overline{v}\frac{\partial \overline{u}}{\partial y} + \overline{w}\frac{\partial \overline{u}}{\partial z} \right) = (f_{\mathrm{z}}\overline{v} - f_{\mathrm{y}}\overline{w}) - \frac{\partial \phi}{\partial x} - \frac{1}{\rho}\frac{\partial \overline{p}}{\partial x} + \nu \left(\frac{\partial^2 \overline{u}}{\partial x^2} + \frac{\partial^2 \overline{u}}{\partial y^2} + \frac{\partial^2 \overline{u}}{\partial z^2} \right) - \left(\frac{\partial \overline{u'u'}}{\partial x} + \frac{\partial \overline{v'u'}}{\partial y} + \frac{\partial \overline{w'u'}}{\partial z} \right), \quad (2.5a)$$

the y-component as

$$\frac{\partial \overline{v}}{\partial t} + \left(\overline{u}\frac{\partial \overline{v}}{\partial x} + \overline{v}\frac{\partial \overline{v}}{\partial y} + \overline{w}\frac{\partial \overline{v}}{\partial z} \right) = (f_{\mathrm{x}}\overline{w} - f_{\mathrm{z}}\overline{u}) - \frac{\partial \phi}{\partial y} - \frac{1}{\rho}\frac{\partial \overline{p}}{\partial y} + \nu \left(\frac{\partial^2 \overline{v}}{\partial x^2} + \frac{\partial^2 \overline{v}}{\partial y^2} + \frac{\partial^2 \overline{v}}{\partial z^2} \right) - \left(\frac{\partial \overline{u'v'}}{\partial x} + \frac{\partial \overline{v'v'}}{\partial y} + \frac{\partial \overline{w'v'}}{\partial z} \right) \quad (2.5b)$$

and the z-component as

$$\frac{\partial \overline{w}}{\partial t} + \left(\overline{u}\frac{\partial \overline{w}}{\partial x} + \overline{v}\frac{\partial \overline{w}}{\partial y} + \overline{w}\frac{\partial \overline{w}}{\partial z} \right) = (f_{\mathrm{y}}\overline{u} - f_{\mathrm{x}}\overline{v}) - \frac{\partial \phi}{\partial z} - \frac{1}{\rho}\frac{\partial \overline{p}}{\partial z} + \nu \left(\frac{\partial^2 \overline{w}}{\partial x^2} + \frac{\partial^2 \overline{w}}{\partial y^2} + \frac{\partial^2 \overline{w}}{\partial z^2} \right) - \left(\frac{\partial \overline{u'w'}}{\partial x} + \frac{\partial \overline{v'w'}}{\partial y} + \frac{\partial \overline{w'w'}}{\partial z} \right) \quad (2.5c)$$

where $f_{x,y,z}$ are the components of the Coriolis parameter, $\phi = \mathrm{a_g} z$ is the geopotential with the acceleration of gravity $\mathrm{a_g}$, ρ is the density, p is the pressure and

ν is the molecular diffusion coefficient (Etling 2008; Oertel et al. 2017). In the surface layer, the following assumptions can be applied to simplify Eqs. 2.5:

1. The flow is in steady state $\frac{\partial \overline{u}}{\partial t} = \frac{\partial \overline{v}}{\partial t} = \frac{\partial \overline{w}}{\partial t} = 0$.
2. The mean flow is horizontally homogeneous $\frac{\partial \overline{u}}{\partial x} = \frac{\partial \overline{u}}{\partial y} = \frac{\partial \overline{v}}{\partial x} = \frac{\partial \overline{v}}{\partial y} = 0$.
3. There is no vertical mean flow (neutral atmospheric conditions) $\overline{w} = 0$.
4. The Coriolis parameter f is negligible in the lower part of the PBL.
5. Horizontal pressure gradients are negligible $\frac{\partial \overline{p}}{\partial x} = \frac{\partial \overline{p}}{\partial y} = 0$.
6. The coordinate system is rotated such that the main flow is in x-direction.
7. The molecular friction is negligible. For the x-component $\nu\left(\frac{\partial^2 \overline{u}}{\partial x^2} + \frac{\partial^2 \overline{u}}{\partial y^2} + \frac{\partial^2 \overline{u}}{\partial z^2}\right) = 0$. (analogue for y- and z-component)
8. The momentum flux is horizontally homogeneous. For the x-component $\frac{\partial \overline{u'u'}}{\partial x} = \frac{\partial \overline{v'u'}}{\partial y} = 0$. (analogue for y- and z-component)

With these simplifications and the fact that the geopotential is horizontally const. $\left(\frac{\partial \phi}{\partial x} = \frac{\partial \phi}{\partial y} = 0 \text{ and } \frac{\partial \phi}{\partial z} = \mathrm{a_g}\right)$, Eq. 2.5a reduces to

$$\frac{\partial \overline{w'u'}}{\partial z} = 0 \tag{2.6}$$

and reveals that the momentum flux $\overline{w'u'}$ = const. with height under neutral conditions. The momentum flux $\overline{w'u'}$ is unknown. Any attempt of deriving an exact solution for the momentum flux results in further unknown variables. This behaviour is known as the closure problem (Keller et al. 1924). In order to circumvent this problem, closure assumptions can be used such as the gradient transport theory, also known as the K-theory, (Stull 1988; Etling 2008; Foken 2016). Analogous to the case of molecular dispersion, a proportionality coefficient K is used to relate the flux of a state variable ξ to the gradient of it (Foken 2016). It is assumed that the turbulence has the same diffusive effect as molecular dispersion. The turbulent flux $\overline{u_k'\xi'}$ of the state variable is directed opposite to the gradient of $\overline{\xi}$ as

$$\overline{u_k'\xi'} = -K_\xi \frac{\partial \overline{\xi}}{\partial x_k} \tag{2.7}$$

where x_k and u_k are the component $k \in \{x, y, z\}$ of the location and velocity vector, respectively. In general, the diffusion coefficient is dependent on location

and time, $K_\xi = K_\xi(x_k, t)$ (Etling 2008). According to Eq. 2.7, the momentum flux can be described as

$$\overline{w'u'} = \overline{w'u'_0} = -K_\mathrm{m}\frac{\partial \overline{u}}{\partial z} \tag{2.8}$$

where u'_0 is the wind speed fluctuation at the height where the average wind speed vanishes and K_m is the diffusion coefficient of the momentum or eddy viscosity. Using the definition for the friction velocity

$$u_* = \sqrt{-\overline{w'u'}} \tag{2.9}$$

Eq. 2.8 can be written as

$$u_*^2 = K_\mathrm{m}\frac{\partial \overline{u}}{\partial z}. \tag{2.10}$$

So far, the eddy viscosity K_m is unknown but according to the mixing length approach after Prandtl (1925), it can be described as

$$K_\mathrm{m} = u_\mathrm{c} l \tag{2.11}$$

with the characteristic velocity u_c and the mixing length l. The characteristic velocity can be defined as

$$u_\mathrm{c} = l\left|\frac{\partial \overline{u}}{\partial z}\right|. \tag{2.12}$$

Thus, the eddy viscosity can be given as

$$K_\mathrm{m} = l^2\left|\frac{\partial \overline{u}}{\partial z}\right|. \tag{2.13}$$

The mixing length is a measure for the size of the eddies. Since the lower PBL is limited by the surface, the radius of an eddy cannot be larger than the distance between the centre of the eddy and the surface. Thus, Prandtl defined the mixing length as

$$l(z) = \kappa z \tag{2.14}$$

with the von Kármán constant κ. After inserting Eqs. 2.13 and 2.14 into Eq. 2.10 and applying the square root to the first order partial differential equation

$$\frac{\partial \overline{u}}{\partial z} = \frac{u_*}{\kappa z} \tag{2.15}$$

is obtained after rearrangement. Using the boundary conditions that at height $z = z_0$ the mean wind speed $\overline{u} = 0$, the integration gives the mean wind speed profile in the lower PBL as

$$\overline{u}(z) = \frac{u_*}{\kappa}\ln\left(\frac{z}{z_0}\right) \tag{2.16}$$

for the neutral boundary layer. z_0 is the roughness length, which defines the height above the surface where the mean wind speed vanishes. The roughness length depends on the surface roughness that depends on surface coverage such as grass, snow, trees or other obstacles. The value of z_0 varies for the different ground coverages but it is not equal to the height of the obstacles itself (Etling 2008).

The logarithmic wind profile given in Eq. 2.16 can also be obtained empirically for the neutral boundary layer. When applying the similarity theory (Stull 1988) to wind speed measurements in the surface layer, the logarithmic wind profile is the expected solution. A detailed derivation of the wind profile from measured data is given by Stull (1988).

The Obukhov length as turbulence parametrisation

For the case of stable or unstable boundary layer conditions, thermal stratification influences the wind profile, which leads to deviations from the mean wind speed profile under neutral conditions given in Eq. 2.16. The relative importance of turbulence produced by buoyancy versus vertical wind shear effects is described by the flux Richardson number

$$Ri_f = \frac{\frac{a_g}{\tilde{\theta}}\overline{w'\theta'}}{\overline{w'u'}\frac{\partial \bar{u}}{\partial z}} \tag{2.17}$$

where $\tilde{\theta}$ is the mean potential temperature, which is also assumed to be constant in time. Using the definition of the friction velocity in Eq. 2.9, Eq. 2.15 and a constant heat flux $\overline{w'\theta'} = \overline{w'\theta'_0} = \text{const.}$, Ri_f can be formulated as

$$Ri_f = \frac{\frac{a_g}{\tilde{\theta}}\overline{w'\theta'_0}}{-u_*^2\frac{u_*}{\kappa z}} = -\frac{\kappa a_g}{\tilde{\theta}}\frac{\overline{w'\theta'_0}}{u_*^3}z = \frac{z}{L} \tag{2.18}$$

with the Obukhov length

$$L = -\frac{\tilde{\theta}}{\kappa a_g}\frac{u_*^3}{\overline{w'\theta'_0}}. \tag{2.19}$$

Thus, L describes the characteristic height where the turbulent energies due to wind shear and buoyancy have the same absolute value (Etling 2008).

Depending on thermal stratification (vertical heat flux) the Obukhov length has the following values:

stable:	$\overline{w'\theta'_0} < 0$	$\Rightarrow$	$L > 0$
neutral:	$\overline{w'\theta'_0} = 0$	$\Rightarrow$	$\lvert L\rvert \longrightarrow \infty$
unstable:	$\overline{w'\theta'_0} > 0$	$\Rightarrow$	$L < 0$

The Obukov length is often used to characterise the atmospheric stability and to parametrise the turbulence in the PBL (Etling 2008; Stull 1988).

The non-neutral surface layer

For the description of the stable or unstable surface layer, Monin et al. (1954) applied the concepts of similarity theory proposing that in a horizontally homogeneous surface layer the mean flow and turbulence characteristics only depend on four independent variables: The height above the surface z, the friction velocity u_*, the heat flux at the surface $\overline{w'\theta'_0}$ and a coefficient describing buoyancy $\frac{a_g}{\overline{\theta}}$. Except for z all the variables can be found in the definition of the Obukhov length in Eq. 2.19.

The starting point for describing the wind profile in stable and unstable conditions is Eq. 2.15, which describes the wind profile in the neutral surface layer. Similarity theory requires physical processes to be described by dimensionless quantities, therefore, Eq. 2.15 has to be used in its dimensionless form

$$\frac{\kappa z}{u_*}\frac{\partial \overline{u}}{\partial z} = \Phi\left(\frac{z}{L}\right) \tag{2.20}$$

with a dimensionless function Φ. Equation 2.20 is valid for neutral and non-neutral surface layer conditions depending on the exact formulation of Φ. According to the similarity hypothesis of (Monin et al. 1954), Φ has to be a function only of L and z and is often called profile function. The function is generally written in the form

$$\Phi\left(\frac{z}{L}\right) = 1 + \alpha\frac{z}{L} \tag{2.21}$$

with an arbitrary coefficient α. For neutral conditions α is not important because $\frac{z}{L} = 0$ and Eq. 2.20 is equivalent to Eq. 2.15. For the stable and unstable boundary layer, α has to be determined from measurements. Often the profile functions

$$\begin{aligned}
&\Phi = 1 + 5\frac{z}{L} && \text{for } \frac{z}{L} > 0 && \text{stable,}\\
&\Phi = 1 && \text{for } \frac{z}{L} = 0 && \text{neutral,}\\
&\Phi = \left(1 - 15\frac{z}{L}\right)^{-\frac{1}{4}} && \text{for } \frac{z}{L} < 0 && \text{unstable}
\end{aligned} \tag{2.22}$$

after Businger et al. (1971) and Dyer (1974) are used. By integrating Eq. 2.20 with the respective profile functions from Eqs. 2.22, the wind speed profiles for stable and unstable stratification are obtained as

$$\begin{aligned}
\overline{u}(z) &= \frac{u_*}{\kappa}\left(\ln\frac{z}{z_0} + 5\frac{z - z_0}{L}\right) && \text{for } \frac{z}{L} > 0 \quad \text{stable,}\\
\overline{u}(z) &= \frac{u_*}{\kappa}\left[\ln\left(\frac{\psi - 1}{\psi_0 - 1}\right) - \ln\left(\frac{\psi + 1}{\psi_0 + 1}\right)\right. && \\
&\qquad \left. + 2\left(\tan^{-1}\psi - \tan^{-1}\psi_0\right)\right] && \text{for } \frac{z}{L} < 0 \quad \text{unstable}
\end{aligned} \tag{2.23}$$

with

$$\psi = \left(1 - 15\frac{z}{L}\right)^{\frac{1}{4}} \quad \text{and}$$
$$\psi_0 = \left(1 - 15\frac{z_0}{L}\right)^{\frac{1}{4}}, \tag{2.24}$$

respectively (Etling 2008; Ragland 1973). Both deviate from the average wind profile of the neutral surface layer given in Eq. 2.16 at page 14 but the logarithmic character is still present.

The wind profile in the neutral Ekman-layer

The part of the boundary layer above the surface layer is denoted as the Ekman-layer and covers most of the mixing layer. Because of the larger distance from the surface not all the assumptions, which have been made for the surface layer on page 13 hold. With increasing height, the Coriolis force becomes more important and pressure gradients can no longer be neglected. Thus, the assumptions 4 to 6 are no longer applicable. However, under the assumption of a steady state and horizontally homogeneous flow, we can derive another set of equations describing a wind profile that changes direction with height. Furthermore, to simplify this derivation it is assumed that the Ekman-layer begins at the surface (Etling 2008).

Starting from the RANS equations 2.5 at page 12 and applying the remaining assumptions, the horizontal components of the wind speed follow

$$-f_z\,\overline{v} + \frac{1}{\overline{\rho}}\frac{\partial \overline{p}}{\partial x} = -\frac{\partial \overline{w'u'}}{\partial z}$$
$$f_z\,\overline{u} + \frac{1}{\overline{\rho}}\frac{\partial \overline{p}}{\partial y} = -\frac{\partial \overline{w'v'}}{\partial z}. \tag{2.25}$$

In contrast to the surface layer (Eq. 2.8 at page 14), the vertical momentum flux of the horizontal wind components ($\overline{w'u'}$ and $\overline{w'v'}$) and consequently K_m is not constant. The gradients of the momentum fluxes represent the turbulent friction. At the top of the boundary layer h_m (at large distance from the surface) the horizontal momentum fluxes (turbulent friction) vanish and the wind is equal to the geostrophic wind

$$\overline{u_\mathrm{g}} = -\frac{1}{\overline{\rho}\,\overline{f_z}}\frac{\partial \overline{p}}{\partial y} \text{ and } \overline{v_\mathrm{g}} = +\frac{1}{\overline{\rho}\,\overline{f_z}}\frac{\partial \overline{p}}{\partial x}. \tag{2.26}$$

When moving towards the surface, the turbulent friction increases which changes the balance between the Coriolis force, the pressure gradient force and the turbulent friction. This results in a change of the wind direction forming the so-called Ekman-spiral (Etling 2008).

When inserting Eqs. 2.26 into Eqs. 2.25, applying the K-theory and integrating from the surface to the boundary layer top ($0 \leq z \leq h_\mathrm{m}$), the wind speed components can be calculated as

$$\begin{aligned}\overline{u}(z) &= \overline{u_\mathrm{g}}\left[1 - \exp\left(-\frac{z}{L_\mathrm{E}}\right)\cos\frac{z}{L_\mathrm{E}}\right] - \overline{v_\mathrm{g}}\exp\left(-\frac{z}{L_\mathrm{E}}\right)\sin\frac{z}{L_\mathrm{E}},\\ \overline{v}(z) &= \overline{v_\mathrm{g}}\left[1 - \exp\left(-\frac{z}{L_\mathrm{E}}\right)\cos\frac{z}{L_\mathrm{E}}\right] + \overline{u_\mathrm{g}}\exp\left(-\frac{z}{L_\mathrm{E}}\right)\sin\frac{z}{L_\mathrm{E}}\end{aligned} \tag{2.27}$$

with the Ekman length

$$L_\mathrm{E} = \sqrt{2\frac{K_\mathrm{m}}{f_\mathrm{z}}}. \tag{2.28}$$

This delivers a qualitative description of the wind speed from the surface to the top of the boundary layer. However, it does not generally agree with observations, which typically show smaller rotations of the wind direction with increasing height. The problem is the assumption of a constant K_m with height, which is not valid for the surface layer. Thus, other descriptions such as a two-layer description can be found in literature. It is assumed that the turbulent diffusion increases linearly with height in the surface layer up to the surface layer top z_s ($0 \leq z \leq z_\mathrm{s}$) and stays constant above to the top of the boundary layer ($z_\mathrm{s} \leq z \leq h_\mathrm{m}$). This corresponds to a surface layer as described in Subsec. "The surface layer in a neutral atmosphere" at page 12 with the Ekman-layer above (Etling 2008).

When the x-direction of the coordinate system is assumed to be in the direction of the mean geostrophic wind $\overline{u_\mathrm{g}}$, the wind profiles for the horizontal wind components in the surface layer ($0 \leq z \leq z_\mathrm{s}$) can be given as

$$\begin{aligned}\overline{u}(z) &= \frac{u_*}{\kappa}\ln\frac{z}{z_0}\cos\alpha_0,\\ \overline{v}(z) &= \frac{u_*}{\kappa}\ln\frac{z}{z_0}\sin\alpha_0\end{aligned} \tag{2.29}$$

and in the Ekman-layer ($z_\mathrm{s} \leq z$) as

$$\begin{aligned}\overline{u}(z) &= \overline{u_\mathrm{g}}\left[1 - \sqrt{2}\exp\left(-\frac{z-z_\mathrm{s}}{L_\mathrm{E}}\right)\sin\alpha_0\cos\left(\frac{z-z_\mathrm{s}}{L_\mathrm{E}} + \frac{\pi}{4} - \alpha_0\right)\right],\\ \overline{v}(z) &= \overline{v_\mathrm{g}}\sqrt{2}\exp\left(-\frac{z-z_\mathrm{s}}{L_\mathrm{E}}\right)\sin\alpha_0\cos\left(\frac{z-z_\mathrm{s}}{L_\mathrm{E}} + \frac{\pi}{4} - \alpha_0\right).\end{aligned} \tag{2.30}$$

α_0 denotes the difference of the wind directions compared to the geostrophic wind. The values for $\overline{u_\mathrm{g}}$, $\overline{v_\mathrm{g}}$, z_0 and z_s have to be measured. Under the assumption that the wind speed components are continuous at z_s the values for u_* and α_0 can be calculated iteratively to obtain the complete wind profile. Wind profiles for the stable and unstable boundary layer can be composed in an analogous way (Etling 2008).

2.2 Introduction to dispersion modelling

Dispersion is the key process that influences the accumulation and dilution of any substance in the atmosphere. It is defined as the spreading of atmospheric constituents and the result of turbulent diffusion, molecular diffusion and mean wind shear (AMS 2022). Atmospheric constituents are the natural air constituents as well as contaminations originating from natural and anthropogenic emissions. The contamination of the environment by any chemical, physical or biological agent including gaseous pollutants and PM that modifies the natural characteristics of the atmosphere is defined as air pollution (WHO 2022). This includes non-ionizing as well as ionizing substances. The monitoring of the constituents of the air occurs at certain measurement stations which only provide local information about concentrations. Satellite observations can provide much better spatial coverage but only very few air pollutants such as nitrogen dioxides (NO_2) can be measured from satellites with sufficient accuracy. Atmospheric dispersion modelling can provide additional information in all three dimensions and thus became a common tool for air quality assessment and the estimation of immissions of radionuclides complementary to observations (De Visscher 2014). ADMs use mathematical equations to describe the transport of constituents of the atmosphere by advection and turbulent diffusion. Concentrations of the constituents are calculated at various locations (Holmes et al. 2006; Stockie 2011). Besides the basic physical properties of diffusion, other processes such as sedimentation of PM, deposition at the surface, plume rise of emissions or chemical reactions can be included in ADMs as well depending on the purpose of the model (Stockie 2011; Beevers et al. 2020). In general, the application of ADMs is not limited to local or regional scales or to the PBL but can be applied to global scale and higher atmospheric levels, too.

2.2.1 A brief history of dispersion modelling of air pollutants and radionuclides in the atmosphere

The development of atmospheric dispersion models can be seen as a consequence of the growing understanding of atmospheric flows and of progresses of the description of turbulent motion at the beginning of the twentieth century and the development of computers in the late 1940's. It is difficult to identify one specific event that marks the beginning of atmospheric dispersion modelling because the development of the theoretical background was an important constituent of this process. In the following, some milestones are given than can be seen as the basis that later resulted in the formulation and implementation of atmospheric dispersion models of different types for the purpose of simulating the spread of emission plumes of air pollutants and radionuclides.

A first milestone was the formulation of the eddy diffusion theory. It is the gen-

eralization of the molecular diffusion to the turbulent diffusion in the atmosphere. Fundamentals of this theory were simultaneously presented by Taylor et al. (1915) and Richardson (1922) in England as well as by Schmidt (1925) in Austria. They used observations of smoke, volcanic ash and other PM to develop their description of the spread of emission plumes. Only 6 years after his contribution to the eddy diffusion theory, Taylor (1921) continued his work on turbulent diffusion and presented his exact Lagrangian solution for the rate of spread of tracer in stationary homogeneous turbulence (Thomson et al. 2012).

Based on the work of Taylor et al. (1915) and Taylor (1921), Sutton et al. (1932) further improved the early eddy diffusion theory and formulated first dispersion models in the context of chemical warfare for emissions from continuous point sources of gas and PM at the ground and from chimneys (Sutton et al. 1934; Sutton 1947a; Sutton 1947b). However, the applicability of these models were limited to neutral atmospheric stability and to scales of only a few hundred meters covering durations of minutes. Due to further investigations at the Chemical Defence Experimental Establishment in Porton, USA, Pasquill (1961) gave a formulation describing the dispersion of tracers in an exhaust plume under a variety of atmospheric conditions with the concentration distribution of the plume having a Gaussian shape in its lateral and vertical direction. An early implementation of a Gaussian plume model was presented by Turner (1964). In his work, he compared sulphur dioxide (SO_2) measurements in an urban area (Nashville, USA) with simulated concentrations emitted by an area source.

While the analytical solution for the transport of tracer in the atmosphere led to the Gaussian plume models, there is also the deterministic solution of the continuity equation resulting in the formulation of Eulerian transport models (Leelőssy et al. 2018). Improvements in the eddy diffusion theory resulted in the first implementation of a Eulerian transport models by Reynolds et al. (1973). They used the continuity equation in combination with the eddy diffusion theory (today known as K-theory) for the modelling of tracer dispersion to simulate the photochemical reactions of air pollutants over Los Angeles.

Based on the Lagrangian solution for the rate of spread of tracer in turbulent flows, a third type of dispersion models was developed in parallel to the others (Thomson et al. 2012). These LPDMs represent a stochastic solution for the turbulent motion of particles or parcels of the flow (Leelőssy et al. 2018). Early attempts used simple random walk models to simulate the turbulent dispersion of tracer. However, such treatments of turbulent diffusion are insufficient because they generalize the turbulent diffusion over the complete spatial range (near-field and far-field) (Thomson et al. 2012). Following some discussions of the characteristics of Markov processes, Bullin et al. (1974) applied a Markov process for the turbulent motion of tracers in their early implementation of a LPDM. In the

following years, a large number of studies have been published investigating the dispersion of passive tracers with LPDMs (Thomson 1987).

Although atmospheric dispersion models were considered to be of interest for the identification of the impact of nuclear power plant emissions to the environment (Slade 1968; Apsimon et al. 1985), their application received a boost after the nuclear accident of Chernobyl in April 1986. Different Lagrangian dispersion models were applied to study the dispersion of radionuclides over Europe (Albergel et al. 1988; Pudykiewicz 1989). Another consequence of the Chernobyl accident was the development and further development of different types of dispersion models for the simulation of radionuclides from the meso-scale over regional-scale to the synoptic-scale (Barnicki et al. 1996; Thaning et al. 1997; Stohl et al. 2005; Ryall et al. 1998; Jones et al. 2007; Arnold et al. 2012). Today, ADMs are widely installed for monitoring and regulatory purposes of nuclear power plants under routine operation and at accidents (Simmonds et al. 1995; Jones et al. 2007; StrlSchV 2018).

2.2.2 Modelling the dispersion of pollutants and radionuclides

Today, there is a vast field of applications for ADMs. Different kinds of pollutants have been studied to improve dispersion modelling and to analyse the impact of the pollutant to the environment, respectively. In the following, a few examples of the application of atmospheric dispersion models are given.

The dispersion of ash and other pollutants from the Eyjafjallajökull volcanic eruption have been simulated with the aim to improve the quantitative estimation of volcanic ash emission rates (Stohl et al. 2011). Devenish et al. (2012) used dispersion simulations of the eruption to minimise uncertainty contributions of different input parameters of long-range dispersion models such as the height of eruption column or the size of the particulates. Schumann et al. (2011) applied atmospheric dispersion simulations to find safe flight zones during and after eruptions to allow safe airborne in situ and remote sensing measurements of volcanic discharges[1]. Atmospheric dispersion models have also been used for the simulation of the airborne spread of some disease of livestock such as foot-and-mouth disease or bluetongue (via insects spread by the wind) (Sørensen et al. 2001; Gloster et al. 2010; Burgin et al. 2017). Sheridan et al. (2004) and Hayes et al. (2006) studied the dispersion of odour from intensive pig and poultry production units in Ireland and how it is influenced by feed, building design and operation. One of the most frequently studied topics with air dispersion modelling is the dispersion

[1]Large concentrations of volcanic ash can damage jet engines of aircraft within short time and thus represent a serious threat to flight safety (Chen et al. 2015).

of air pollutants in urban areas. The large number of pollution sources in urban areas, the complex structure of urban areas with buildings and the dense population in cities make urban areas a target area for authorities and the scientific community. The dispersion of substances such as carbon monoxide (CO), carbon dioxide (CO_2), nitrogen oxides (NO_x), SO_2 and particulate matter PM_{10} of road traffic, harbour and industrial emissions and their impact on air quality are heavily studied (Karppinen et al. 2000; Mazzeo et al. 2008; Ionov et al. 2021; Borrego et al. 2003; Gariazzo et al. 2007; Berchet et al. 2017). Atmospheric dispersion models are also used to identify the source location of conventional or radioactive tracers when measurements at receptors are provided (Lin et al. 2003; Becker et al. 2007; De Meutter et al. 2017). This inverse modelling is an advantage of LPDMs because the dispersion backwards in time can easily be calculated compared to Eulerian dispersion models (Henne et al. 2016; Seibert et al. 2004).

Radionuclides are associated with special hazardous potential. Thus, the dispersion of radionuclides in the atmosphere is of special interest either for the case of accidental releases or for releases under routine operation of nuclear installations. Dispersion modelling of different radionuclides originating from the Chernobyl and the Fukushima Nuclear Power Plant (NPP) accidents were performed in order to estimate radionuclide concentration levels and dose estimation (Gudiksen et al. 1989; Lauritzen et al. 1999; Chino et al. 2011; Lin et al. 2015; Arnold et al. 2015; Sato et al. 2020). The exposure of the population to airborne discharges from nuclear installations under routine operation is very low compared to the exposure from natural background radiation and very challenging to be measured directly (Murith et al. 1986; Ohera et al. 1993; Lee et al. 2019). Therefore, it is common to use atmospheric dispersion models to estimate the exposure of the population (Schorling 1995; Simmonds et al. 1995; Smith et al. 2002; Mayall 2003; AVV 2012; StrlSchV 2018; AVV Tätigkeiten 2020).

2.2.3 Overview of the types of atmospheric dispersion models

For all these purposes and more, there are different types of atmospheric dispersion models available: Gaussian plume models, Gaussian puff models, Eulerian transport models and Lagrangian particle dispersion models. All the different model types have certain advantages and disadvantages concerning their applicability and computational load.

Gaussian plume models use a simplified description of the dispersion of exhaust plume. Under the assumptions of a homogeneous and steady-state flow the exhaust plume originating from a continuous source can be described as a cone with Gaussian lateral (perpendicular to the direction of mean wind speed) and

vertical (as far as not limited by the surface) concentration distribution (Turner 1964; Leelőssy et al. 2014). Due to their simple analytical formulation, Gaussian models are inexpensive in terms of computation time. However, they rely on strong assumptions such as steady-state and homogeneous wind conditions, which limits their applicability to a maximum distance of a few tens of km from the source. Further, they are not designed to simulate low wind conditions (Holmes et al. 2006). Although hourly plume concentrations can have a Gaussian distribution under some conditions this is usually not the case for shorter averaging times (De Visscher 2014).

A further development of Gaussian plume models are the Gaussian puff models. They simulate the exhaust plume as a number of puffs sequentially emitted at the source and having a Gaussian concentration distribution in all directions. Each puff is subject to the local mean wind flow and independent of other puffs. Hence, these models can also simulate curved plumes when the mean wind direction rotates (Leelőssy et al. 2014). Their results are more accurate compared to Gaussian plume models and perform well for distances up to 50 km. Gaussian puff models are computationally more expensive as Gaussian plume models because they have to handle a large number of puffs instead of one single plume (De Visscher 2014).

Eulerian models solve the transport equation numerically in a fixed coordinate frame and for fixed grid points. The transport equation describes the concentration of a single tracer in time and depends on the advection of the tracer, the sources or sinks of the tracer and the turbulent diffusion of the tracer. The turbulent diffusion is usually modelled analogous to the molecular diffusion of Fick's law (Zannetti 1991; De Visscher 2014). Eulerian models are more expensive concerning computation time. They work well at large scales but the dispersion is not well represented close to the source and at sub-grid scale (De Visscher 2014).

In contrast to the direct simulation of concentrations of the model types described above, Lagrangian particle dispersion models calculate distinct trajectories of tracers or fluid parcels represented by a large number of numerical particles. In its simplest realisation these numerical particles are assumed to be points that follow the underlying wind and turbulence fields exactly. The turbulent fluctuation is often estimated as a random walk (Leelőssy et al. 2014). LPDMs mimic the transport of single particles and thus simulate closest to real transport processes. However, the computational costs depend on the number of numerical particles and can become very high for large scale, long-term simulations with multiple sources (De Visscher 2014).

Any atmospheric simulation of tracer dispersion needs information about meteorology such as mean wind direction, mean wind speed and atmospheric stability as input. Based on this meteorological input the dispersion of tracers is simulated according to the model type (Gaussian plume model, Gaissian puff model, etc.).

Different models require different levels of detail of the meteorological information. The complexity ranges from a simple vertical wind profile to three-dimensional prognostic meteorological fields. Such three-dimensional inputs can be provided for example from Large-Eddy-Simulation (LES) model, numerical weather prediction (NWP) models or computational fluid dynamic (CFD) models (Leelőssy et al. 2014; Zannetti 1991; De Visscher 2014). In contrast to this, there are also ADM systems which calculate the meteorology and the dispersion of tracers at the same time.

2.2.4 Lagrangian particle dispersion models (LPDMs)

In classical fluid mechanics there are two ways to describe fluid motion: the Eulerian (field) description; and the Lagrangian (particle) description. Both perspectives are illustrated in Fig. 2.3. They complement each other because they describe the same flow (Cohen et al. 2007).

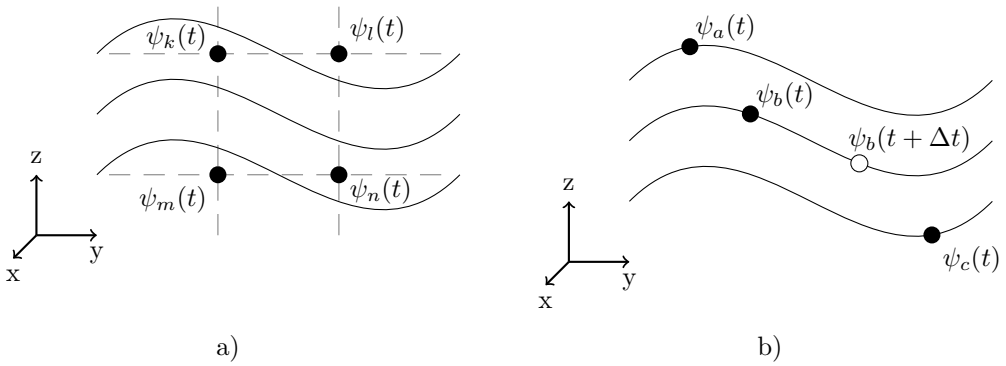

Figure 2.3: Illustration of a) the Eulerian and b) the Lagrangian description of a fluid flow. a) In the Eulerian perspective an underlying flow (solid black lines) is described by the fluid flow property ψ at different fixed locations k, l, m, n (solid dots) at time t. b) In the Lagrangian perspective the underlying flow is described by flow properties for fluid particles $\{a, b, c\}$ following the flow at different time steps t (solid dots) and $t + \Delta t$ (circle).

The Eulerian description uses a fixed reference frame in space and time. It gives information about the properties of the flow in the form of a field. The flow is described at discrete and fixed positions in space. At these positions the fluid properties are given at the same time. Those properties can be for example spatial distribution of air temperature or wind speed. Meteorological stations measure the weather according to the Eulerian description (Etling 2008; Cohen et al. 2007; Lin 2013).

The Lagrangian description uses reference frames that change in space and time. One reference frame is bound to one fluid parcel and moves with it. Information about the flow field are given by observation of distinguishable fluid parcels or tracers through space and time. The paths of the fluid particles form trajectories on which the fluid properties are described at any time (Etling 2008; Cohen et al. 2007; Lin 2013).

Fluid properties of the two perspectives can be transformed into each other using the substantial derivative

$$\frac{\mathrm{D}\psi}{\mathrm{D}t} = \frac{\partial\psi}{\partial t} + \vec{u} \cdot \vec{\nabla}\psi \tag{2.31}$$

where ψ is a state variable associated with a fluid particle. The left-hand side of the equation represents the rate of change when following the fluid particles. The first part of the right-hand side $\frac{\partial\psi}{\partial t}$ represents the rate of change in the Eulerian reference frame i.e. the rate of change at a fixed position and the second part $\vec{u} \cdot \vec{\nabla}\psi$ is a non-linear advection term representing the advection from one location to another with the flow where the value of ψ may be different (Cohen et al. 2007; Lin 2013).

LPDMs are a type of dispersion models, which use numerical particles to simulate the dispersion according to the Lagrangian perspective. A large number of numerical particles are released at the emission source. They are then propagated in space and time individually according to the underlying flow field which, usually is given in the Eulerian description (Thomson 1987; Lin 2013). Each numerical particle forms a distinct trajectory and represents a certain amount of tracer. The basic properties of the numerical particles are that they are not subject to any deformation or inertia so that they follow the flow field and its eddies exactly. Furthermore, they are large compared to the intermolecular distance and have comparable densities as the surrounding air. Thus, no buoyancy or sedimentation occurs without additional properties assigned to the numerical particles (Luhar 2013), which would be the case when modelling PM or when discharges have higher temperatures than the surrounding air. The position of a numerical particle is advanced from one time step to the next as

$$\vec{x}(t_{m+1}) = \vec{x}(t_m) + \tau \underbrace{\left[\overline{\vec{u}}(x_m) + \vec{u}' + \vec{u}_{\mathrm{add}}\right]}_{\vec{u}_{\mathrm{trans}}} \tag{2.32}$$

with time t, time step $\tau = t_{m+1} - t_m$ (m is the index of the time step) and the additional velocity $\vec{u}_{\mathrm{add}}$ that comprises for instance velocities due to sedimentation or buoyancy. The average wind speed, the turbulent wind speed fluctuation and the additional wind speed are the transport velocity $\vec{u}_{\mathrm{trans}}$ of a numerical particle (Anfossi et al. 1993; Hanfland et al. 2022). An example for the trajectories of ten

numerical particles simulated by a LPDM with additional plume rise is illustrated in Fig. 2.4.

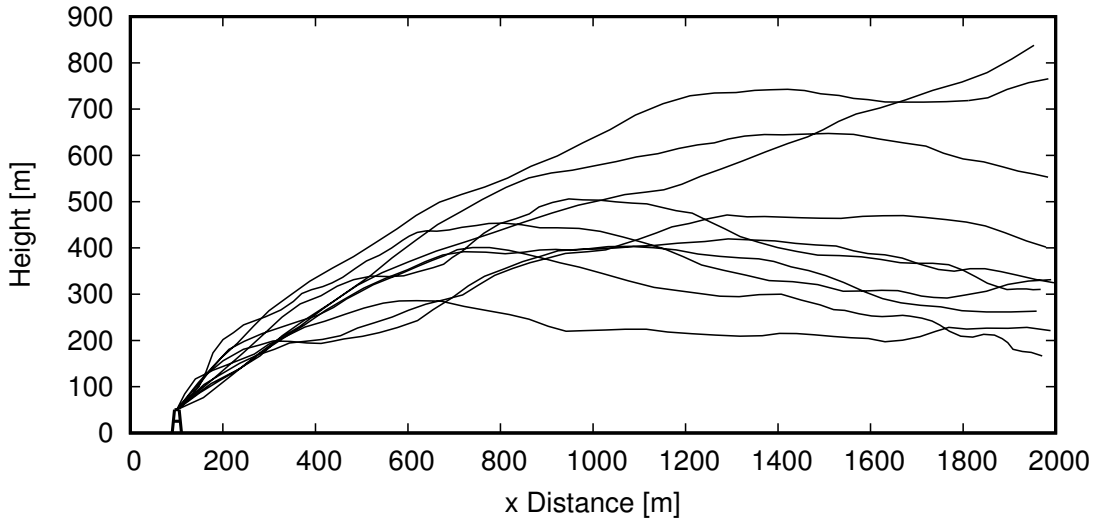

Figure 2.4: Trajectories of ten particles emitted from a stack (point source) with additional plume rise simulated with the Atmospheric Radionuclide Transport Model (ARTM).

The flow field is of great importance because it provides the driving force to propagate numerical particles, the mean wind components $\overrightarrow{\overline{u}}$ and the turbulence components $\overrightarrow{u}'$. The mean wind field is generated from separate meteorological models, which often provide not only flow information but also other meteorological parameters such as temperature, humidity or cloud cover. Such models are either coupled directly to the LPDM or they provide data sets that can be read by the LPDM. Depending on the scale of its application, the meteorological fields can originate from NWP models for larger scale applications, static diagnostic models for applications in the range of a few km to a few tens of km or prognostic fluid dynamic models for smaller scale applications. LPDMs mimic also the turbulent motion by a suitable statistical process (Holmes et al. 2006; Leelőssy et al. 2018; Trini Castelli et al. 2018; Pisso et al. 2019). This process is often modelled as a Markov chain process in the form of a Langevin equation (Thomson 1987; Lin et al. 2013).

The concept of LPDMs is beneficial for the simulation of atmospheric dispersion because it describes the physical processes of particle dispersion closer to reality compared to other approaches (Wilson et al. 1996). They also allow the unique application of inverse simulations to gain information about the location of unknown emission sources when tracers are recorded at a known receptor (Lin et al. 2003). However, depending on the number of numerical particles, LPDMs

can become computationally intensive. A concrete example for the formulation of the LPDM ARTM is presented in Chapter 3.

2.3 Model evaluation

As proposed by Kleijnen (1995) and Rao (2005), model validation should comprise two parts: Sensitivity analysis (SA) and the comparison with observations. The SA investigates the influence of the variation of input parameters to the model results. This can reveal whether a model reacts as expected when changing a certain input parameter. Furthermore, it can answer the following questions: How does the uncertainty of input parameters influence the model output; which parameters require additional research in order to reduce output uncertainty; which parameters are most significant or insignificant for the model's output (Hamby 1994; Frey et al. 2002; Rao 2005; Saltelli et al. 2008; Hanfland et al. 2023).

The comparison of simulation results with observations shows how well the simulation represents the real-world system. In the case of complex systems such as the atmosphere, this may require a large number of comparisons using different boundary conditions. For simulations modelling the processes in the PBL, it is beneficial to use data sets sampling the whole vertical extent of the PBL than just the atmosphere close to the surface. This makes measurement campaigns expensive and thus, it can be challenging to find proper measurement data sets for comparison studies.

For LPDMs that work with a Markov process for the turbulence modelling, it is also important to demonstrate that initially uniform distributions of tracers in an incompressible flow remain uniform as it is postulated by the second law of thermodynamics (Sawford 1986; Thomson 1987; Lin et al. 2013; Bahlali et al. 2020). As pointed out by Thomson (1987) this cannot in general be assumed for turbulence modelling via Markov processes. By applying these three tasks to Lagrangian atmospheric dispersion models, the credibility of model results can be demonstrated. These important concepts guided the work performed in this thesis.

Additionally, ARTM was part of a joint atmospheric transport model comparison. The performance of ARTM was compared to more sophisticated, computational more expensive models to account for difference in simulation results.

For the validation attempts presented in this work a large number of ARTM simulation runs (25 628) had been performed. An overview of the performed simulations is given in Tab. 2.2.

Table 2.2: Overview of performed simulations.

Analysis	Sub-category	Detail	Nr. of Simulations
Sensitivity analysis	Local SA	Variation of stability class (SC)	6
Sensitivity analysis	Local SA	Variation of z_0	6
Sensitivity analysis	Local SA	Variation of d	4
Sensitivity analysis	Local SA	Variation of h_s	8
Sensitivity analysis	Local SA	Variation of particle type	6
Sensitivity analysis	Global SA	Variation of SC, z_0, d and h_s	24 576
Sensitivity analysis	Graphical SA	Variation of L, z_0, d and h_s	1 000
Well-mixed test	very unstable	30-day simulations for five turbulence models (TMs)	6
Comparison with observations	Jänschwalde	Intercomparison with other models	8
Comparison with observations	Bełchatów	Intercomparison with other models	8

Chapter 3

The Atmospheric Radionuclide Transport Model (ARTM)

The Atmospheric Radionuclide Transport Model (ARTM) is a LPDM developed by the Gesellschaft für Anlagen- und Reaktorsicherheit gGmbH (GRS) on behalf of the Federal Office for Radiation Protection (BfS) of Germany in 2007. Its purpose is to provide annual activity fields of radionuclides emitted from nuclear facilities under routine operation in the vicinity of the emitter in slightly structured non-urban terrain. It is based on the model AUSTAL2000 2.2.11 that had been developed for conventional tracers before. Typical simulation domains have a horizontal extent between 2 km × 2 km and 15 km × 15 km and vertically cover the entire PBL (Hanfland et al. 2022; Hanfland et al. 2023).

ARTM consists of a static mass-conserving diagnostic wind field model. This has to be distinguished from computational more expensive prognostic meteorological fields provided by NWP models like COSMO or CFDs models like GRAMM and MISKAM, which are used by other LPDMs such as FLEXPART, STILT, NAME, HYSPLIT or GRAL (Lin et al. 2003; Stohl et al. 2005; Ryall et al. 1998; Draxler et al. 1998; Oettl 2015; Doms et al. 2013; Eichhorn et al. 2010). The second part of ARTM is a particle transport model that propagates the numerical particles according to the calculated wind fields. Wind speed fluctuations and Lagragian correlation time scales are feed into a Markov process to parametrise turbulence (Hanfland et al. 2022; Hanfland et al. 2023).

The physical and mathematical concepts of ARTM that are important for the understanding of this study are published for the first time in a peer-reviewed article in Hanfland et al. (2022). Major parts of the Secs. 3.1 and 3.2 with the Subsecs. 3.2.1 - 3.2.8 of this work are published in Hanfland et al. (2022) and are cited here. Features such as the handling of buildings or the plume rise through cooling towers are not part of this study and thus excluded from the following description.

3.1 The wind field model TALdia

The diagnostic wind field model TALdia was developed by Janicke Consulting and provides wind and turbulence fields for the Lagrangian particle dispersion model ARTM when terrain is present (Janicke et al. 2003; Janicke et al. 2004; GRS 2007). TALdia uses a mass conservation approach to model the wind field within the simulation domain. Hourly wind fields are generated by using a boundary layer model and in situ wind measurements $\vec{u}_{\text{meas}}$ (velocity and direction) at a single location within the simulation domain (Richter et al. 2015b). In the absence of terrain, only the boundary layer model described in the next section is applied to model the wind and turbulence fields. In this work TALdia 2.7.0 is described.

3.1.1 The boundary layer model of TALdia

The boundary layer model is based on similarity theory and employs a logarithmic wind profile where the mean wind speed $\overline{|\vec{u}(z)|}$ at height z depends on the atmospheric stability as

$$\overline{|\vec{u}(z)|} = \frac{u_*}{\kappa} \cdot \begin{cases} \left\{ \ln\left[\frac{(\psi-1)(\psi_0+1)}{(\psi+1)(\psi_0-1)}\right] + 2\left(\tan^{-1}\psi - \tan^{-1}\psi_0\right) \right\} & \text{for } \frac{z_{d_0}}{L} < 0 \\ \left\{ \ln\frac{z_{d_0}}{z_0} + 5\left(\frac{z_{d_0}-z_0}{L}\right) \right\} & \text{for } 0 \le \frac{z_{d_0}}{L} < 0.5 \\ \left\{ 8\ln\left(2\frac{z_{d_0}}{L}\right) + 4.25\left(\frac{z_{d_0}}{L}\right)^{-1} - 0.5\left(\frac{z_{d_0}}{L}\right)^{-2} - \ln\left(2\frac{z_0}{L}\right) - 5\frac{z_0}{L} - 4 \right\} & \text{for } 0.5 \le \frac{z_{d_0}}{L} < 10 \\ \left\{ 0.7585\frac{z_{d_0}}{L} + 8\ln 20 - 11.165 - \ln\left(2\frac{z_0}{L}\right) - 5\frac{z_0}{L} \right\} & \text{for } 10 \le \frac{z_{d_0}}{L} \end{cases} \tag{3.1}$$

with

$$z_{d_0} = z - d_0, \tag{3.2a}$$

$$\psi = \left(1 - 15\frac{z_{d_0}+z_0}{L}\right)^{\frac{1}{4}} \tag{3.2b}$$

and

$$\psi_0 = \left(1 - 15\frac{z_0}{L}\right)^{\frac{1}{4}} \tag{3.2c}$$

where $\kappa = 0.4$ is the von Kármán constant and d_0 represents the zero-plane displacement (Stull 1988; VDI 3783 part 8 2002). The Obukhov length L is either determined directly from measurements or by determining the atmospheric stratification and divide its stability into six SCs parametrising the turbulence in the atmosphere (Klug 1969; Richter et al. 2015a). In the latter case, the Obukhov length can be determined using the SC and the roughness length. The determination scheme may depend on the TM. Most TMs use Tab. 3.1 except for the default TM of ARTM 3.0.0, which uses Tab. 3.2 instead. The profile below $z = d_0 + 6 \cdot z_0$ follows a linear profile down to the surface with $\overline{|\vec{u}(z=0)|} = 0$. The transition from logarithmic to linear profile is continuous (TA Luft 2002).

For the determination of the friction velocity, Eq. 3.1 is evaluated at the height of the measurement data $z = z_{\text{meas}}$ using $u_* = 1\,\text{m s}^{-1}$. The resulting wind speed is denoted with $\overline{|\vec{u}(z_{\text{meas}})|}_{u_*=1\,\text{m s}^{-1}}$. The friction velocity can be seen as a proportional factor between the obtained wind speed at the height of the measurement data when using $u_* = 1\,\text{m s}^{-1}$ and the real, measured wind speed $|\vec{u}_{\text{meas}}|$ and is given by

$$u_* = \frac{|\vec{u}_{\text{meas}}|}{\overline{|\vec{u}(z_{\text{meas}})|}_{u_*=1\,\text{m s}^{-1}}} \cdot 1\,\text{m s}^{-1} \tag{3.3}$$

(Janicke Consulting et al. 2015).

The mixing layer top h_{m} is assumed to be equal to the boundary layer top and depends on the atmospheric stability (Richter et al. 2015a; VDI 3783 part 8 2002). For unstable atmospheric conditions, a mixing layer depth of 1 100 m is used (TA Luft 2002). For all other conditions

$$h_{\text{m}} = \min(H_{\text{m}}, 800\,\text{m}) \tag{3.4}$$

is valid, where

$$H_{\text{m}} = 0.3\frac{u_*}{f_{\text{c}}} \begin{cases} 1 & \text{for } L \geq \dfrac{u_*}{f_{\text{c}}} \\ \left(\dfrac{f_{\text{c}} L}{u_*}\right)^{\frac{1}{2}} & \text{for } 0 < L < \dfrac{u_*}{f_{\text{c}}} \end{cases} \tag{3.5}$$

and f_{c} denotes the Coriolis parameter (TA Luft 2002; Seinfeld 1986).

The wind direction $d_{\text{wind}}(z)$ within the boundary layer is assumed to change with height above ground level (agl) according to an Ekman spiral and is given as

$$d_{\text{wind}}(z) = d_{\text{meas}} + D(z) - D(z_{\text{meas}}) \tag{3.6}$$

with the wind shift at height z

$$D(z) = 1.23 \cdot D_{\text{h}} \cdot \left[1 - \exp\left(-1.75\frac{z}{h_{\text{m}}}\right)\right] \tag{3.7}$$

Table 3.1: Scheme for the determination of the Obukhov length in meter from the SC and the roughness length as it is used by ARTM 2.8.0. After Richter et al. (2015a) from Hanfland et al. (2022).

	Stability class					
Roughness length z_0 (m)	I very stable	II stable	III_1 neutral	III_2 indifferent	IV unstable	V very unstable
0.01	7	25	99999	-25	-10	-4
0.02	9	31	99999	-32	-13	-5
0.05	13	44	99999	-45	-19	-7
0.10	17	60	99999	-60	-25	-10
0.20	24	83	99999	-81	-34	-14
0.50	40	139	99999	-130	-55	-22
1.00	65	223	99999	-196	-83	-34
1.50	90	310	99999	-260	-110	-45
2.00	118	406	99999	-326	-137	-56

Table 3.2: Scheme for the derivation of the Obukhov length in meter from SC and roughness length as it is used by ARTM 3.0.0. After Richter et al. (2020).

	Stability class					
Roughness length z_0 (m)	I very stable	II stable	III_1 neutral	III_2 indifferent	IV unstable	V very unstable
0.01	5	25	354	-37	-15	-6
0.02	7	31	448	-47	-19	-8
0.05	9	44	631	-66	-27	-11
0.10	13	59	842	-88	-36	-15
0.20	17	81	1 160	-122	-49	-20
0.50	28	133	1 893	-199	-80	-33
1.00	44	207	2 951	-310	-125	-52
1.50	60	280	4 000	-420	-170	-70
2.00	77	358	5 107	-536	-217	-89

where the wind shift D_h depends on the Obukhov length as

$$D_\mathrm{h} = \begin{cases} 0° & \text{for } \dfrac{h_\mathrm{m}}{L} < -10 \\ 45° + 4.5\dfrac{h_\mathrm{m}}{L} & \text{for } -10 \leq \dfrac{h_\mathrm{m}}{L} < 0 \\ 45° & \text{for } L > 0 \end{cases} \tag{3.8}$$

and d_meas is the wind direction of the measurement data (TA Luft 2002).

Using the mixing layer depth h_m and the friction velocity u_*, the standard deviation of wind fluctuation σ, the Lagrangian correlation time T_L and the diffusion coefficient K are calculated for each component of the wind vector. The first two quantities (σ and T_L) are sufficient to describe the turbulence and their formulation is denoted as the turbulence model (TM). The x-direction is defined in downwind direction, the y-direction is horizontally perpendicular to it and the z-direction is in vertical direction. The components of the wind fluctuation, as they are used in TALdia 2.7.0 (included in ARTM 2.8.0), are

$$\sigma_\mathrm{x}(z) = \begin{cases} 2.4u_* \left(1 + 0.01486\dfrac{-h_\mathrm{m}}{\kappa L}\right)^{\frac{1}{3}} \exp\left(\dfrac{-z}{h_\mathrm{m}}\right) & \text{for } L < 0 \\ 2.4u_* \exp\left(\dfrac{-z}{h_\mathrm{m}}\right) & \text{for } L > 0 \end{cases} \tag{3.9a}$$

$$\sigma_\mathrm{y}(z) = \begin{cases} 1.8u_* \left(1 + 0.03522\dfrac{-h_\mathrm{m}}{\kappa L}\right)^{\frac{1}{3}} \exp\left(\dfrac{-z}{h_\mathrm{m}}\right) & \text{for } L < 0 \\ 1.8u_* \exp\left(\dfrac{-z}{h_\mathrm{m}}\right) & \text{for } L > 0 \end{cases} \tag{3.9b}$$

$$\sigma_\mathrm{z}(z) = \begin{cases} 1.3u_* \left[\left(1 - 0.8\dfrac{z}{h_\mathrm{m}}\right)^3 \dfrac{-z}{\kappa L} + \exp\left(\dfrac{-z}{h_\mathrm{m}}\right)^3\right]^{\frac{1}{3}} & \text{for } L < 0 \\ 1.3u_* \exp\left(\dfrac{-z}{h_\mathrm{m}}\right) & \text{for } L > 0 \end{cases} \tag{3.9c}$$

for a given grid cell point (VDI 3783 part 8 2002).

The components of the Lagrangian time scale are parametrised according to

$$T_{\mathrm{L}i} = \frac{2\Sigma_i}{\mathrm{C}_0 \eta} \tag{3.10}$$

where $\Sigma_i = \sigma_i^2$ is the variance of the wind fluctuation, i indicates the coordinate ($i = x, y, z$), $\mathrm{C}_0 = 5.7$ denotes the Kolmogorov constant and η is the dissipation

rate of turbulent kinetic energy. Depending on the atmospheric stability, η can be determined empirically (VDI 3783 part 8 2002). For unstable and neutral stratification it can be given as

$$\eta = \max\left\{\frac{u_*^3}{\kappa z}\left[\left(1-\frac{z}{h_\mathrm{m}}\right)^2+\frac{z}{h_\mathrm{m}}\right] + \frac{-u_*^3}{\kappa L}\left[1.5-1.3\left(\frac{z}{h_\mathrm{m}}\right)^{\frac{1}{3}}\right], \frac{u_*^3}{\kappa z}\right\} \tag{3.11}$$

while for stable stratification

$$\eta = \frac{u_*^3}{\kappa z}\left(1+4\frac{z}{L}\right) \tag{3.12}$$

holds.

The corresponding diffusion coefficients K_i are

$$K_i = \Sigma_i T_{\mathrm{L}i}. \tag{3.13}$$

The tensors $\boldsymbol{\Sigma}(x)$, $\boldsymbol{K}(x)$ and $\boldsymbol{T}_\mathrm{L}(x)$ are (3×3)-matrices constructed using the components Σ_i, K_i and $T_{\mathrm{L}i}$ for each grid cell, respectively.

3.1.2 Wind field modelling

In the initialization step $\mathfrak{I}$, an initial wind field is constructed from the measurement data $\vec{u}_\mathrm{meas}$ (Ratto et al. 1994) according to the boundary layer model described above. The wind profile contains a logarithmic shape in the Prandtl layer (up to approx. 200 m agl). For wind flowing perpendicular to a mountain ridge, the wind velocity above the ridge increases. This leads to unrealistic large wind velocities at the ground of the mountain top. Janicke Consulting (2014) described this problem and ARTM uses a modification of the initial wind field by an additional profile $c(z)$ in order to overcome this artefact. The logarithmic shape of the wind profile in the Prandtl layer is removed by multiplying the initial wind field with c^{-1}. The profile $c(z)$ is given as

$$c(z) = \begin{cases} \dfrac{\ln(6)}{\ln\left(\frac{200\,\mathrm{m}-d_0}{z_0}\right)} & \text{for } 0 < z < d_0 + 6z_0, \\ \dfrac{\ln\left(\frac{z-d_0}{z_0}\right)}{\ln\left(\frac{200\,\mathrm{m}-d_0}{z_0}\right)} & \text{for } d_0 + 6z_0 < z \leq 200\,\mathrm{m}, \\ 1 & \text{otherwise} \end{cases} \tag{3.14}$$

(Janicke Consulting et al. 2015). The initial wind field and thus the modified initial wind field $\boldsymbol{V}_0$ do not necessarily fulfil the continuity equation which, assuming

constant air density, is given as

$$\vec{\nabla} \cdot \vec{u} = \frac{\partial u}{\partial x} + \frac{\partial v}{\partial y} + \frac{\partial w}{\partial z} = 0 \tag{3.15}$$

(Ratto 1996). $\vec{u}$ denotes the wind vector while x, y and z are the coordinates in the cartesian coordinate system.

In the adjustment step $\mathfrak{F}$, the initial wind field $\boldsymbol{V}_0$ is then optimized under the constraint of the continuity equation 3.15 to obtain the intermediate wind field $\boldsymbol{V}_{\text{inter}}$ (Janicke Consulting 2014; Ratto et al. 1994). For this purpose, the method presented by Sasaki (1958) and Sasaki (1970) is used where the functional

$$E(u, v, w) = \iiint \frac{1}{2} \left[a_{\text{h}}(u - u^0)^2 + a_{\text{h}}(v - v^0)^2 + a_{\text{v}}(w - w^0)^2 \right] \mathrm{d}x\, \mathrm{d}y\, \mathrm{d}z \tag{3.16}$$

represents the deviation between the initial and the intermediate wind fields (Ratto 1996). u^0, v^0, w^0 and u, v, w are the wind components of the initial and the intermediate wind field, respectively, while a_h and a_v are the horizontal and vertical weighting factors or stability parameters and are termed "Gauss precision moduli" (Sasaki 1958; Sherman 1978). They are constant for the whole simulation domain. For the two horizontal directions identical Gauss precision moduli are assumed (Richter et al. 2015b). The aim is to minimize Eq. 3.16 under the constraint of mass conservation leading to the variational problem

$$\delta \left\{ \iiint \frac{1}{2} \left[a_{\text{h}}(u - u^0)^2 + a_{\text{h}}(v - v^0)^2 + a_{\text{v}}(w - w^0)^2 \right] \mathrm{d}x\, \mathrm{d}y\, \mathrm{d}z + \iiint \lambda \vec{\nabla} \cdot \vec{u}\, \mathrm{d}x\, \mathrm{d}y\, \mathrm{d}z \right\} = 0 \tag{3.17}$$

where δ denotes the first variation and $\lambda = \lambda(x, y, z)$ is the Lagrange multiplier. The Euler-Lagrange equations

$$u = u^0 + \frac{1}{a_{\text{h}}} \frac{\partial \lambda}{\partial x} \tag{3.18a}$$

$$v = v^0 + \frac{1}{a_{\text{h}}} \frac{\partial \lambda}{\partial y} \tag{3.18b}$$

$$w = w^0 + \frac{1}{a_{\text{v}}} \frac{\partial \lambda}{\partial z} \tag{3.18c}$$

give the solution of the variational problem of Eq. 3.17 (Ratto 1996). The substitution of the partial differentials of the continuity equation 3.15 with the Euler-Lagrange equations 3.18 leads to an elliptical equation for λ as

$$\frac{\partial^2 \lambda}{\partial x^2} + \frac{\partial^2 \lambda}{\partial y^2} + \left(\frac{a_{\text{h}}}{a_{\text{v}}} \right) \frac{\partial^2 \lambda}{\partial z^2} = -a_{\text{h}} \left(\frac{\partial u^0}{\partial x} + \frac{\partial v^0}{\partial y} + \frac{\partial w^0}{\partial z} \right) \tag{3.19}$$

which is then solved numerically using the Alternating-Directions Implicit (ADI) method (Press et al. 2002; Richter et al. 2015b). For solving Eq. 3.19 the boundary conditions described in Sec. 3.1.3 are used to ensure the resulting wind field to be free of divergence.

This resulting intermediate wind field $\boldsymbol{V}_{\text{inter}}$ is multiplied by the profile $c(z)$ of Eq. 3.14 to restore the previously removed logarithmic wind profile in the Prandtl layer. According to Janicke Consulting (2014), this workaround leads to lower and thus, more realistic wind velocities at the ground of mountain ridges. The adjustment step $\mathfrak{F}$ is applied again to $c(z) \cdot \boldsymbol{V}_{\text{inter}}$ to obtain the divergence-free final wind field $\boldsymbol{V}$ (Janicke Consulting 2014).

3.1.3 Boundary conditions

In order to obtain a unique solution for the adjustment step $\mathfrak{F}$ (Eq. 3.17), boundary conditions for λ can be specified implicitly from Eq. 3.17 as

$$\lambda \, \delta \vec{u} \cdot \vec{n} = 0 \tag{3.20}$$

on the boundaries in x-, y- and z-direction where δ denotes the first variation normal to each boundary and $\vec{n}$ is the outward unit vector normal to the grid cell surface of the wind field (Sherman 1978; Ratto et al. 1994; Homicz 2002). A detailed derivation is given by Homicz (2002).

Eq. 3.20 is only valid when either i) $\lambda = 0$ or ii) $\delta \vec{u} \cdot \vec{n} = 0$; if both terms i) and ii) are equal to zero there would be no unique solution (Sherman 1978):

i) If $\lambda = 0$ is valid the variation of the normal wind component $\delta \vec{u} \cdot \vec{n}$ at the boundary is not zero. This implies an adjustment of the initial wind field in normal direction at the boundary, which means that there is a change of air mass entering or leaving the grid cell boundary. This is a “flow-through” boundary.

ii) If the variation of the normal wind component is zero ($\delta \vec{u} \cdot \vec{n} = 0$) then there is no adjustment of the initial wind field at the boundary, which implies no air mass change through the boundary. This represents a “no-flow-through” boundary.

Flow-through boundaries are used for the lateral and the top border of the simulation domain while a no-flow-through boundary is used for the bottom of the simulation domain (Janicke et al. 2003).

3.1.4 Parametrisation of atmospheric stability

The Gauss precision moduli a_{h} and a_{v} of Eq. 3.16 serve as an interface to get information about the atmospheric stability into the process of the wind field

modelling (Sherman 1978) and to determine whether an obstacle is passed more likely in horizontal (flow around) or vertical (flow over) direction (Ratto 1996). Both Gauss precision moduli are connected as

$$a_\mathrm{h} = \frac{1}{a_\mathrm{v}} \tag{3.21}$$

where a_v is a function of the Strouhal number Str and defined as

$$a_\mathrm{v} = \frac{1}{2} Str^2 + \sqrt{1 + \frac{1}{4} Str^4}. \tag{3.22}$$

The Strouhal number Str is the product of the Brunt-Väisälä frequency N_BV and a characteristic time t_c as

$$Str = N_\mathrm{BV} \cdot t_\mathrm{c} \tag{3.23}$$

where

$$N_\mathrm{BV} = \sqrt{\frac{\mathrm{a_g}}{\theta} \frac{\mathrm{d}\theta}{\mathrm{d}z}} \tag{3.24}$$

and

$$t_\mathrm{c} = \frac{L_\mathrm{c}}{v_\mathrm{c}}. \tag{3.25}$$

$\mathrm{a_g}$ is the acceleration of gravity and θ is the potential temperature. In the case of unstable and very unstable conditions the potential temperature gradient $\frac{\mathrm{d}\theta}{\mathrm{d}z}$ is assumed zero leading to $a_\mathrm{v} = a_\mathrm{h} = 1$. For other stratifications $\frac{\mathrm{d}\theta}{\mathrm{d}z}$ is determined from the SC and the wind velocity after KTA 1508 (2017, Tab. 7-2). For the characteristic wind velocity $v_\mathrm{c} = v_\mathrm{c}(z)$, the wind profile of the initial wind field $\boldsymbol{V}_0$ at the position of the measurement data is used (Janicke Consulting 2014). L_c is the geometric mean $L_\mathrm{c} = \sqrt{h_\mathrm{c} l_\mathrm{c}}$ of a characteristic height (height of a terrain structure) h_c and a characteristic length l_c given by

$$l_\mathrm{c} = \frac{h_\mathrm{c}}{2\gamma} \tag{3.26}$$

with the average slope within the simulation domain

$$\gamma^2 = \frac{\int \left(\frac{\partial b}{\partial x}\right)^2 + \left(\frac{\partial b}{\partial y}\right)^2 \mathrm{d}x\,\mathrm{d}y}{A_\mathrm{domain}}. \tag{3.27}$$

$b = b(x, y)$ is the terrain elevation and

$$A_\mathrm{domain} = (x_\mathrm{max} - x_\mathrm{min})(y_\mathrm{max} - y_\mathrm{min}) \tag{3.28}$$

is the area of the simulation domain where $x_{\min/\max}$ and $y_{\min/\max}$ represent the edges of the simulation domain in x- and y-direction. The characteristic height h_c is defined as

$$h_c = 4\sqrt{\frac{\int [b(x,y) - \bar{b}\,]^2 \,\mathrm{d}x\,\mathrm{d}y}{A_{\text{domain}}}} \tag{3.29}$$

with the mean terrain elevation

$$\bar{b} = \frac{\int b(x,y)\,\mathrm{d}x\,\mathrm{d}y}{A_{\text{domain}}} \tag{3.30}$$

(Janicke Consulting 2014).

3.1.5 Coordinate system

TALdia uses a height-based terrain-following σ-coordinate system initially presented by Gal-Chen et al. (1975). In the simulation domain the vertical coordinate z is zero at the bottom of the domain while the top of the simulation domain is denoted as $\hat{z} = \text{const}$ (Gal-Chen et al. 1975). Positions between the terrain surface b and the domain top $\hat{z}$ can be expressed as $h = z - b$. It is assumed that $\hat{z} \to \infty$ leading to $\hat{h} = \hat{z}$ (Janicke Consulting 2014). For the terrain-following coordinate system a new vertical coordinate s is introduced as

$$s(x,y) = \hat{h}(x,y) \cdot \sigma = \hat{h}(x,y) \cdot \frac{z(x,y) - b(x,y)}{\hat{z}(x,y) - b(x,y)} \tag{3.31}$$

(Janicke Consulting 2014; Ratto 1996; Gal-Chen et al. 1975).

At the terrain surface $z(x,y) = b(x,y)$ is valid and thus the coordinate s is always zero at the surface. At the top of the domain $z(x,y) = \hat{z}(x,y)$ and therefore $s = \hat{h} = \hat{z}$ (Ratto et al. 1994; Janicke Consulting 2014). For the case of a flat surface (no terrain is present) the vertical coordinate remains unchanged $s = z$.

The vertical component of the wind speed is also transformed and used in ARTM. The vertical velocity w_s within the terrain-following coordinate system is obtained by differentiating Eq. 3.31 with respect to time leading to

$$w_s = w - \left(\frac{\partial b}{\partial x}u + \frac{\partial b}{\partial y}v\right) \tag{3.32}$$

with the original vertical velocity w (Janicke Consulting 2014). A detailed derivation is given by Gal-Chen et al. (1975).

3.2 The particle dispersion model

The ARTM version 2.8.0 uses the particle dispersion model suggested by the Association of German Engineers (VDI) guideline 3945 part 3 in combination with VDI guideline 3782 part 3 for the plume rise (VDI 3945 part 3 2000; VDI 3782 part 3 1985; Richter et al. 2015a; Janicke Consulting 2014). The model also contains radionuclide specific features such as radioactive decay, dry and wet deposition and γ-cloud shine.

3.2.1 The transport

The transport is modelled according to Eq. 2.32 at page 25 for LPDMs. In order to simplify the follow up formalism, I repeat the equation using different indices as

$$\vec{x}_{\text{new}} = \vec{x}_{\text{old}} + \tau \Big[\underbrace{\vec{\overline{u}}(\vec{x}_{\text{old}}) + \vec{u'} + \vec{u}_{\text{add}}}_{\vec{u}_{\text{trans}}} \Big] \tag{3.33}$$

with the new (old) particle positions $\vec{x}_{\text{new(old)}}$, the average velocity $\vec{\overline{u}}$ and the turbulent velocity $\vec{u'}$ representing the Reynolds decomposition of the wind vector (VDI 3945 part 3 2000; Mesinger et al. 1976). $\vec{u}_{\text{add}}$ is an additional velocity vector representing e.g. sedimentation or buoyancy, $\vec{u}_{\text{trans}}$ denotes the transport velocity and $\vec{x}_{\text{old}}$ is the former particle position. The time steps τ are small compared to the Lagrangian correlation time and they are in the order of seconds to tens of seconds in practice.

$\vec{\overline{u}}$ is obtained by spatial interpolation from the final wind field $\boldsymbol{V}$ at the particle position (see Sec. 3.1.2) and is constant for the time $t = 1\,\text{h}$ while the turbulent velocity $\vec{u'}$ changes for each $\tau \ll t$ according to the Markov process

$$\vec{u'} = \boldsymbol{\Psi}(\vec{x}_{\text{old}}) \cdot \vec{u'}_{\text{old}} + \vec{W}(\vec{x}_{old}) + \boldsymbol{\Lambda}(\vec{x}_{old}) \cdot \vec{r} \tag{3.34}$$

(VDI 3945 part 3 2000). $\boldsymbol{\Psi}$ is the autocorrelation tensor and given as

$$\boldsymbol{\Psi} \approx \boldsymbol{I} - \tau(\vec{x}) \left(\boldsymbol{\Sigma} \cdot \boldsymbol{K}^{-1} \right) \tag{3.35}$$

with the identity matrix $\boldsymbol{I}$, $\vec{W}$ is the drift velocity

$$\vec{W} \approx \tau(\vec{x}) \vec{\nabla} \cdot \boldsymbol{\Sigma}, \tag{3.36}$$

$\boldsymbol{\Lambda}$ is the Cholesky decomposition of a tensor $\boldsymbol{\Omega}$ given as

$$\boldsymbol{\Omega} = \boldsymbol{\lambda}\boldsymbol{\lambda}^{\mathsf{T}} \approx \tau(\vec{x}) \left[\left(\boldsymbol{\Sigma} \cdot \boldsymbol{K}^{-1} \right) \cdot \boldsymbol{\Sigma} + \boldsymbol{\Sigma} \cdot \left(\boldsymbol{\Sigma} \cdot \boldsymbol{K}^{-1} \right)^{\mathsf{T}} \right] \tag{3.37}$$

and $\vec{r}$ is a random vector with its components following a standard normal probability density distribution (Janicke 2000). The tensors $\boldsymbol{\Sigma}$ and $\boldsymbol{K}$ are obtained from the boundary layer model described in Sec. 3.1.1.

The Eqs. 3.35 to 3.37 are derived under the assumptions of i) the additional velocity is zero ($\vec{u}_{\text{add}} = 0$); ii) there are suitable boundary conditions to obtain a homogeneous steady state particle distribution; iii) in such a homogeneous steady state particle distribution the mean wind speed and its variance is equal to the mean particle velocity and its variance, respectively; iv) at time scales much larger then the Lagrangian correlation time a particle cloud spreads like the classic diffusion equation predicts; and v) the small time steps $\tau(\vec{x})$ depend on the location. Using location dependent time steps τ avoids very small time steps in the whole simulation domain and keeps the model computational efficient (VDI 3945 part 3 2000). A detailed derivation of Eqs. 3.35 to 3.37 is given by Janicke (2000).

3.2.2 Particle initialisation and boundary conditions

All numerical particles start either as a point, line, area or volume source. In the latter cases the numerical particles are distributed randomly within the line, area or volume source. The initial turbulent velocity of each numerical particle is chosen randomly according to a standard normal distribution with the mean value $\overrightarrow{u'} = \boldsymbol{\Sigma}(\vec{x})$ and the standard deviation $\sigma_{\text{norm}} = 1\,\text{m}\,\text{s}^{-1}$ (VDI 3945 part 3 2000).

Particles crossing the upper and lateral boundaries of the simulation domain are erased from the simulation. At the terrain surface, numerical particles are elastically reflected instantaneously (with deposition for PM as described in Sec. 3.2.4) and their turbulent velocity is changed to

$$\vec{u'}_{\text{new}} = \vec{u'}_{\text{old}} - 2(\vec{n} \cdot \vec{u'}_{\text{old}}) \cdot \vec{n} \tag{3.38}$$

(VDI 3945 part 3 2000).

The upper boundary of the mixing layer within the simulation domain can be crossed by the numerical particles. The atmosphere above the mixing layer is modelled as a region with no diffusion ($\vec{u'} = 0$) (VDI 3945 part 3 2000; GRS 2015).

3.2.3 The plume rise

Usually a rise of the plume relative to the emission height occurs due to buoyancy and inertia (Briggs 1971). In ARTM emissions are divided into two categories, emissions with heat content Q lower or higher than 1.4 MW. The heat Q in MW is calculated as

$$Q = c_{\text{p}} \cdot R_{\text{norm}} \, (T_{\text{e}} - 283.15\,\text{K}) \tag{3.39}$$

with $c_\mathrm{p} = 1.36 \cdot 10^{-3}\,\mathrm{MW\,s\,m^{-3}\,K^{-1}}$ being the specific heat capacity for the emissions of a pit coal fire, R_norm being the volume flux under standard conditions (temperature $T = 273.15\,\mathrm{K}$ and pressure $p = 1013.25\,\mathrm{hPa}$) and T_e being the temperature of the emissions (VDI 3782 part 3 1985).

For the first case ($Q \leq 1.4\,\mathrm{MW}$), the momentum plays a significant role for the plume rise (VDI 3782 part 3 1985). Thus, according to Moses et al. (1968) the maximum plume rise (relative to the height of the source agl) is given as

$$h_\mathrm{max} = \max\left(h_\mathrm{b}, h_\mathrm{i}\right) \tag{3.40}$$

with

$$h_\mathrm{b} = \left(0.35 \cdot w_\mathrm{emission} \cdot d_\mathrm{source} + 84 \cdot Q^{\frac{1}{2}}\right) |\vec{u}_h|^{-1} \tag{3.41}$$

and

$$h_\mathrm{i} = 3 \cdot w_\mathrm{emission} \cdot d_\mathrm{source} \cdot |\vec{u}_h|^{-1}. \tag{3.42}$$

w_emission denotes the vertical velocity of the emission flux, d_source is the diameter of the source and $|\vec{u}_h|$ is the horizontal wind velocity in the height of the source taken from the final wind field $\boldsymbol{V}$ (GRS 2015). Equations 3.40 to 3.42 are valid for all turbulence conditions in the atmosphere (VDI 3782 part 3 1985). The horizontal distance between the source and the maximum plume rise depends only on the heat Q and is given as

$$|\vec{x}_{h_\mathrm{max}}| = 209.8 \cdot Q^{0.522}. \tag{3.43}$$

For the second case ($Q > 1.4\,\mathrm{MW}$), the calculation depends on the turbulence in the atmosphere (VDI 3782 part 3 1985). Following Briggs, the horizontal distance from the source to the maximum plume rise is determined by

$$|\vec{x}_{h_\mathrm{max}}| = \exp\left[\frac{\ln\left(\frac{h_\mathrm{max} \cdot |\vec{u}_h|}{\alpha}\right) - \chi \ln Q}{q}\right] \tag{3.44}$$

(VDI 3782 part 3 1985; Briggs 1971). The empirical parameters α, χ and q depend on the atmospheric stability and the heat Q and are summarized in Tab. 3.3. The maximum plume rise h_max for this case is calculated according to

$$h_\mathrm{max} = \beta \cdot Q^{\epsilon} \cdot |\vec{u}_h|^{\gamma_e} \tag{3.45}$$

with the empirical parameters β, ϵ and γ_e given in Tab. 3.3 (Briggs 1971; VDI 3782 part 3 1985).

After the determination of h_max and $|\vec{x}_{h_\mathrm{max}}|$ an additional vertical velocity $\vec{w}_\mathrm{pr}$ for the numerical particles due to the plume rise is calculated as

$$\vec{w}_\mathrm{pr} = \frac{h_\mathrm{max}}{t_\mathrm{rise}} \tag{3.46}$$

Table 3.3: Values of the parameters in Eqs. 3.44 and 3.45 for the different SCs and heat contents Q. After VDI 3782 part 3 (1985). From Hanfland et al. (2022).

	stability class					
	I	II	$III_1 + III_2$		IV + V	
	very stable	stable	neutral	indifferent	unstable	very unstable
	$Q > 1.4\,MW$		$1.4\,MW < Q \leq 6\,MW$	$Q > 6\,MW$	$1.4\,MW < Q \leq 6\,MW$	$Q > 6\,MW$
α	3.34	3.34	2.84	2.84	3.34	3.34
χ	0.333	0.333	0.333	0.333	0.333	0.333
q	0.667	0.667	0.667	0.667	0.667	0.667
β	74.4	85.2	78.4	102	112	146
ϵ	0.333	0.333	0.750	0.600	0.750	0.600
γ_e	−0.333	−0.333	−1	−1	−1	−1

where

$$t_{\text{rise}} = 0.4 \cdot \frac{|\vec{x}_{h_{\max}}|}{|\vec{u}_h|} \tag{3.47}$$

denotes the rise time. A numerical particle is assumed to move vertically with $\vec{w}_{\text{pr}}$ beginning from its release at the source until t_{rise} is reached (GRS 2015).

The given equations for the plume rise are only valid for emissions from sources with a vertical flux not influenced by obstacles. In the case of wind speeds at source height lower than $1\,\text{m s}^{-1}$ it is substituted with $|\vec{u}_h| = 1\,\text{m s}^{-1}$. Latent heat in the discharge is explicitly excluded (VDI 3782 part 3 1985).

3.2.4 Sedimentation, dry and wet deposition

The sedimentation of PM is realised by numerical particles with an additional velocity $\vec{u}_{\text{add}}$ in the transport equation 3.33. Sedimentation velocities used by ARTM depend on the aerodynamic diameter of particulate matter (VDI 3945 part 3 2000). The five size classes ARTM uses for PM are given in Tab. 3.4 together with their sedimentation velocities.

Each numerical particle represents a mass and may carry an activity a_ν of a real particle species ν. If such a numerical particle hits an obstacle or the terrain surface, a fraction $\zeta_{\nu,\text{dry}}$ of its activity a_ν is deposited. After this process the new

Table 3.4: Size classes for particulate matter (PM) used in ARTM with their aerodynamic diameters d_{aero} in µm, sedimentation velocities w_{sed} in $\mathrm{m\,s^{-1}}$, deposition velocities u_{dep} in $\mathrm{m\,s^{-1}}$ and washout coefficients $r^0_{\nu,\text{w}}$ in $\mathrm{s^{-1}}$ for a precipitation rate of $1\,\mathrm{mm\,s^{-1}}$ after Richter et al. (2015b). From Hanfland et al. (2022).

Size Class	d_{aero} in µm	w_{sed} in $\mathrm{m\,s^{-1}}$	u_{dep} in $\mathrm{m\,s^{-1}}$	$r^0_{\nu,\text{w}}$ in $\mathrm{s^{-1}}$
PM 1	$d_{\text{aero}} < 2.5$	0.00	0.001	$1 \cdot 10^{-4}$
PM 2	$2.5 \leq d_{\text{aero}} < 10$	0.00	0.01	$2 \cdot 10^{-4}$
PM 3	$10 \leq d_{\text{aero}} \leq 50$	0.04	0.05	$3 \cdot 10^{-4}$
PM 4	$50 < d_{\text{aero}}$	0.15	0.20	$4 \cdot 10^{-4}$
PM u	$10 < d_{\text{aero}}$	0.06	0.07	$3 \cdot 10^{-4}$

activity of the particle is given by

$$a_{\nu,\text{new}} = (1 - \zeta_{\nu,\text{dry}})\, a_{\nu,\text{old}}. \tag{3.48}$$

The factor $\zeta_{\nu,\text{dry}}$ is given as

$$\zeta_{\nu,\text{dry}} = \frac{2\, u_{\text{dep}}}{u_{\text{dep}} + w_{\text{sed}} + \sigma_{w,0}\, \sqrt{\frac{2}{\pi}}\, f_{\text{p}}} \tag{3.49}$$

where

$$f_{\text{p}} = \frac{\exp\left(-\frac{w_{\text{sed}}^2}{2\sigma_{w,0}^2}\right)}{1 + \operatorname{erf}\left(\frac{w_{\text{sed}}}{\sigma_{w,0}\sqrt{2}}\right)}, \tag{3.50}$$

u_{dep} is the deposition velocity given in Tab. 3.4 and $\sigma_{w,0}$ is the vertical wind fluctuation close to the ground (Janicke 1985; VDI 3945 part 3 2000). The deposition velocities for mercury and iodine in their organic bounded form are $0.0001\,\mathrm{m\,s^{-1}}$ and in their elementary form are $0.01\,\mathrm{m\,s^{-1}}$, respectively. The particle is elastically reflected and its turbulent velocity is changed according to Eq. 3.38.

Wet deposition denotes the deposition due to washout by precipitation and thus, also activity deposition occurs. For each particle species a specific washout coefficient $r^0_{\nu,\text{w}}$ is defined which is used to obtain the washout factor

$$r_{\nu,\text{w}} = r^0_{\nu,\text{w}} \cdot \phi^a_{\text{prec}} \tag{3.51}$$

where ϕ_{prec} is the precipitation rate and a is a tracer specific exponent which may have i) a value of $a = 0.8$ for PM and iodine isotopes or ii) a value of $a = 1$ for

tritiated water (AVV 2012; Richter et al. 2015a). The activity fraction remaining in the atmosphere is given by

$$a_{\nu,\text{new}} = (1 - r_{\nu,\text{w}}\tau)\, a_{\nu,\text{old}} \tag{3.52}$$

(VDI 3945 part 3 2000).

The washout coefficients for the precipitation rate 1 mm h^{-1} of radionuclides as PM are given in Tab. 3.4. Washout coefficients for organic bounded mercury and iodine are $7 \cdot 10^{-7}\,\text{s}^{-1}$, in their elementary form they are $7 \cdot 10^{-5}\,\text{s}^{-1}$, respectively. The activity of a grid cell bottom area due to wet deposited originates from the vertical column above the bottom area to the top of the simulation domain (VDI 3945 part 3 2000).

3.2.5 Radioactive decay

The radioactive decay of numerical particles is represented as an exponential decay of the activity of a radioactive species as

$$a_{\nu,\text{new}} = a_{\nu,\text{old}} \cdot \exp\left(-\tau\lambda_{\text{decay}}\right) \tag{3.53}$$

where λ_{decay} is the constant of decay for the corresponding radionuclide. Radioactive decay is only considered for numerical particles in the air not on the ground. Daughter products are not considered in ARTM (Richter et al. 2015a).

3.2.6 Activity concentration distribution

The simulation domain is divided into grid cells with coordinate indices i, j, k where the volume of a grid cell is denoted $V_{i,j,k}$. The activity concentration of a particle species ν consists of spatio-temporal mean activity concentration $\overline{a^{\nu}_{i,j,k}}$ within each grid cell and the time interval $[t_0, t_1]$. During this time interval, all numerical particles n with activity concentration $a_{\nu,n}$ contribute to the grid cell's mean activity concentration $\overline{a^{\nu}_{i,j,k}}$ for $n = 1 \ldots N$.N is the total particle number. Using the step function

$$f^{(n)}_{i,j,k}(t) = \begin{cases} 1 & \text{the particle } n \text{ is inside } V_{i,j,k} \text{ at time } t, \\ 0 & \text{otherwise} \end{cases} \tag{3.54}$$

for each numerical particle to decide at which time the particle contributes to the grid cell, the mean activity concentration can be calculated as

$$\overline{a^{\nu}_{i,j,k}} = \frac{\sum_{n=1}^{N} \int_{t_0}^{t_1} f^{(n)}_{i,j,k}(t) \cdot a_{\nu,n}(t)\,\mathrm{d}t}{V_{i,j,k} \cdot (t_1 - t_0)} \tag{3.55}$$

(VDI 3945 part 3 2000).

3.2.7 Activity deposition rate distribution

The calculation of the dry activity deposition rate is similar to the calculation of the activity concentration distribution. The grid cells divide the terrain surface into areas $A_{l,m}$ where l and m identify the grid cells in x- and y-direction. At a certain point in time $t_{l,m}^{(n)}$ the particle n hits the terrain surface area $A_{l,m}$ and deposits a fraction $\zeta_{\nu,\mathrm{dry}}$ of its activity. Thus, for a time interval $[t_0, t_1]$ the dry deposition rate is calculated as

$$\overline{d_{l,m}^{\nu}} = \frac{\sum_{n=1}^{N} \int_{t_0}^{t_1} \delta(t - t_{l,m}^{(n)}) \cdot \zeta_{\nu,\mathrm{dry}} \cdot a_{\nu,n}(t)\,\mathrm{d}t}{A_{l,m} \cdot (t_1 - t_0)} \tag{3.56}$$

(VDI 3945 part 3 2000).

3.2.8 γ-cloud shine

Radioactive isotopes - as part of the exhaust plume - may radiate γ-rays to all directions in space (Hallenbeck 1994). The γ-radiation of the plume at the terrain surface is called γ-cloud shine and is calculated by ARTM based on the grid cells (Richter et al. 2015a). The γ-radiation $G(x_{\mathrm{lm}}, y_{\mathrm{lm}})$ to the area of a grid cell at the surface with coordinates l and m is given as

$$G(x_{\mathrm{lm}}, y_{\mathrm{lm}}) = \sum_{i,j,k} \overline{a_{i,j,k}^{\nu}} \int_{V_{i,j,k}} \frac{B(\mu R_{l,m}^{i,j,k}) K(\mu z, \mu S_{l,m}^{i,j,k}) \exp\left(-\mu R_{l,m}^{i,j,k}\right)}{4\pi {R_{l,m}^{i,j,k}}^2} \,\mathrm{d}x\,\mathrm{d}y\,\mathrm{d}z \tag{3.57}$$

where B is the dose buildup factor, μ is the aggregate attenuation coefficient, K is the correction factor for influences of the ground, S is the horizontal distance from the source of the γ-ray to the observed grid cell and R is the three-dimensional distance, respectively (VDI 3945 part 3 2000; Richter et al. 2015a).

The dose buildup factor B depends on the radiation energy. For simplicity, the energy spectrum is divided into two parts at 0.2 MeV. Energies of the lower (upper) part of the spectrum are approximated with coefficients for $E = 0.1\,\mathrm{MeV}$ ($E = 1\,\mathrm{MeV}$), respectively (Richter et al. 2015a). Thus, the dose buildup factor is approximated as

$$B_E(\mu_E \cdot R) = 1 + \sum_{f=1}^{5} b_{E;f} \cdot (\mu_E \cdot R)^f \quad \text{for } E \in \{0.1\,\mathrm{MeV}, 1\,\mathrm{MeV}\} \tag{3.58}$$

with the aggregate attenuation coefficients $\mu_{1\,\mathrm{MeV}} = 7.78 \cdot 10^{-3}\,\mathrm{m}^{-1}$ (AVV 2012; Richter et al. 2015a) and $\mu_{0.1\,\mathrm{MeV}} = 1.82 \cdot 10^{-2}\,\mathrm{m}^{-1}$ (Jacob et al. 1984; Richter et al.

2015a). Values for the coefficients $b_{E;f}$ are summarized in Tab. 3.5. The coefficients $b_{1\,\mathrm{MeV};f}$ are only valid if $\mu_{1\,\mathrm{MeV}} \cdot R < 15$, for higher values $B_{1\,\mathrm{MeV}}(\mu_{1\,\mathrm{MeV}} \cdot R \geq 15) = B_{1\,\mathrm{MeV}}(15)$ is used (AVV 2012; Richter et al. 2015a).

Table 3.5: Coefficients $b_{E;f}$ for the calculation of the dose buildup factors in Eq. 3.58 after Richter et al. (2015a) for energies of 0.1 MeV and after AVV (2012) for energies of 1 MeV. From Hanfland et al. (2022)

Energy	$f = 1$	$f = 2$	$f = 3$	$f = 4$	$f = 5$
0.1 MeV	1.92	1.74	$-3.39 \cdot 10^{-2}$	$3.86 \cdot 10^{-2}$	$-2.11 \cdot 10^{-3}$
1 MeV	$7.7 \cdot 10^{-1}$	$3.5 \cdot 10^{-1}$	$-4.0 \cdot 10^{-2}$	$3.2 \cdot 10^{-3}$	$-8.2 \cdot 10^{-5}$

The correction coefficient for the influence of the ground K is approximated as

$$K_E(\mu_E \cdot z, \mu_E \cdot S) \approx \sum_{f=0}^{3} \sum_{g=0}^{3} a_{f,g} (\mu_E \cdot z)^f \cdot \exp\left(-\frac{g}{2} \cdot \mu_E \cdot S\right) \quad \text{for } E \in \{0.1\,\mathrm{MeV}, 1\,\mathrm{MeV}\} \tag{3.59}$$

where the coefficient $a_{f,g}$ is taken from Tab. 3.6 (Jacob et al. 1985; Richter et al. 2015a; AVV 2012).

Table 3.6: Coefficients $a_{f,g}$ for the calculation of the correction coefficients for the influence of the ground K_E after Jacob et al. (1985). From Hanfland et al. (2022).

	0.1 MeV			
	$g = 0$	$g = 1$	$g = 2$	$g = 3$
$f = 0$	0.279	0.595	−0.205	0.622
$f = 1$	0.135	0.866	−0.716	−0.578
$f = 2$	−0.0131	−0.324	0.1103	0.2892
$f = 3$	0.0003	0.0313	−0.0017	−0.0337
	1 MeV			
	$g = 0$	$g = 1$	$g = 2$	$g = 3$
$f = 0$	0.485	0.064	1.705	−1.179
$f = 1$	0.137	1.878	−4.817	2.883
$f = 2$	−0.0035	−0.8569	2.0527	−1.2552
$f = 3$	−0.0018	0.0997	−0.2392	0.1503

For the calculation of the γ-cloud shine, the integration of Eq. 3.57 is solved using Gaussian Quadratures (Press et al. 2002; Richter et al. 2015a). The calculation is straight forward for all grid cells except for the case where the grid cell of radiance also contains emitters. In that case, a coordinate transformation to polar coordinates is necessary in order to omit a singularity in the integrand of Eq. 3.57. Details about the calculation are given by Richter et al. (2015a).

3.2.9 Sample Error

In ARTM the simulation results consist of concentration fields, fields for dry and wet deposition and fields for the γ-cloud shine. All this fields are given with associated uncertainties that represent the sample error. Assuming we observe one molecule that is represented by a numerical particle. Molecular diffusion is neglected because it is small compared to the turbulent diffusion. During the dispersion the molecule is transported by advection and turbulent diffusion. In ARTM the corresponding numerical particle is propagated by the mean wind (advection) and the turbulent wind speed that is associated with the turbulent diffusion. The turbulent diffusion is modelled as a stochastic process, i.e. the trajectory of the numerical particle represents just one possible realisation of all possible trajectory of the associated molecule. This is valid for all the numerical particle trajectories simulated by ARTM. The resulting concentration fields of a simulation are thus only one representation of all the possible representations and they are subject to a certain uncertainty. ARTM estimates this uncertainty as the sample error (Janicke Consulting 2014). Other common names are the standard error of the mean or just the standard error and it characterises the uncertainty in the mean calculated concentrations as the best estimate for the actual concentration (Taylor 1997).

In ARTM the set of numerical particles of one simulation run is internally split into N_g sub-sets. This is the equivalent to an ensemble with N_g members. The dispersion simulations of all sub-sets use the same initial and boundary conditions but the turbulent diffusion of each sub-set of numerical particles is simulated independently. This means that each sub-set uses its own unique set of pseudo-random numbers for the simulation of the turbulent velocities. ARTM uses the N_g sub-sets to estimate the sample error of the concentration for each grid cell of the simulation domain (GRS 2015; Janicke Consulting 2022).

Statistical background

Assuming X is a random variable forming the population $X = \{X_1, X_2, \ldots, X_N\}$. The population mean μ or population expected value $E(X)$ is

$$\mu = E(X) = \sum_{i=1}^{N} X_i P_i \tag{3.60}$$

where P_i is the probability of the value X_i. If X is uniformly distributed all P_i are equal. Sometimes the population mean is written as $\mu = \langle X \rangle$.

The variance of a population $\mathrm{Var}(X) = \sigma_X^2$ is the weighted sum of the squared difference from the mean

$$\mathrm{Var}(X) = \sigma_X^2 = \sum_{i=1}^{N} (X_i - \mu)^2 P_i. \tag{3.61}$$

If we only assume a sub-set of the population as a sample $x = \{x_1, x_2, \ldots, x_n\}$ then the sample mean $\overline{x}$ is different from the above population mean μ as

$$\overline{x} = \sum_{i=1}^{n} x_i p_i \tag{3.62}$$

with the probability p_i of x_i. We assume that x is uniformly distributed with $p_i = \frac{1}{n}$. The sample variance can be expressed as

$$\mathrm{Var}(x) = \sigma_x^2 = \frac{1}{n} \sum_{i=1}^{n} (x_i - \overline{x})^2 \tag{3.63}$$

or as the unbiased sample variance

$$\mathrm{Var}(x) = \sigma_x^2 = \frac{1}{n-1} \sum_{i=1}^{n} (x_i - \overline{x})^2 \tag{3.64}$$

which includes a correction (Taylor 1997).

The deviation of the sample mean $\overline{x}$ from the population mean μ can be expressed as the variance of the sample mean

$$\begin{aligned} \mathrm{Var}(\overline{x}) = \sigma_{\overline{x}} = \mathrm{Var}\left(\frac{1}{n} \sum_{i=1}^{n} x_i \right) &\overset{1)}{=} \frac{1}{n^2} \mathrm{Var}\left(\sum_{i=1}^{n} x_i \right) \\ &\overset{2)}{=} \frac{1}{n^2} \sum_{k=1}^{n} \mathrm{Var}\left(x_k\right) = \frac{1}{n^2} n \cdot \mathrm{Var}(x) = \frac{1}{n^2} n \cdot \sigma_x^2 = \frac{\sigma_x^2}{n} \end{aligned} \tag{3.65}$$

where at 1)

$$\begin{aligned}\mathrm{Var}(aX) &= \frac{1}{n}\sum_{i=1}^{n}\left(aX_i - a\overline{X}\right)^2 = \frac{1}{n}\sum_{i=1}^{n}\left(a^2X^2 - 2a^2X\overline{X} + a^2\overline{X}^2\right) \\ &= \frac{1}{n}\sum_{i=1}^{n}a^2\left(X^2 - 2X\overline{X} + \overline{X}^2\right) = a^2\frac{1}{n}\sum_{i=1}^{n}\left(X - \overline{X}\right)^2 \\ &= a^2\,\mathrm{Var}(X) \end{aligned} \tag{3.66}$$

was used and at 2) Bienaymé's identity was applied. It states that for pairwise independent samples x_1 and x_2 the sum of the variances is equal to the variance of the sum

$$\mathrm{Var}(x_1 + x_2) = \mathrm{Var}(x_1) + \mathrm{Var}(x_2) \tag{3.67}$$

(Press et al. 2002). The square root of Eq. 3.65 is defined as the standard error (Taylor 1997).

Calculation of the sample error

In the following, for simplicity, we focus on one single gird cell of the simulation domain. The calculation of the sample error for the other grid cells is analogue. In ARTM the shortest evaluation time period h is one hour. For each sub-set one activity value $a_{h,n}$ with $n = 1 \ldots N_\mathrm{g}$ is given for the observed grid cell. Summing over all N_g sub-sets results in

$$s_h = \sum_{n=1}^{N_\mathrm{g}} a_{h,n}. \tag{3.68}$$

This sum can also be estimated by multiplying the activity value of one single sub-set with the number of all sub-sets

$$A_{h,n} = N_\mathrm{g} \cdot a_{h,n}. \tag{3.69}$$

The mean of the estimates $A_{h,n}$ using the activity values from all sub-sets given as

$$M_h = \frac{1}{N_\mathrm{g}}\sum_{n=1}^{N_\mathrm{g}} A_{h,n} = \frac{1}{N_\mathrm{g}}\sum_{n=1}^{N_\mathrm{g}}(N_\mathrm{g} \cdot a_{h,n}) = \sum_{n=1}^{N_\mathrm{g}} a_{h,n} = s_\mathrm{h} \tag{3.70}$$

is equal to the sum of all activity values given in Eq. 3.68. This sample mean M_h deviates from the population mean μ_h, where $N_\mathrm{g} \to \infty$ or the number of numerical particles $\to \infty$. The deviation of M_h from its expected value μ_h is given by the mean squared error (variance) as

$$\sqrt{\mathrm{Var}(M_h)} = \sqrt{\frac{\sigma^2_{A_{h,n}}}{N_\mathrm{g}}} \overset{Eq.3.64}{=} \left[\frac{1}{N_\mathrm{g}(N_\mathrm{g}-1)}\sum_{n=1}^{N_\mathrm{g}}(A_{h,n} - M_h)^2\right]^{\frac{1}{2}}$$

$$
\begin{aligned}
&= \left[\frac{1}{N_\mathrm{g}(N_\mathrm{g}-1)} \sum_{n=1}^{N_\mathrm{g}} \left(A_{h,n}^2 - 2A_{h,n}M_h + M_h^2 \right) \right]^{\frac{1}{2}} \\
&= \left[\frac{1}{N_\mathrm{g}(N_\mathrm{g}-1)} \left(\sum_{n=1}^{N_\mathrm{g}} A_{h,n}^2 - \sum_{n=1}^{N_\mathrm{g}} 2A_{h,n}M_h + \sum_{n=1}^{N_\mathrm{g}} M_h^2 \right) \right]^{\frac{1}{2}} \\
&= \left\{ \frac{1}{N_\mathrm{g}(N_\mathrm{g}-1)} \left[\sum_{n=1}^{N_\mathrm{g}} (N_\mathrm{g} \cdot a_{h,n})^2 - \sum_{n=1}^{N_\mathrm{g}} 2A_{h,n}M_h + \sum_{n=1}^{N_\mathrm{g}} M_h^2 \right] \right\}^{\frac{1}{2}} \\
&= \left\{ \frac{1}{N_\mathrm{g}(N_\mathrm{g}-1)} \left[\sum_{n=1}^{N_\mathrm{g}} (N_\mathrm{g} \cdot a_{h,n})^2 - 2M_h \sum_{n=1}^{N_\mathrm{g}} A_{h,n} + \sum_{n=1}^{N_\mathrm{g}} M_h^2 \right] \right\}^{\frac{1}{2}} \\
&\overset{Eq.3.70}{=} \left\{ \frac{1}{N_\mathrm{g}(N_\mathrm{g}-1)} \left[\sum_{n=1}^{N_\mathrm{g}} (N_\mathrm{g} \cdot a_{h,n})^2 - 2M_h \cdot N_\mathrm{g} \cdot M_h + \sum_{n=1}^{N_\mathrm{g}} M_h^2 \right] \right\}^{\frac{1}{2}} \\
&= \left\{ \frac{1}{N_\mathrm{g}(N_\mathrm{g}-1)} \left[\sum_{n=1}^{N_\mathrm{g}} (N_\mathrm{g} \cdot a_{h,n})^2 - 2N_\mathrm{g}M_h^2 + \sum_{n=1}^{N_\mathrm{g}} M_h^2 \right] \right\}^{\frac{1}{2}} \\
&= \left\{ \frac{1}{N_\mathrm{g}(N_\mathrm{g}-1)} \left[\sum_{n=1}^{N_\mathrm{g}} (N_\mathrm{g} \cdot a_{h,n})^2 - 2N_\mathrm{g}M_h^2 + N_\mathrm{g} \cdot M_h^2 \right] \right\}^{\frac{1}{2}} \\
&= \left\{ \frac{1}{N_\mathrm{g}(N_\mathrm{g}-1)} \left[N_\mathrm{g}^2 \sum_{n=1}^{N_\mathrm{g}} a_{h,n}^2 - 2N_\mathrm{g}M_h^2 + N_\mathrm{g} \cdot M_h^2 \right] \right\}^{\frac{1}{2}} \\
&= \left\{ \frac{1}{N_\mathrm{g}(N_\mathrm{g}-1)} \left[N_\mathrm{g}^2 \sum_{n=1}^{N_\mathrm{g}} a_{h,n}^2 - N_\mathrm{g}M_h^2 \right] \right\}^{\frac{1}{2}} \\
&= \left\{ \frac{1}{N_\mathrm{g}-1} \left[N_\mathrm{g} \sum_{n=1}^{N_\mathrm{g}} a_{h,n}^2 - M_h^2 \right] \right\}^{\frac{1}{2}} \\
&\overset{Eq.3.70}{=} \left\{ \frac{1}{N_\mathrm{g}-1} \left[N_\mathrm{g} \sum_{n=1}^{N_\mathrm{g}} a_{h,n}^2 - s_h^2 \right] \right\}^{\frac{1}{2}} \\
&= \left\{ \frac{1}{N_\mathrm{g}-1} \left[N_\mathrm{g} \cdot q_h - s_h^2 \right] \right\}^{\frac{1}{2}} \qquad (3.71)
\end{aligned}
$$

where

$$
q_h = \sum_{n=1}^{N_\mathrm{g}} a_{h,n}^2 \qquad (3.72)
$$

is the sum of squared activities of the time period h (Janicke Consulting 2022).

Now, assuming two sequential time periods $h = \mathfrak{h}, \mathfrak{h}+1$ and applying the identity of Bienaymé's (Eq. 3.67) the standard error can be expressed as

$$\begin{aligned}
\sqrt{\mathrm{Var}(M_{\mathfrak{h}} + M_{\mathfrak{h}+1})} = [\mathrm{Var}(M_{\mathfrak{h}}) + \mathrm{Var}(M_{\mathfrak{h}+1})]^{\frac{1}{2}} &= \left(\frac{\sigma^2_{A_{\mathfrak{h},n}}}{N_\mathrm{g}} + \frac{\sigma^2_{A_{\mathfrak{h}+1,n}}}{N_\mathrm{g}} \right)^{\frac{1}{2}} \\
&= \left[\frac{1}{N_\mathrm{g}} \left(\sigma^2_{A_{\mathfrak{h}}} + \sigma^2_{A_{\mathfrak{h}+1,n}} \right) \right]^{\frac{1}{2}} \\
&\overset{Eq.3.71}{=} \left[\frac{1}{N_\mathrm{g}-1} \left(N_\mathrm{g} \cdot q_{\mathfrak{h}} - s^2_{\mathfrak{h}} \right) + \frac{1}{N_\mathrm{g}-1} \left(N_\mathrm{g} \cdot q_{\mathfrak{h}+1} - s^2_{\mathfrak{h}+1} \right) \right]^{\frac{1}{2}} \\
&= \left[\frac{1}{N_\mathrm{g}-1} \left(N_\mathrm{g} \cdot q_{\mathfrak{h}} - s^2_{\mathfrak{h}} + N_\mathrm{g} \cdot q_{\mathfrak{h}+1} - s^2_{\mathfrak{h}+1} \right) \right]^{\frac{1}{2}} \\
&= \left\{ \frac{1}{N_\mathrm{g}-1} \left[N_\mathrm{g}(q_{\mathfrak{h}} + q_{\mathfrak{h}+1}) - \left(s^2_{\mathfrak{h}} + s^2_{\mathfrak{h}+1} \right) \right] \right\}^{\frac{1}{2}} \\
&= \left\{ \frac{1}{N_\mathrm{g}-1} \left[N_\mathrm{g}(q_{\mathfrak{h}} + q_{\mathfrak{h}+1}) - \left(s^2_{\mathfrak{h}} + s^2_{\mathfrak{h}+1} - 2s_{\mathfrak{h}}s_{\mathfrak{h}+1} + 2s_{\mathfrak{h}}s_{\mathfrak{h}+1} \right) \right] \right\}^{\frac{1}{2}} \\
&= \left\{ \frac{1}{N_\mathrm{g}-1} \left[N_\mathrm{g}(q_{\mathfrak{h}} + q_{\mathfrak{h}+1}) - \left((s_{\mathfrak{h}} + s_{\mathfrak{h}+1})^2 - 2s_{\mathfrak{h}}s_{\mathfrak{h}+1} \right) \right] \right\}^{\frac{1}{2}} \\
&= \left\{ \frac{1}{N_\mathrm{g}-1} \left[N_\mathrm{g}(q_{\mathfrak{h}} + q_{\mathfrak{h}+1}) + 2s_{\mathfrak{h}}s_{\mathfrak{h}+1} - (s_{\mathfrak{h}} + s_{\mathfrak{h}+1})^2 \right] \right\}^{\frac{1}{2}} \\
&= \left\{ \frac{1}{N_\mathrm{g}-1} \left[N_\mathrm{g} \left(q_{\mathfrak{h}} + q_{\mathfrak{h}+1} + \frac{2}{N_\mathrm{g}} s_{\mathfrak{h}}s_{\mathfrak{h}+1} \right) - (s_{\mathfrak{h}} + s_{\mathfrak{h}+1})^2 \right] \right\}^{\frac{1}{2}}
\end{aligned} \tag{3.73}$$

with the definitions

$$q_{\mathfrak{h},\mathfrak{h}+1} \equiv q_{\mathfrak{h}} + q_{\mathfrak{h}+1} + \frac{2}{m} s_{\mathfrak{h}}s_{\mathfrak{h}+1}, \tag{3.74}$$

$$s_{\mathfrak{h},\mathfrak{h}+1} \equiv s_{\mathfrak{h}} + s_{\mathfrak{h}+1} = \sum_{n=1}^{N_\mathrm{g}} a_{\mathfrak{h},n} + \sum_{n=1}^{N_\mathrm{g}} a_{\mathfrak{h}+1,n} \tag{3.75}$$

and

$$M_{\mathfrak{h},\mathfrak{h}+1} \equiv M_{\mathfrak{h}+(\mathfrak{h}+1)} \tag{3.76}$$

leading to

$$\sqrt{\mathrm{Var}(M_{\mathfrak{h},\mathfrak{h}+1})} = \left\{ \frac{1}{N_\mathrm{g}-1} \left[N_\mathrm{g} \cdot q_{\mathfrak{h},\mathfrak{h}+1} - s^2_{\mathfrak{h},\mathfrak{h}+1} \right] \right\}^{\frac{1}{2}} \tag{3.77}$$

which has the same structure as Eq. 3.71 but for sequential time periods.

The standard error in ARTM is then estimated by the relative standard deviation of the mean as

$$\begin{aligned}\frac{\sqrt{\mathrm{Var}(M_{\mathfrak{h},\mathfrak{h}+1})}}{M_{\mathfrak{h},\mathfrak{h}+1}} &= \sqrt{\frac{\sigma^2_{A_{\mathfrak{h},\mathfrak{h}+1,n}}}{N_\mathrm{g}\cdot M^2_{\mathfrak{h},\mathfrak{h}+1}}} \overset{Eq.3.70}{=} \sqrt{\frac{\sigma^2_{A_{\mathfrak{h},\mathfrak{h}+1}}}{N_\mathrm{g}\cdot s^2_{\mathfrak{h},\mathfrak{h}+1}}} \\ &\overset{Eq.3.77}{=} \sqrt{\frac{\frac{1}{N_\mathrm{g}-1}\left[N_\mathrm{g}\cdot q_{\mathfrak{h},\mathfrak{h}+1} - s^2_{\mathfrak{h},\mathfrak{h}+1}\right]}{s^2_{\mathfrak{h},\mathfrak{h}+1}}} \\ &= \sqrt{\frac{1}{N_\mathrm{g}-1}\left[N_\mathrm{g}\cdot\frac{q_{\mathfrak{h},\mathfrak{h}+1}}{s^2_{\mathfrak{h},\mathfrak{h}+1}} - 1\right]}\end{aligned} \tag{3.78}$$

(Janicke 2022a; Janicke 2022b; Janicke Consulting 2022).

For long simulation periods $H = \mathfrak{h} + (\mathfrak{h}+1) + (\mathfrak{h}+2) + \ldots$, ARTM uses Eq. 3.75 and 3.74 iteratively to estimate the relative standard deviation of the mean activity as

$$\sqrt{\frac{\mathrm{Var}(A_{H,n})}{s^2_H N_\mathrm{g}}} = \sqrt{\left(N_\mathrm{g}\frac{q_H}{s^2_H} - 1\right)\frac{1}{N_\mathrm{g}-1}}. \tag{3.79}$$

By default, ARTM uses $N_\mathrm{g} = 9$ sub-sets (GRS 2015).

This sample error depends on the number of numerical particles and decreases with increasing particle number. It can be seen as a figure-of-merit whether the number of numerical particles used in the simulation is large enough to obtain statistically reliable simulation results for the individual grid cells.

Chapter 4

The influence of input parameters and turbulence models

This chapter describes the evaluation of the ARTM model. In a first part it gives a description and the results of the sensitivity study of ARTM. This is followed by a description of five turbulence models (three are already part of ARTM while two are newly implemented) as well as the description and the results of the study of their vertical mixing properties.

Parts of this chapter are published in Hanfland et al. (2022) and Hanfland et al. (2023). Significant parts of the section 4.1 (first paragraph of Subsec. 4.1.1, parts of Subsec. 4.1.2 and first paragraph of Subsec. 4.1.3) are published in Hanfland et al. (2022) and are cited here. Major parts of Section 4.1 (second and third paragraph of Subsec. 4.1.1, parts of Subsec. 4.1.2 and second paragraph of Subsec. 4.1.3) are published in Hanfland et al. (2023) and cited here. Major parts of Section 4.2 (Subsec. 4.2.1, 4.2.2 and 4.2.3) are published in Hanfland et al. (2023) and are cited here. For the sake of readability there will be no further citations at the mentioned text parts in this chapter.

4.1 Dependence of simulation results on input parameters

It is important to understand how a model responds to variations of the input parameters. SA is a common tool to study such dependencies in a systematic way, it is crucial for model validation and can serve to guide future research (Hamby 1994; Frey et al. 2002; Saltelli et al. 2008). Furthermore, it can answer the following questions: how does the uncertainty of input parameters influence the model output; which parameters require additional research in order to reduce output uncertainty; which parameters are most significant or insignificant to the model's

output; does the model behave as expected when varying a certain input parameter (Hamby 1994; Rao 2005; Hanfland et al. 2023).

4.1.1 Methods for the quantification of sensitivity

SA methods are classified as either local or global depending on the sampled input parameter space (Saltelli et al. 2008; Morio 2011; Zagayevskiy et al. 2015). Local SA samples only a small region of the input parameter space using distinct locations. This results in a small number of simulation runs and thus little computing time. In contrast, global SA samples the entire input parameter space, which results in a larger number of simulations and also larger computing time. The smaller number of simulations of local SA allows the analysis of the simulation results in a descriptive way. In this work, this analysis is called qualitative SA. The large amount of simulations of the global SA makes the descriptive analysis of simulation results inconvenient or even impossible. In order to simplify the analysis and to quantify the influence of input parameters on the simulation output, sensitivity coefficient based methods have been developed. They condense the information of sensitivity to one quantity, the sensitivity coefficient. Such methods are available for local and global SA (Saltelli et al. 2008; Morio 2011; Zagayevskiy et al. 2015). The coefficient-based analysis is called quantitative SA in the following.

The results of the quantitative SA of the two classes as well as of two methods of the same class may differ depending on the shape of the input parameter space. Thus, the application of several different methods is necessary (Iman et al. 1988; Hamby 1995). Therefore, a qualitative evaluation of local SA as well as several different quantitative local and global SA methods are applied in this work in order to provide a more comprehensive assessment of the response of ARTM 2.8.0 to different input parameters.

Evaluation methods for qualitative sensitivity analysis

In order to objectively evaluate the results of the qualitative SA some target quantities are used. For instance, the spread of the exhaust plume is described with the normalised volume covered by the pollutant. The normalisation can be done either by normalising the volume covered by the plume in one horizontal simulation level with the entire volume of that specific level or by normalising the volume covered by the whole plume in the simulation domain with the volume of the entire simulation domain. Furthermore, the mean plume volume of the three lowest simulation levels is determined to get information about the spread close to the ground.

A second target quantity is the distance between the source and the position of maximum activity concentration (PMAC) in x-direction $x_{\max}$ in each horizontal level. To compare the influence of the input parameters on the concentration dis-

tribution close to the ground, the slope of the maximum concentration distribution given by

$$m_{\text{slope}} = \frac{h_{\text{s}} - h_{\text{l}}}{x_{\max}} \tag{4.1}$$

is calculated, where h_{s} is the source height and h_{l} is the level height. These slopes are only used for comparison when the investigated levels are below the source level.

For the analysis of the activity deposition rate, the surface area of the simulation domain is divided into rings formed by concentric circles around the source. The distance between the circumferences is 1 km (see Fig. 4.1 on page 58). The deposition rate is evaluated in each ring, respectively. Additionally, the total amount of deposited activity is evaluated.

Local coefficient-based sensitivity analysis methods

A local sensitivity analysis is performed at one point in the input parameter space which typically correspond to the default or reference inputs (Borgonovo et al. 2016). The output of a model is represented by $Y = g(X_1, \dots X_k)$ where the random variables X_i with $i = 1, \dots, k$ denote the different input parameters. The representations (or values) of X_i are denoted with x_i. The input parameters X_i are varied one at a time while all the others are held constant at their reference values x_i^{ref}. This local SA approach is similar to estimating the partial derivative $\frac{\partial Y}{\partial X_i}$ and characterises the effect of the input parameter X_i on Y at the reference point $\boldsymbol{X}^{\text{ref}} = (x_1^{\text{ref}}, \dots, x_k^{\text{ref}})$ (Morio 2011).

Sensitivity index The sensitivity index described by Hoffman et al. (1983) uses the default parameter set (reference point) where each parameter is varied one at a time by their full range, respectively. For continuous input parameters, several discrete values have to be pitched in order to limit the number of model evaluations. The sensitivity index is calculated as

$$SI_i = \frac{Y_{i,\max} - Y_{i,\min}}{Y_{i,\max}} \tag{4.2}$$

where $Y_{i,\max(\min)}$ indicates the maximum (minimum) output value, respectively. The sensitivity index is a value between $0 \leq SI_i \leq 1$ and gives the fraction of output variation caused by the varied input parameter (Hamby 1994).

One-at-a-time sensitivity measure The one-at-a-time sensitivity measure calculates the variation of the model output normalised to the largest output variation $\Delta Y_{\max}$ that had been observed for the different input parameters. Starting

from the reference parameter set, the parameters are varied one at a time by a percentage α. The resulting model outputs $Y_{i,\pm\alpha} = g(X_1, \ldots, X_i \cdot (1 \pm \alpha), \ldots, X_k)$ are then used to calculate the sensitivity coefficient for the input parameter X_i as

$$SM_i^{\alpha} = \frac{|Y_{i,+\alpha} - Y_{i,-\alpha}|}{\Delta Y_{\max}} \tag{4.3}$$

where $\Delta Y_{\max} = \max(|Y_{l,+\alpha} - Y_{l,-\alpha}|)\ \forall l \in i$ (Link et al. 2018). In this work the percentages $\pm 25\,\%$ and $\pm 50\,\%$ are used for α. SM_i^{α} is a value between $0 \leq SM_i^{\alpha} \leq 1$ where unity identifies the input parameter with the biggest effect on the model output Y.

Global coefficient-based sensitivity analysis methods

Global SAs sample the whole input parameter space, which leads to a broader representation of the sensitivity compared to local methods but also increase computation time. A general discussion about global SA can be found in Saltelli et al. (2008).

Sobol' indices The variance-based Sobol' indices use variance decomposition to calculate indices of different orders (Sobol' 1993). Usually only two key Sobol' indices are determined: the first-order index S_i; and the total effect index $S_{\mathrm{T}i}$.

For the first one, the conditional expected value of the model output $E_{\boldsymbol{X}_{\sim i}}(Y|X_i)$ with a constant value of X_i and varying values for all other input parameters $\boldsymbol{X}_{\sim i}$ is computed. For different realisations of X_i, $V_{X_i}[E_{\boldsymbol{X}_{\sim i}}(Y|X_i)]$ reflects the variance of the model output Y originating from a variation of the input parameter X_i. The first Sobol' index is then given by

$$S_i = \frac{V_{X_i}[E_{\boldsymbol{X}_{\sim i}}(Y|X_i)]}{V(Y)} \tag{4.4}$$

where $V(Y)$ is the unconditional variance of the output where all X_i are varied. $V_{X_i}[E_{\boldsymbol{X}_{\sim i}}(Y|X_i)]$ cannot be larger than $V(Y)$ and thus for the sensitivity coefficient $0 \leq S_i \leq 1$ is valid. This index is the first-order sensitivity index and does not take higher-order effects (i.e. interactions between different input parameters) into account (Saltelli et al. 2008).

The second index considered here is the total effect index. It takes higher order terms into account, which might be important depending on the model. The total effect is calculated as

$$S_{\mathrm{T}i} = 1 - \frac{V_{\boldsymbol{X}_{\sim i}}[E_{X_i}(Y|\boldsymbol{X}_{\sim i})]}{V(Y)} \tag{4.5}$$

where $V_{\boldsymbol{X}_{\sim i}}[E_{X_i}(Y|\boldsymbol{X}_{\sim i})] = V_{\boldsymbol{X}_{\sim i}}[E_{X_i}(Y|X_1, X_2, \ldots, X_{i-1}, X_{i+1}, \ldots, X_k)] \leq V(Y)$ is the total variance of all input parameters except X_i. As the first order index, this

total effect index is a value between zero and unity where a value of zero indicates no influence of X_i on the output Y while unity indicates a strong influence (Saltelli et al. 2008). A comprehensive description of the method is given by Saltelli et al. (2008).

For the analysis presented here, the python library SALib (Herman et al. 2017) is used for the quasi-random sampling with low discrepancy after Joe et al. (2008) of the input parameter space as well as for the calculation of the Sobol' indices. It furthermore allows the estimation of the 95 % confidence intervals (Herman et al. 2023).

δ-method In comparison with the Sobol' indices, the δ-method takes the complete density distribution of the model output into account, which ensures the conservation of the whole information of the output density distribution (Borgonovo 2007). The probability density function (PDF) of X_i is denoted $f_{X_i}(x_i)$. The sensitivity coefficient δ_i for the input parameter X_i is calculated using the marginal density distribution of the input parameter $f_{X_i}(x_i)$ and the difference between the unconditional density function $f_Y(y)$ and the conditional density distribution function $f_{Y|X_i}(y)$ of the model output with fixed representation $X_i = x_i$ as

$$\delta_i = \frac{1}{2} \int f_{X_i}(x_i) \left[\int |f_Y(y) - f_{Y|X_i}(y)| \, \mathrm{d}y \right] \, \mathrm{d}x_i \tag{4.6}$$

(Borgonovo 2007). δ_i represents the total effect of an input parameter X_i on Y. It can take a value between zero and unity ($0 \leq \delta_i \leq 1$) where zero means that the output is independent of X_i (Plischke et al. 2013). The same library SALib (Herman et al. 2017) was used to apply the δ-method including the estimation of the 95 % confidence interval.

4.1.2 Simulation setup for the sensitivity analyses

In order to analyse the sensitivity of model results on the different input parameters, simulations of gaseous and particle-bound radioactive tracers are performed. A single point source (at $x = 25\,\mathrm{m}$, $y = 25\,\mathrm{m}$) with varying vertical position close to the left border of a rectangular simulation domain extending 10 km from west to east and 1 500 m from south to north was used (see Fig. 4.1). The vertical extension of the simulation domain is 1 500 m. The spatial resolution for both horizontal directions is 50 m. Vertically, the 1 500 m high simulation domain is divided into 19 levels of varying thickness gradually increasing from the lowest layer (3 m thick) to the top simulation layer (300 m thick). The thicknesses of the different levels are summarized in Tab. 4.1. In order to focus on the evolving dispersion pattern the topography is assumed as flat surface. A constant westerly wind (270°) was

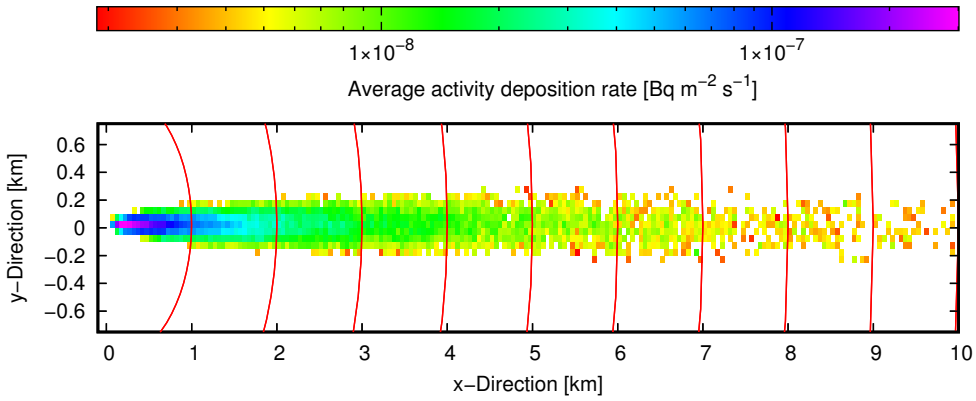

Figure 4.1: Simulation domain with the average activity deposition rate of PM1 in logarithmic scale. The red lines denote the concentric circles around the source dividing the ground surface into evaluation areas. The x-direction is in west-east orientation, the y-direction in north-south orientation. From Hanfland et al. (2022).

used for the entire simulation period of 24 hours with a velocity of $1\,\mathrm{m\,s^{-1}}$ in 10 m height.

As I want to focus on dispersion properties radionuclides with long half-life are used in this analysis. The krypton isotope ^{85}Kr with a decay constant of $\lambda_{\mathrm{decay}} = 2.05 \times 10^{-9}\,\mathrm{s^{-1}}$ was used as gaseous tracer. This results in a decay of less than 0.02 % within the simulation period. The emission source is represented as a source with a constant activity rate of $1\,\mathrm{Bq\,s^{-1}}$. Additional simulations are performed for PM, in which case the emitted activity rate stays unchanged but the emission only occurs in the first 20 hours of the day. Doing so, all emitted particles are able to leave the simulation domain within 24 hours which ensures the investigation of the fraction of particles being deposited relative to the emitted ones. For the emission of PM, ^{137}Cs with the decay constant $\lambda_{\mathrm{decay}} = 7.32 \cdot 10^{-10}\,\mathrm{s^{-1}}$ is used. The decay ratio is less then 0.006 % within 24 hours. Therefore, the radioactive decay of both radionuclides has no significant effect on the simulation results in this analysis and can therefore be neglected. Plume rise and wind direction rotation due to the Ekman-spiral is not taken into account. Figure 4.1 illustrates the simulation domain with evaluation areas confined by the concentric circles and the average deposition rate.

The input parameters stability class SC, roughness length z_0, zero-plane displacement factor d, source height h_{s} and tracer type which is either a tracer in the gas phase or PM with four different size classes representing different aerodynamic diameters d_{aero} are assumed to be the key parameters of ARTM. The zero-plane displacement d_0 depends on d as $d_0 = d \cdot z_0$. When using d instead of d_0 the input parameters for the SA are independent. This allows the analysis of the unbiased effects of input parameter variations. Wind direction and wind speed have a strong

Table 4.1: Default setup of the horizontal levels in ARTM. The height of the lower boundaries of the level agl and the level thickness are given in meter. After Richter et al. (2015b) from Hanfland et al. (2022).

level	lower boundary height [m]	thickness [m]
19	1 200	300
18	1 000	200
17	800	200
16	700	100
15	600	100
14	500	100
13	400	100
12	300	100
11	200	100
10	150	50
9	100	50
8	65	35
7	40	25
6	25	15
5	16	9
4	10	6
3	6	4
2	3	3
1	0	3

influence on the dispersion of tracers, too. However, the stochastic character of wind direction and wind speed time series that may strongly depend on the geographic location limit the meaningfulness of a general test case. Furthermore, the study of wet deposition, as a consequence of precipitation, suffers from similar highly variable influences such as precipitation duration, strength and local distribution. They are highly case dependent and I therefore exclude wind and precipitation from this general case study. The used parameters and their ranges are summarized in Tab. 4.2. Usually only a discrete set of six SCs is provided for the simulations according to German regulations. The number of z_0 values allowed by ARTM is also limited to nine roughness length classes (TA Luft 2002). For this analysis, the roughness lengths are further limited to the six largest class values. German authorities recommend a value of the zero-plane displacement

Table 4.2: Input parameters and their values and ranges. The default parameters for local SAs are marked with (*). For the global SAs the given values of the parameters marked with [1)] are sampled. Those marked with [2)] are sampled continuously within the range while those marked with [3)] are sampled with a resolution of 1 m within the range. For the coefficient based SAs the maximum source height was extended to 150 m and marked with [4)]. After Hanfland et al. (2022).

Parameter	Values/Range
Stability class (SC) [1)]	very stable, stable, neutral*, indifferent, unstable, very unstable
Roughness length (z_0) [1)]	0.10 m, 0.20 m, 0.50 m*, 1.00 m, 1.50 m, 2.00 m
Zero-plane displacement factor (d) [2)]	3 ... 6* ... 9 ... 15
Source height (h_s) [3)]	10 m ... 20 m* ... 120 m (150 m[4)])
Tracer type	Gas*, PM 1, PM 2, PM 3, PM 4

factor $d = 6$ (TA Luft 2002; VDI 3783 part 8 2017). The range for the variation of d is centred on this value and limited to forest canopy heights typical for mixed forest (Lang et al. 2022). The range for the source height is oriented to the stack heights of nuclear facilities in Germany. In Tab. 4.2 the parameter values for the reference point for the local SAs are marked with * symbol. For global sensitivity analyses, the whole parameter ranges are sampled, respectively. The tracer type is a fundamental tracer property. However, it is excluded from the quantitative (coefficient based) SA because the resulting deposition patterns are too complex to be described by single target quantities in a meaningful way.

The evaluation of the SAs is performed with respect to the target quantities of the simulation results, which were described in Sec. 4.1.1. Both methods, qualitative and quantitative SA, use

i) the plume volume,

which is a measure for the tracer dispersion and is closely linked to the maximum mixing ratio. Furthermore, the qualitative local SAs also use

ii) the distance between the source and the PMAC for each horizontal simulation level and

iii) the activity deposition rate of PM.

In contrast to this the quantitative SA using sensitivity coefficients uses

iv) the distance between the source position and the PMAC at ground level,

which is of special interest for radiation exposure assessment.

All the modelled concentration and deposition rate values are associated with a grid cell and the result of contributing numerical particles, respectively. Each numerical particle is subject to advection and the turbulent motion, which is random (see Secs. 3.2.1, 3.2.6 and 3.2.7). Thus, each concentration value or deposition rate is associated with a sample error (see Sec. 3.2.9). A high sample error of a grid cell indicates the concentration or deposition rate value to be rather uncertain. This is the case for the grid cells at the edge of the plume. For this analysis, the simulation results are limited to those concentration values and deposition rates having a maximum sample error of 30 % assuring a sufficient statistical significance of the result.

4.1.3 Evaluation of parameter sensitivity

Qualitative local sensitivity analysis

Volume of the exhaust plume The volume of the exhaust plume in the simulation domain - and for each level separately - gives insights into how the plume spreads in all three dimensions. The SCs have a strong impact on the plume volume as shown in Fig. 4.2 where the volume covered by the plume in each horizontal level is normalised by the level volume, respectively, for all the different SCs. It can be seen that the overall plume volume increases with decreasing atmospheric stability. The plume volume of the SC "very stable" (smallest plume spread) covers only 1 % of the volume of the entire simulation domain while the plume with the biggest spread ("very unstable") reaches 71 % (see Tab. 4.3). However, the normalized volume in the lowest three levels doesn't show a monotonic behaviour. For these levels, the largest mean plume volume is found for neutral boundary layer conditions (37.3 %) while the smallest mean plume volume of the lowest three levels is found for very unstable conditions (13.3 %) resulting in a variation of the mean plume volume of the lowest three levels of 24 %. For levels above the emission level (level 5) the volume increases with atmospheric instability. Especially the extent of the plume towards higher levels is clearly observable in Fig. 4.2. This vertical spread is not limited by the simulated mixing layer height as it is shown in Tab. 4.3. For neutral atmospheric conditions the mixing layer height is above the top level of the plume while for all other cases it is directly at the lower border of the top plume level (for indifferent stratification), within the top plume level ("stable" and "very stable") or below the lower border of the top plume level ("unstable" and "very unstable").

The roughness length has less influence on the plume volume with a minimum coverage of 7 % for $z_0 = 0.1$ m of the simulation domain and a maximum coverage of 24 % for $z_0 = 2.0$ m while keeping the other input parameters' reference values. In

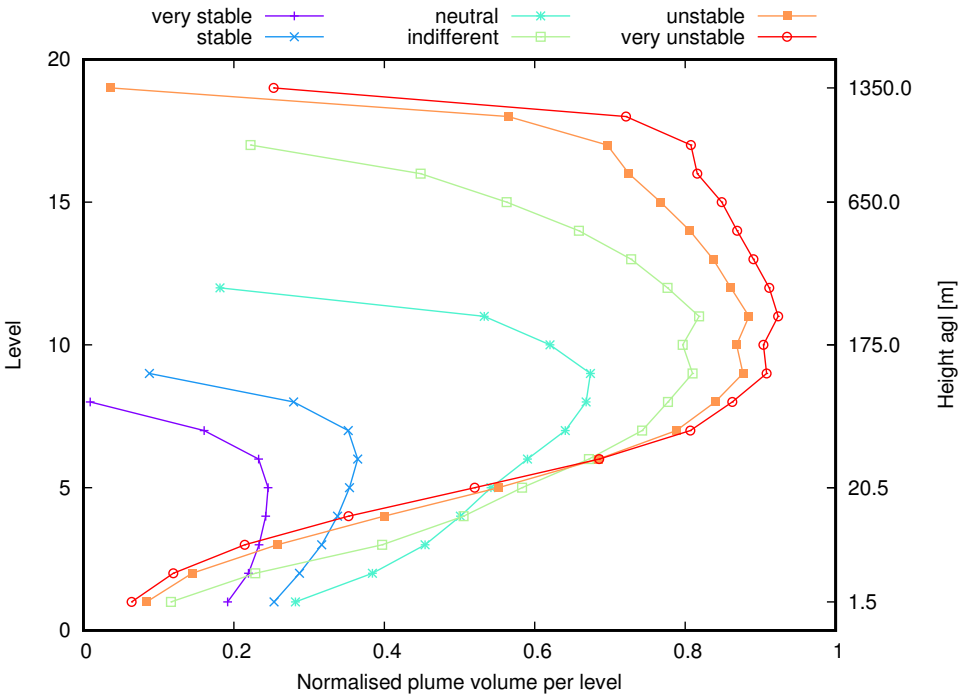

Figure 4.2: Normalised plume volume of the 19 horizontal levels for the SCs. The point source is located at 20 m agl (in level 5). From Hanfland et al. (2022).

Table 4.3: The plume volume relative to the volume of the simulation domain, the mixing layer height (VDI 3783 part 8 2002) and the upper and lower boarder of the top plume level for the different SCs. From Hanfland et al. (2022).

SC	plume volume	mixing layer height	top plume level
very unstable	71 %	1 100 m	1 200 – 1 500 m
unstable	61 %	1 100 m	1 200 – 1 500 m
indifferent	39 %	800 m	800 – 1 000 m
neutral (default)	13 %	418 m	300 – 400 m
stable	2 %	127 m	100 – 150 m
very stable	1 %	62 m	60 – 100 m

the lowest three simulation levels, only a very weak volume alternation (5.3 %) can be observed. No spread towards higher levels is observed, thus growth of the plume coverage from small to large values of z_0 occurs mainly in the mid levels of the plume. However, the influence of z_0 to the plume volume depends strongly on the SC. The maximum effect of z_0 on the volume is observed for neutral atmospheric conditions. For both, more stable and less stable conditions, the influence of the roughness length on the plume volume decreases.

The overall influence of the zero-plane displacement height $d_0 = d \cdot z_0$ on the plume volume is weaker than the influence caused by the roughness length. Nevertheless, the mean plume volume for the three lowest simulation levels show a different picture with a variation of 7 % by varying the zero-plane displacement factor as given in Tab. 4.2. This shows a stronger influence of d_0 on the lowest three simulation levels than z_0. The turbulence is determined by the Obukhov length and thus, the friction velocity u_* via SC and z_0 while d_0 predominantly influences the wind profile because it shifts the logarithmic wind profile vertically. There is no spread of the plume towards higher levels observed by varying the zero-plane displacement.

The overall volume of the plume is hardly affected by a variation of the source height in the given range. However, the source height strongly influences the particle spread in the lowest three levels. When varying the source height, the mean plume volume of the lowest three levels changes by 9.8 %. In agreement with the boundary layer model the diffusion coefficient close to the ground is smaller than at higher levels. Therefore, tracers do not spread well at levels close to the ground. A spread of the plume towards higher levels is expected to be proportional to the source height but was not observed because of the limited range of the source height variation compared to the simulation grid resolution in medium and high levels.

Distance from source to maximum concentration The turbulence in the atmosphere is not only a key to the plume extent but also influences the PMAC in each horizontal level of the plume. Figure 4.3 shows that the distance between the source and the PMAC decreases with increasing turbulence in the atmosphere. The information about the position of the maximum concentration is of special interest in the levels close to the ground where most organisms are living. For the lowest three levels average slopes for the PMAC from $-13.1\,\mathrm{m\ km^{-1}}$ to $-128.7\,\mathrm{m\ km^{-1}}$ for very stable and very unstable conditions were observed, respectively. This shows the very unstable atmosphere to be better mixed in the levels close to the ground despite of the surface effects (smaller diffusion coefficient close to the ground).

Compared to the SC a variation of the roughness length has a weaker influence on the distance between the source and the PMAC. This is observed in the middle

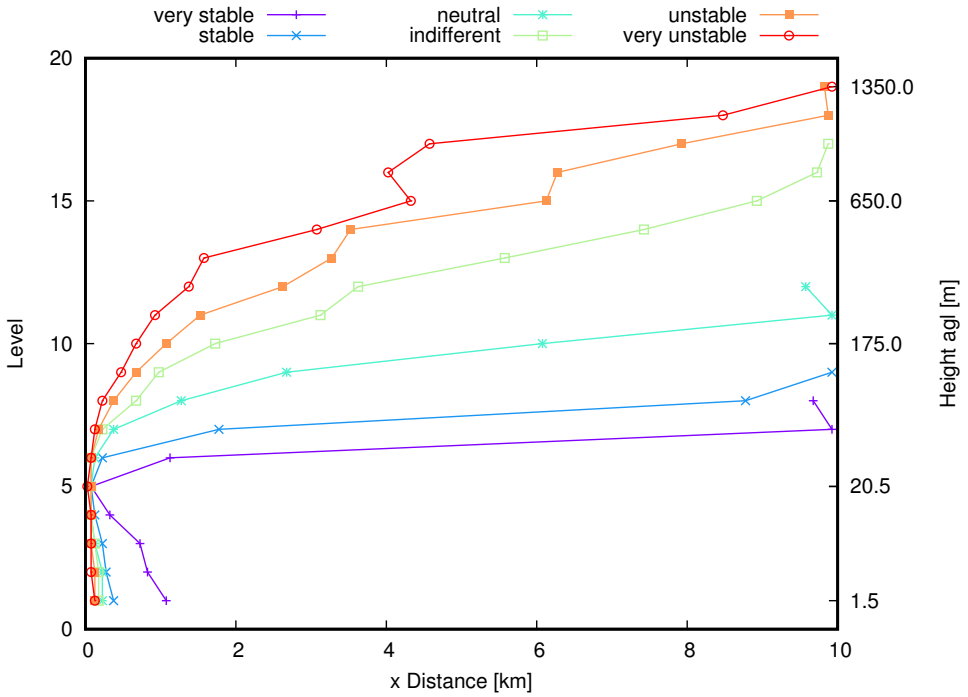

Figure 4.3: Position of the maximum concentration in each level for the six SCs. The point source is located at a height of 20 m agl (in level 5). From Hanfland et al. (2022).

and upper levels but also in the levels close to the ground. Here, the slopes of the three lowest levels are steeper compared to those for a variation of the SC and determined between $-39.5\,\mathrm{m\,km^{-1}}$ and $-153.3\,\mathrm{m\,km^{-1}}$. This indicates the PMAC to be closer to the source than it is the case for the variation of the SC. However, there is a strong dependence of the SC especially in the lowest levels. The influence of the roughness length increases for more stable conditions while it decreases for more unstable conditions.

The zero-plane displacement hardly affects the distance between source and the PMAC. In contrary, the height of the source has a strong influence on the maximum concentration. With a shift of the source to different heights agl the plume and thus the PMAC in each level shifts vertically as well.

Deposition of PM on the ground PM may deposit to the ground. Depending on the aerodynamic diameter the deposition rate changes as it can be seen in Fig. 4.4 for neutral conditions (reference setting) as well as for very stable and very unstable atmospheric conditions. For neutral conditions, deposition rates are larger for large particles resulting in a bigger amount of deposited material closer to the source. While for PM larger than 10 µm (size classes PM 3 and PM 4)

almost all particles are deposited, smaller particles can spread widely and can stay in the atmosphere for a long time. Values of the percentage of deposited activity, compared to the emitted one, are given in Tab. 4.4.

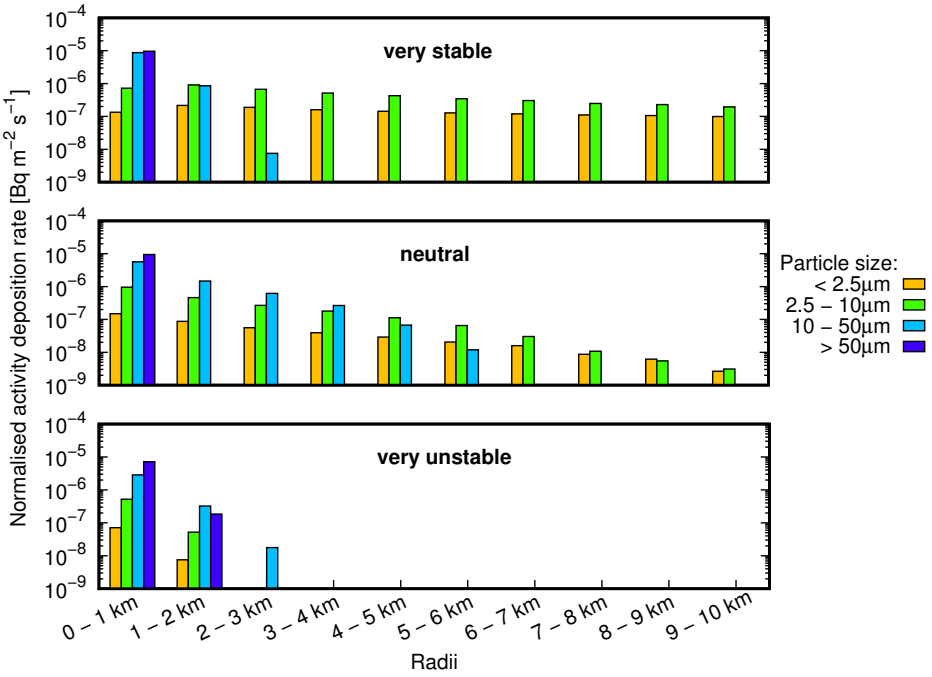

Figure 4.4: Normalised activity deposition rate at different distances from the source for the four different particulate matter size classes. The activity deposition rates are shown for very stable, neutral (default) and very unstable boundary layer conditions. From Hanfland et al. (2022).

The deposition rate is not only dependent on the aerodynamic diameter but also on the SC as seen in Fig. 4.4. In the case of very stable atmospheric conditions the deposition rate for PM smaller than 10 µm (size classes PM 1 and PM 2) decreases only slightly with increasing distance from the source while the larger particles are almost completely deposited after 3 km (99.46 % of particles of 10–50 µm and 99.93 % of particles $>$ 50 µm). With increasing turbulence in the atmosphere the overall deposition rate decreases. This leads to a wider spread of the larger particles at neutral atmospheric conditions and thus to less particles deposited to the ground at very unstable conditions. This is explained by the turbulence in the atmosphere cancelling out the sedimentation and keeps the particles in the atmosphere. This can also be seen in Tab. 4.4 where the amount of deposited activity shows the lowest values at very unstable conditions for all particle sizes and monotonically increase when the atmosphere becomes less turbulent.

Table 4.4: Fractions of deposited activity per SC and particle size class in the whole simulation domain. From Hanfland et al. (2022).

	Deposition [%]			
SC	PM 1	PM 2	PM 3	PM 4
very unstable	0.8	6.0	33.2	75.5
unstable	1.3	8.7	47.7	88.6
indifferent	2.0	12.2	61.8	94.5
neutral (reference)	4.3	21.8	83.8	98.4
stable	9.8	40.7	97.3	99.7
very stable	14.6	47.3	99, 5	99.9

Sensitivity coefficient-based analysis

All input parameters mentioned in Sec. 4.1.3 were analysed with the quantitative (coefficient based) SA methods. The results of the calculations of the local and global sensitivity coefficients are summarised in Tab. 4.5. Concerning the plume volume, all SA methods result in the highest SA coefficients for the SC. Although less prominent, this is also observable for the distance between source and the PMAC at the ground level except for sensitivity indices SI_i.

For $SM_{z_0}^{25}$ no value can be calculated because a variation of $\pm 25\,\%$ from the reference roughness length value does not lead to a change of the categorial z_0 value. Nevertheless, the two different ranges of variation ($\alpha = 25$ and $\alpha = 50$) for SM_i^{α} can give additional information about the sensitivity of target quantities on parameters. It can be seen from Tab. 4.5 that the deviations between the coefficients of SM_i^{25} and SM_i^{50} are small for the plume volume while they are large for the distance between the source and the maximum concentration. The influence of the input parameters seem to be rather linear for the plume volume while it is clearly not linear for the distance between source and the PMAC at the ground.

For the global SA methods, both target quantities show a distinct importance not only of the first order (direct influence of one single input parameter) but also of higher order (includes interactions of two or more input parameters) effects. A small difference between S_i and $S_{\mathrm{T}i}$ shows a large first order effect as it can be seen for the plume volume. In contrary to this, a large difference reveals a small first order effect compared to a higher order effect as it can be seen for the distance between source and the PMAC at ground level. This is in agreement with the conclusions that can be drawn from the δ_i coefficients. The sum of the sensitivity coefficients for the plume volume $\sum_i \delta_i = 1.05 \pm 0.01 \cong 1$ indicates that the effects of variation in the input parameters on variation in the plume volume

Table 4.5: Sensitivity coefficients of local and global SAs for the plume volume and for the distance between the source and the PMAC at the ground level. For the Sobol' indices (S_i and $S_{\mathrm{T}i}$) and the δ-method (δ_i) 95 % confidence intervals are given as well. Coefficients with very large relative confidence intervals are marked with (*), coefficients of the same method that cannot be distinguished within their confidence intervals are marked with (†). From Hanfland et al. (2023).

	Plume volume					
Parameter	SI_i	SM_i^{25}	SM_i^{50}	S_i	$S_{\mathrm{T}i}$	δ_i
SC	0.987	1	1	0.981 ± 0.032	0.99 ± 0.04	0.666 ± 0.009
z_0	0.718	-	0.202	$0.005 \pm 0.006^*$	0.017 ± 0.002	0.130 ± 0.001
d	0.291	0.022	0.027	$(0.3 \pm 8) \cdot 10^{-4*}$	$(28 \pm 5) \cdot 10^{-5}$	$0.126 \pm 0.002^\dagger$
h_s	0.130	0.004	0.004	$(0.9 \pm 9) \cdot 10^{-4*}$	$(39.5 \pm 2.3) \cdot 10^{-5}$	$0.126 \pm 0.002^\dagger$
	Distance between source and PMAC at the ground level					
Parameter	SI_i	SM_i^{25}	SM_i^{50}	S_i	$S_{\mathrm{T}i}$	δ_i
SC	0.884	1	1	0.16 ± 0.06	0.90 ± 0.06	0.328 ± 0.005
z_0	0.769	-	0.158	$0.00 \pm 0.04^*$	$0.75 \pm 0.07^\dagger$	$0.118 \pm 0.003^\dagger$
d	0.222	0.250	0.053	$0.00 \pm 0.01^*$	0.06 ± 0.02	$0.115 \pm 0.003^\dagger$
h_s	0.971	0.750	0.211	$0.02 \pm 0.04^*$	$0.74 \pm 0.07^\dagger$	0.129 ± 0.004

are separable, i.e. interactions between input parameters play a minor role. For the distance between source and the PMAC, the sum of the sensitivity coefficients $\sum_i \delta_i = 0.690 \pm 0.008 \ncong 1$ indicates the important role of cross interactions between the input parameters (Borgonovo 2007). In contrary to the findings of the Sobol' indices that some input parameters having negligible influences, the δ-method states the output characteristics to be sensitive to all parameters.

Some of the global SA coefficients have very large relative confidence intervals and cannot be distinguished from zero (marked with *). Some cannot be distinguished from others of the same method within their confidence intervals (marked with †). Increasing the sample size of 24 576 further would be necessary to get smaller confidence intervals but this would also increase the computation time (Herman et al. 2023).

Based on the coefficients from Tab. 4.5 the input parameters were ranked according to their importance as summarised in Tab. 4.6. The rankings obtained for the individual SA methods differ not only for the two target quantities but also between different methods. The overall ranking, which is simply computed as the sum (Σ) over the different methods, is provided in the last column.

Table 4.6: Ranking of the influence of the input parameters on the plume volume and on the distance between the source and the PMAC at ground level for local and global sensitivity analyses methods. From Hanfland et al. (2023).

	Plume volume							
Parameter	SI_i	SM_i^{25}	SM_i^{50}	S_i	$S_{\mathrm{T}i}$	δ_i	Σ	Rank
SC	1	1	1	1	1	1	6	1
z_0	2	3	2	3	2	2	14	2
d	3	2	3	3	4	3.5	18.5	3
h_s	4	4	4	3	3	3.5	21.5	4
	Distance between source and PMAC at the ground level							
Parameter	SI_i	SM_i^{25}	SM_i^{50}	S_i	$S_{\mathrm{T}i}$	δ_i	Σ	Rank
SC	2	1	1	1	1	1	7	1
z_0	3	3	3	3	2.5	3.5	18	3
d	4	4	4	3	4	3.5	22.5	4
h_s	1	2	2	3	2.5	2	12.5	2

The most unambiguous result is that all SA methods show the plume volume to be most sensitive to the SC. The ranks for the other input parameters, in contrast, vary. The ranking of SM_i^{25} given in Tab. 4.6 is the average of all possible rankings

for this method when taking into account that there is no coefficient for $SM_{z_0}^{25}$. The rankings of the remaining local SA methods SI_i and SM_i^{50} are in agreement with each other for the plume volume, while the rankings of the global SA methods disagree. Compared to the rankings for the plume volume, those for the distance between source and PMAC at the ground level is less uniform.

For both target quantities, the resulting rankings given in column "Rank" in Tab. 4.6 differ from each other. This emphasises that different target quantities are not necessarily sensitive to the same input parameters. The simulation result is highly sensitive to the SC and thus it is a potential source of high uncertainty. The source height h_s has little influence on the plume volume but it is the second most important parameter for the distance between source and PMAC at the ground level.

Scatter plot analysis of parameter influence

The simulations of the global SA can be used to illustrate the target quantities

i) plume volume and

iv) distance between source and PMAC at the ground level

dependent of the four input parameters in scatter plots. These can be used to investigate the behaviour of the model (Saltelli et al. 2008). Figure 4.5 shows the plume volume above the four input parameters, respectively. For all input parameters there are gaps between bands of normalised plume volume above 0.25 present. The gaps are the result of the six distinct SCs used in ARTM. In Fig. 4.5, the distinct bands for the SCs "indifferent", "unstable" and "very unstable" are shown. In contrast to this, the bands for "very stable", "stable" and "neutral" overlap each other. In Fig. 4.5 b, the plume volumes originating from neutral conditions can be separated from the more stable ones for the different z_0 revealing a further gap. For the other input parameters analysed in this study such an effect of causing gaps in the plume volume distribution was not observed. It suggests that the classification of the atmospheric stability is to coarse.

A SA using scatter plots is hardly possible for ARTM because of the complex and non-linear dependency of the plume volume. However, it can be seen that a variation of the SC has a strong influence on the plume volume especially for rather unstable SCs. Other parameters affecting the plume volume cannot be identified from Fig. 4.5.

Scatter plots for the distance between source and PMAC at the ground level and the input parameters are shown in Fig. 4.6. Here, no bands or gaps are observed for the distance between source and PMAC. In Fig. 4.6 no influence of the input parameters on the target quantity is recognised if z_0 or d were varied.

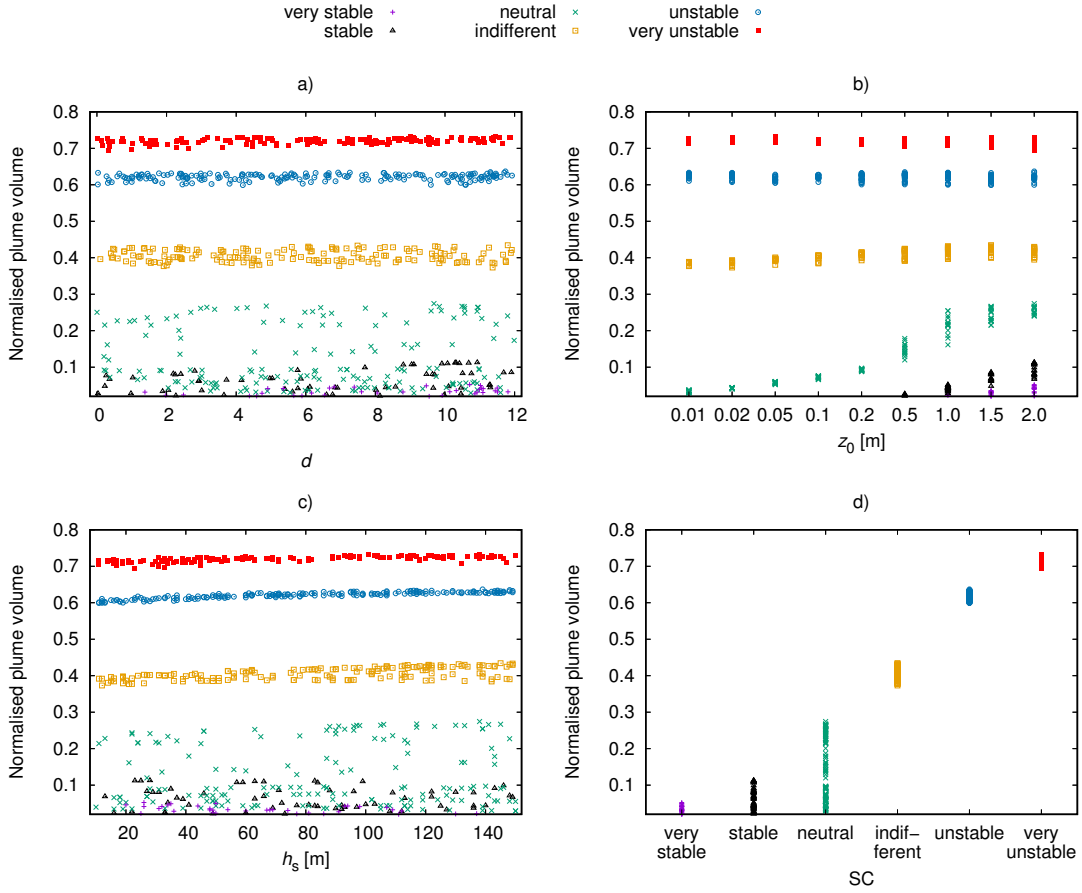

Figure 4.5: Scatter plots of the normalised plume volume versus the input parameters d, z_0, h_s and SC, colour coded according to the SCs. Data of the first 1 000 samples of the global SA is used.

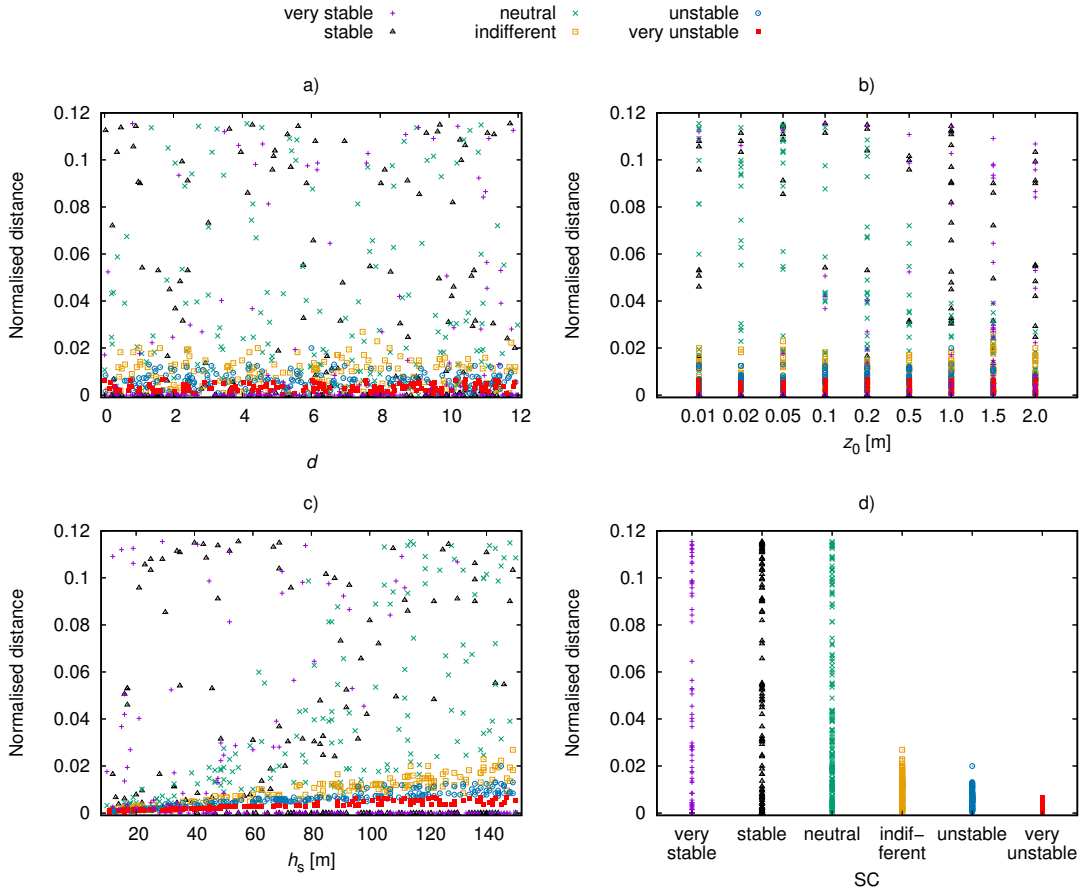

Figure 4.6: Scatter plots of the distance between the source and the PMAC at the ground level versus the input parameters d, z_0, h_s and SC colour coded according to SCs. The distance is normalised with 86.4 km (distance that a particle with a velocity of $1\,\mathrm{m\,s^{-1}}$ can do within 24 hours). Data of the first 1 000 samples of the global SA is used.

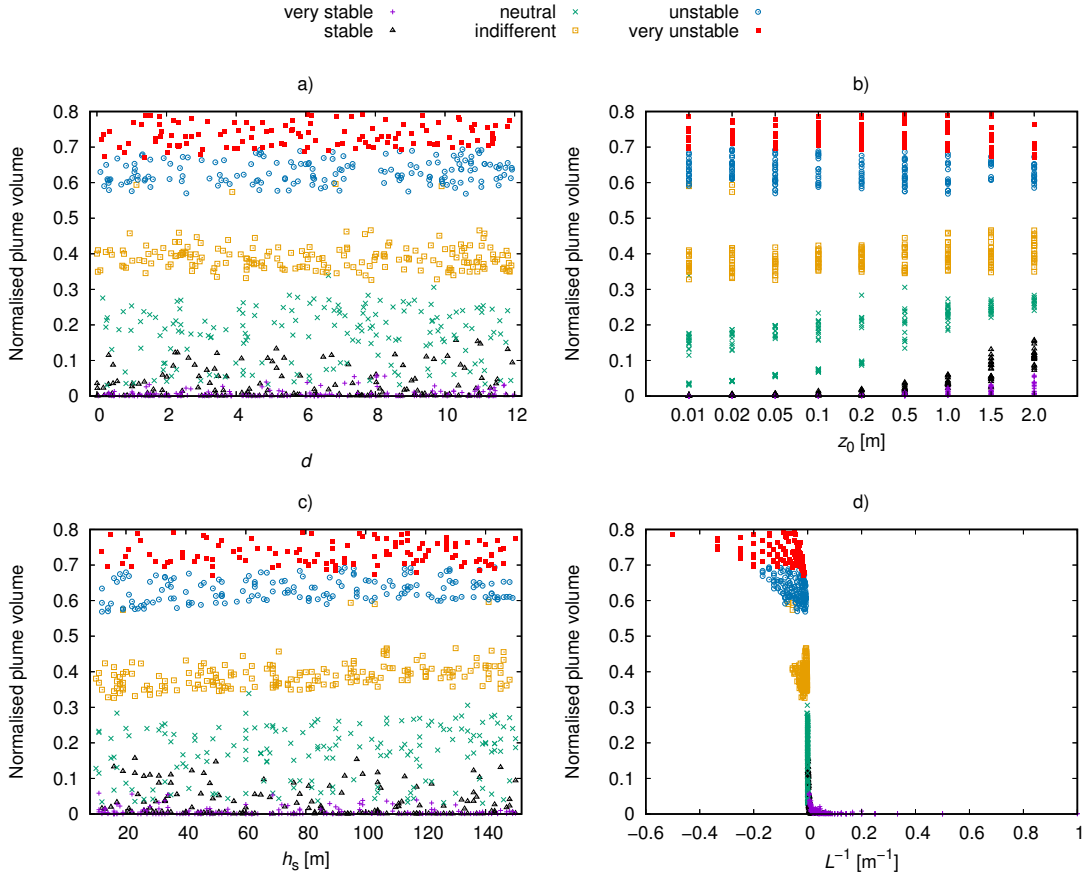

Figure 4.7: Scatter plots of the normalised plume volume versus the input parameters d, z_0, h_s and L^{-1} colour coded according to SCs. The Obukhov length L is sampled with a sample size of 1 000.

h_s and the SC have an effect on the normalised distance, respectively. Although a variation of the SC from "very stable" to "neutral" and from "indifferent" to "very unstable" has no distinguishable effect a variation from "neutral" to "indifferent" can lead to a large difference in the normalised distance between source and PMAC at the ground. This graphical SA suggest SC mostly affects the plume volume and the distance between source and PMAC at the ground level and are in agreement with the findings of the previous analyses.

The rather coarse classification of the atmospheric stability into six stability classes limits the possible plume volumes (see Fig. 4.5). The usage of a finer classification such as the Obukhov length partly overcomes this shortcoming and lead to a more homogeneous plume volume distribution as shown in Fig. 4.7. The remaining gaps might be caused by the wide range of the Obukhov length ($-\infty$ to $+\infty$) that cannot be sampled sufficient with 1 000 samples. A larger

number of samples or the sampling of the reciprocal Obukhov length could close the remaining gaps. However, further analyses of the plume volume are necessary to reveal the cause of the remaining gaps in Fig. 4.7.

4.2 The mixing properties of turbulence models under unstable conditions

Many LPDMs use a Markov process in the form of a Langevin equation to model the stochastic turbulent movement of tracers in the atmosphere. This Markov process is often parametrised by wind speed fluctuations and Lagrangian correlation time scales and called as turbulence model (TM) (Lin et al. 2013). Models containing such a Markov process do not necessarily preserve a well-mixed atmosphere with time as it is expected by the second law of thermodynamics. This means that during atmospheric dispersion simulations initially uniformly distributed tracers in an incompressible flow can be accumulated or diluted in some regions of the simulation domain. This would violate the second law of thermodynamics. Exactly fulfilling this criterion is challenging, but it is important to quantify the degree of deviation from this ideal behaviour to judge the magnitude of systematic model biases and whether these biases are acceptable (Thomson 1987; Lin et al. 2013; Bahlali et al. 2020; Katharopoulos et al. 2022; Hanfland et al. 2023). The description of the TMs, the used model setup for the analysis and the evaluation of the results contained in this section are published in Hanfland et al. (2023) and may be cited word-by-word.

4.2.1 Description of the turbulence models

The TM implemented in ARTM 2.8.0 as its default model is well known in Germany. It has been reported by Janicke et al. (2011) that it sometimes underestimates plume dispersion. Therefore, they introduced a modified TM leading to more effective dispersion, which can optionally be used in ARTM. In 2022, the new version 3.0.0 of ARTM was released. It implements a further TM according to the guideline VDI 3783 part 8 (2017). All three models deviate from the model suggested by Hanna (1982), which is quite widely used and thoroughly tested against tracer release experiments. However, in contrast to other models the turbulence may abruptly change between SCs. To overcome this issue of discontinuity, Degrazia et al. (2000) proposed a continuous description of the turbulence throughout all atmospheric conditions that approximates the model of Hanna under certain conditions. Since the used measurement data set for the comparison of simulations and observations was collected under unstable atmospheric conditions the following analyses focus on unstable stratification. The wind speed fluctuations

σ and the Lagrangian correlation time scales T_L of the five TMs are presented in the following Eqs. 4.7 - 4.27 for unstable stratification and their profiles are displayed in Fig. 4.8. For the following quantities I define the x-components along the average horizontal wind direction, the y-components perpendicular to it in the horizontal plane and the z-components in the vertical direction. Although the zero-plane displacement is used in ARTM (GRS 2015) to displace the wind profile vertically to account for the influence of obstacles, in the sake of simplicity they are not included in the following equations.

The first model, the default boundary layer model (BLM) of ARTM 2.8.0, was initially suggested by Kerschgens et al. (2000) and is based on the works of Lenschow et al. (1980), Panofsky et al. (1977), and Hicks (1985) and Gryning et al. (1987). It describes profiles for the wind speed fluctuations as

$$\sigma_\mathrm{x} = 2.4 \cdot u_* \left(1 + 0.01486 \frac{-h_\mathrm{m}}{\kappa L}\right)^{\frac{1}{3}} \cdot \exp\left(\frac{-z}{h_\mathrm{m}}\right), \tag{4.7}$$

$$\sigma_\mathrm{y} = 1.8 \cdot u_* \left(1 + 0.03522 \frac{-h_\mathrm{m}}{\kappa L}\right)^{\frac{1}{3}} \cdot \exp\left(\frac{-z}{h_\mathrm{m}}\right) \tag{4.8}$$

and

$$\sigma_\mathrm{z} = 1.3 \cdot u_* \left[\left(1 - 0.8 \frac{z}{h_\mathrm{m}}\right)^3 \cdot \frac{-z}{\kappa L} + \exp\left(\frac{-z}{h_\mathrm{m}}\right)^3\right]^{\frac{1}{3}} \tag{4.9}$$

where u_* is the friction velocity, h_m is the mixing layer height, $\kappa = 0.4$ is the von Kármán constant, L is the Obukhov length and z is the height agl (VDI 3783 part 8 2002; Hanfland et al. 2022). This model is called ARTM2 in the following.

The second TM available in ARTM is based on ARTM2 with a modification in the exponents as well as in the prefactor of u_* of the crosswind component σ_y as

$$\sigma_\mathrm{x} = 2.4 \cdot u_* \left(1 + 0.01486 \frac{-h_\mathrm{m}}{\kappa L}\right)^{\frac{1}{3}} \cdot \exp\left(\frac{-0.3 \cdot z}{h_\mathrm{m}}\right), \tag{4.10}$$

$$\sigma_\mathrm{y} = 2.0 \cdot u_* \left(1 + 0.03522 \frac{-h_\mathrm{m}}{\kappa L}\right)^{\frac{1}{3}} \cdot \exp\left(\frac{-0.3 \cdot z}{h_\mathrm{m}}\right) \tag{4.11}$$

and

$$\sigma_\mathrm{z} = 1.3 \cdot u_* \left[\left(1 - 0.8 \frac{z}{h_\mathrm{m}}\right)^3 \cdot \frac{-z}{\kappa L} + \exp\left(\frac{-0.3 \cdot z}{h_\mathrm{m}}\right)^3\right]^{\frac{1}{3}} \tag{4.12}$$

(Janicke et al. 2011). This model leads to wider plumes and is called PRFMOD in the following.

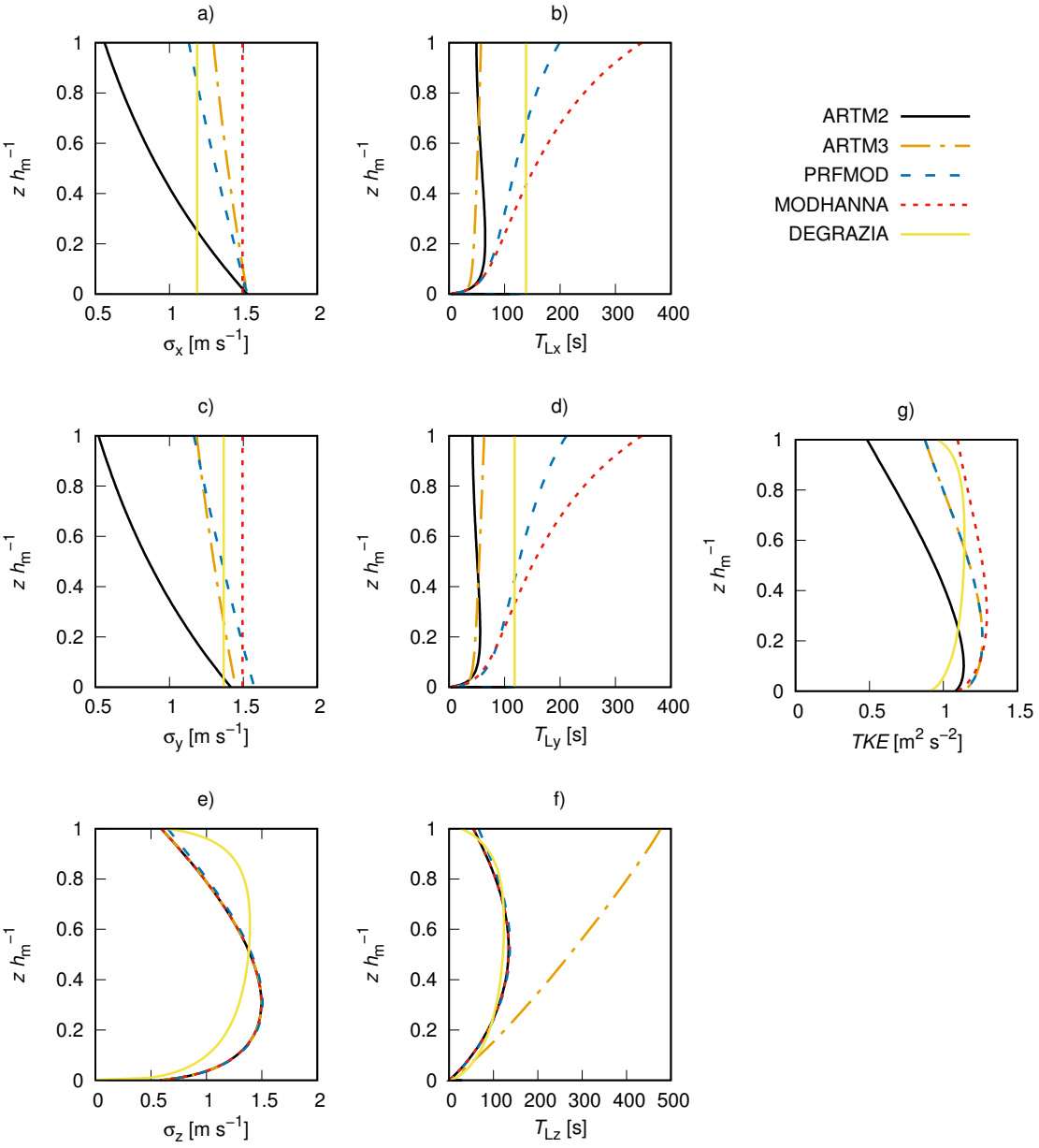

Figure 4.8: Vertical profiles of model characteristics for the five turbulence models ARTM2, ARTM3, PRFMOD, MODHANNA and DEGRAZIA for very unstable atmospheric conditions. Wind speed fluctuations σ: a) along wind direction σ_x; c) in the crosswind direction σ_y; and e) in the vertical direction σ_z against the normalized height (normalised to the boundary layer height). The corresponding Lagrangian correlation times T_L are shown in b), d) and f), respectively. The turbulent kinetic energy *TKE* is shown in g). From Hanfland et al. (2023).

In addition to the two previous models I added a TM to ARTM based on ARTM2 modified with formulations used in other ADMs (Stohl et al. 2005). This model uses σ_z from ARTM2 given in Eq. 4.9 but the horizontal wind speed fluctuations

$$\sigma_{\mathrm{x}} = \sigma_{\mathrm{y}} = u_* \left(12 + \frac{h_{\mathrm{m}}}{2|L|}\right)^{\frac{1}{3}} \tag{4.13}$$

are equal to the equations suggested by Hanna (1982). The aim of this modification is to increase the turbulent kinetic energy and to analyse the effect of the horizontal wind speed fluctuations on the dispersion. In the following, this model is called MODHANNA.

The Lagrangian correlation times of the three models above are given according to Kolmogorov's theory as

$$T_{\mathrm{L}i} = \frac{2 \cdot \sigma_i^2}{\mathrm{C}_0 \cdot \eta} \tag{4.14}$$

(Luhar et al. 1989) with the Kolmogorov constant $\mathrm{C}_0 = 5.7$ and the dissipation rate of the turbulent kinetic energy

$$\eta = \max\left\{\frac{u_*^3}{\kappa z}\left[\left(1 - \frac{z}{h_{\mathrm{m}}}\right)^2 + \frac{z}{h_{\mathrm{m}}}\right] + \frac{-u_*^3}{\kappa L}\left[1.5 - 1.3\left(\frac{z}{h_{\mathrm{m}}}\right)^{\frac{1}{3}}\right], \frac{u_*^3}{\kappa z}\right\}. \tag{4.15}$$

The fourth model is the default model of the new version 3.0.0 of ARTM with the wind speed fluctuations given as

$$\sigma_{\mathrm{x}} = 2.4 \cdot u_* \left[1 + 0.01486 \frac{-h_{\mathrm{m}}}{\kappa L} \cdot \exp\left(-0.9 \frac{z}{h_{\mathrm{m}}}\right)\right]^{\frac{1}{3}}, \tag{4.16}$$

$$\sigma_{\mathrm{x}} = 2.0 \cdot u_* \left[1 + 0.02568 \frac{-h_{\mathrm{m}}}{\kappa L} \cdot \exp\left(-0.9 \frac{z}{h_{\mathrm{m}}}\right)\right]^{\frac{1}{3}} \tag{4.17}$$

and

$$\sigma_{\mathrm{z}} = 1.3 \cdot u_* \left[\left(1 - 0.8 \frac{z}{h_{\mathrm{m}}}\right)^3 \cdot \frac{-z}{\kappa L} + \exp\left(-0.9 \frac{z}{h_{\mathrm{m}}}\right)^3\right]^{\frac{1}{3}} \tag{4.18}$$

(VDI 3783 part 8 2017). The Lagrangian correlation time scales for each component i are calculated via the turbulent diffusion coefficients K_i as

$$T_{\mathrm{L}i} = \frac{K_i}{\sigma_i^2} \tag{4.19}$$

with

$$K_j = 0.9 \frac{u(z) \cdot h_{\mathrm{m}}}{100 \cdot u_*} \sigma_j \tag{4.20}$$

for the horizontal components j and

$$K_z = \kappa u_* z \left[\left(1 - 0.8\frac{z}{h_\mathrm{m}}\right)^4 \frac{9z}{-L} + \exp\left(-3.6\frac{z}{h_\mathrm{m}}\right) \right]^{\frac{1}{2}} \tag{4.21}$$

for the vertical component, respectively (VDI 3783 part 8 2017). This model is called ARTM3 in the following.

I implemented also a fifth model, which in contrast to the previous four turbulence models that are based on similarity theory, is based on the spectral distribution of the turbulent kinetic energy of the boundary layer and was presented by Degrazia et al. (2000). For very unstable boundary conditions the wind speed fluctuations are given as

$$\sigma_\mathrm{x} = 0.53 \cdot u_* \left(\frac{-h_\mathrm{m}}{\kappa L}\right)^{\frac{1}{3}}, \tag{4.22}$$

$$\sigma_\mathrm{y} = 0.61 \cdot u_* \left(\frac{-h_\mathrm{m}}{\kappa L}\right)^{\frac{1}{3}} \tag{4.23}$$

and

$$\sigma_\mathrm{z} = 0.54 \cdot u_* \left(\frac{-h_\mathrm{m}}{\kappa L}\right)^{\frac{1}{3}} \cdot \left\{ 1.8 \left[1 - \exp\left(\frac{-4z}{h_\mathrm{m}}\right) - 0.0003 \cdot \exp\left(\frac{8z}{h_\mathrm{m}}\right) \right] \right\}^{\frac{1}{3}} \tag{4.24}$$

with the Lagrangian correlation times

$$T_{\mathrm{L}i} = \frac{l_{\mathrm{L}i}}{\sigma_i} \tag{4.25}$$

where $l_{\mathrm{L}i}$ is the Lagrangian correlation length given as

$$l_\mathrm{Lx} = l_\mathrm{Ly} = 0.21 \cdot h_\mathrm{m} \left(0.01\frac{h_\mathrm{m}}{-L}\right)^{\frac{1}{2}} \tag{4.26}$$

and

$$l_\mathrm{Lz} = 0.14 \cdot h_\mathrm{m} \left(0.01\frac{h_\mathrm{m}}{-L}\right)^{\frac{1}{2}} \cdot \left\{ 1.8 \left[1 - \exp\left(\frac{-4z}{h_\mathrm{m}}\right) - 0.0003 \cdot \exp\left(\frac{8z}{h_\mathrm{m}}\right) \right] \right\}. \tag{4.27}$$

In this work this TM is denoted as DEGRAZIA.

The turbulent kinetic energy per unit mass is determined as

$$TKE = \frac{1}{2}\left(\sigma_\mathrm{x}^2 + \sigma_\mathrm{y}^2 + \sigma_\mathrm{z}^2\right) \tag{4.28}$$

(Stull 1988).

4.2.2 Simulation setup for the well-mixed condition test

The well-mixed condition test can characterise the vertical mixing homogeneity of a model. For these tests simulation domains with periodic horizontal boundaries and reflecting vertical boundaries are used. This virtually expands the simulation domain to infinite extent and prevents the simulation from losing tracer mass. The whole simulation domain serves as a volume source where 115 200 numerical particles are inserted uniformly within the first simulation hour. The domain size is 2 000 m × 2 000 m × 1 100 m in x-, y-, and z-direction with a horizontal (vertical) resolution of 200 m (25 m), respectively. The vertical extent of the domain is equal to the assumed mixing depth. A temporally constant wind profile for unstable atmospheric conditions, as described in Hanfland et al. (2022) with a wind speed of 2.3 m s^{-1} at 10 m height and a direction of 270 ° (westerly) is used. The selected wind speed originates from measurement sites at very unstable stratification in Germany. For the evaluation, the hourly mean concentration and its standard deviation was derived for each vertical level.

4.2.3 Evaluation of the turbulence models

The concentration profiles of the different TMs for very unstable PBL conditions are shown in Fig. 4.9. The concentration profiles of the state of mixing after one hour (red line) and after two hours (blue dashed line) are shown. Concentration values are normalised to the mean concentration ($c\,\overline{c}^{-1}$) and the height is normalised to the mixing depth ($z\,h_{\mathrm{m}}^{-1}$). I used the same initial numerical particle distribution for all TMs to eliminate possible differences arising from different initial distributions.

The concentration profiles after one hour differ from the uniform distribution $c\,\overline{c}^{-1} = 1$. This indicates a certain degree of segregation of the numerical particles but most deviations are less than 5% (vertical dotted lines). The largest deviations can be found at the top of the PBL for the ARTM3 model (> 35%) and the DEGRAZIA model (> 15%). The profiles of the ARTM2 and the MODHANNA turbulence models are very similar since they both contain the same vertical turbulence parametrisation. The PRFMOD TM differs slightly from the ARTM2 model due to modifications described in Eq. 4.12. The profile of ARTM3 shows trends of dilution and accumulation similar to ARTM2, PRFMOD and MODHANNA, which have similar vertical parametrisations, but magnified in its extent. The profile of the DEGRAZIA turbulence model shows a different shape because of its different formulation of the turbulence parameters (see Eqs. 4.24, 4.25 and 4.27).

By $t = 2\,\mathrm{h}$, the dilution has further increased at the bottom and the top of the PBL and the accumulation at $z\,h_{\mathrm{m}}^{-1} \approx 0.3$ (horizontal dashed black line in Fig. 4.9 a has further increased partly beyond 5% but well below 10% deviation

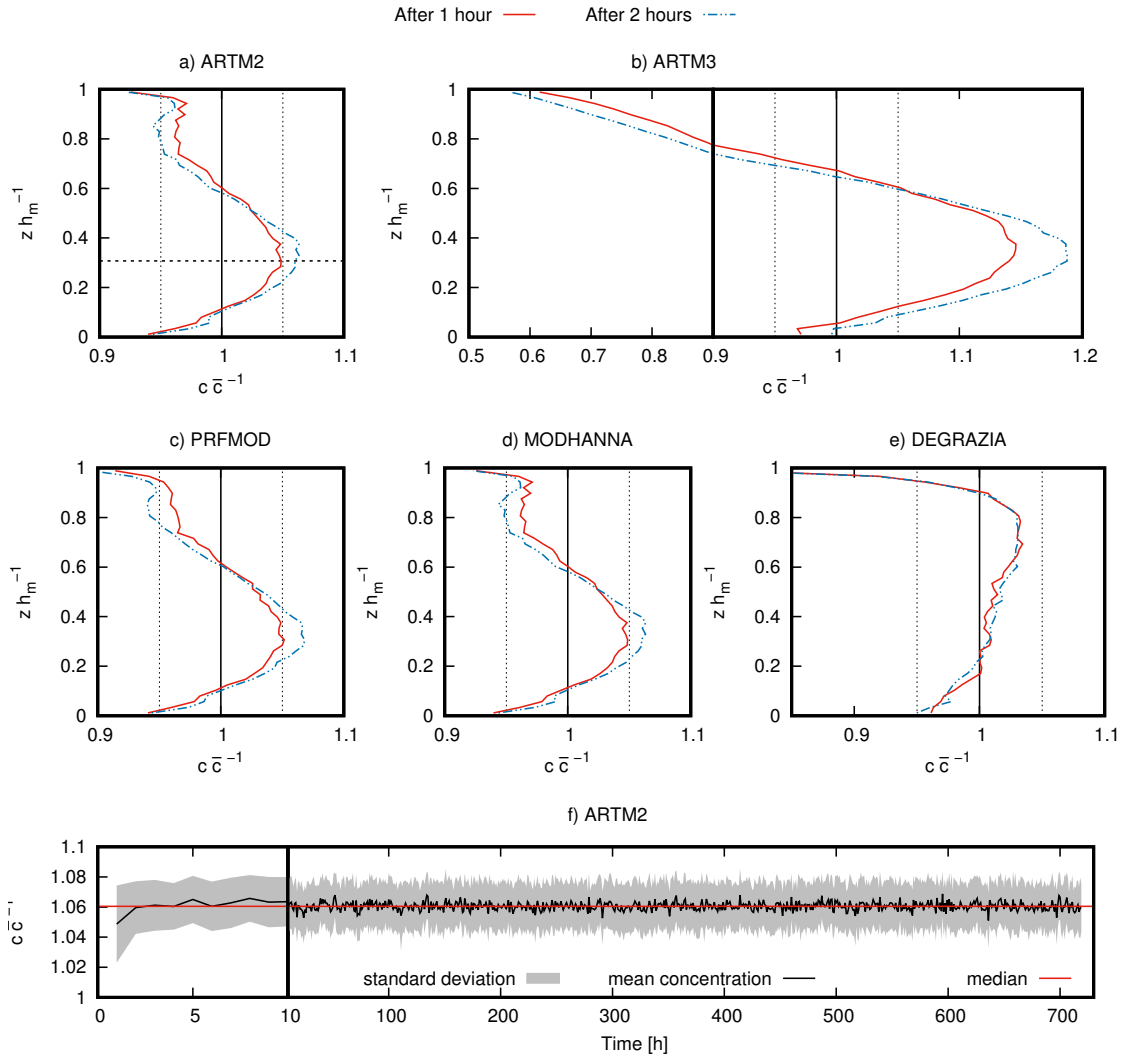

Figure 4.9: Profiles of the concentration normalised to the mean concentration $c\,\overline{c}^{-1}$ (a, b, c, d, e) of the different turbulence models ARTM2, ARTM3, PRFMOD, MODHANNA and DEGRAZIA after one hour (red lines) and two hours (blue dashed dotted lines) for periodic lateral simulation domain boundaries and reflecting bottom and top boundaries. The wind speed at 10 m height is 2.3 m s^{-1}. In b) the x-axis scale changes at $c\,\overline{c}^{-1} = 0.9$. f) Time series of the normalised concentration at normalised height $z\,h_{\mathrm{m}}^{-1} \approx 0.3$ for the ARTM2 model, which is indicated by the dashed horizontal line in a). The x-axis scale changes at 10 hours. From Hanfland et al. (2023).

for ARTM2, PRFMOD, MODHANNA and DEGRAZIA. For ARTM3, the dilution at the ground almost vanishes while the dilution above $z\,h_{\mathrm{m}}^{-1} = 0.8$ increases to 40% and the accumulation in the middle of the PBL increases to 18%. After the second hour, no further changes are observed as it can be seen in Fig. 4.9 f for the ARTM2 turbulence model at $z\,h_{\mathrm{m}}^{-1} \approx 0.3$. Time series for other heights and other TMs show similar behaviour. Figure 4.10 shows the time series for ARTM2 at the height levels of $z\,h_{\mathrm{m}}^{-1} \approx 0$ (12.5 m agl) and $z\,h_{\mathrm{m}}^{-1} \approx 1$ (1 087.5 m agl). For the other TMs the concentration fluctuates around the median within the standard deviation as it is shown in the Figs. 4.11, 4.12, 4.13 and 4.14, respectively. The concentration becomes steady after the initialisation during the first two hours.

This well-mixed condition test shows that the simulation result systematically overestimates the concentration values at $z\,h_{\mathrm{m}}^{-1} \approx 0.3$ for the ARTM2, PRFMOD and the MODHANNA model after the second hour. Near the surface, which is important for estimation of exposure to the population, the concentration values are underestimated. In both cases, the errors are only 5 - 6%. At the top of the PBL, the models underestimate the expected concentration significantly. The ARTM3 turbulence model shows the smallest deviation from the mean domain concentration near the ground but it overestimates the concentration in the middle of the PBL before turning into a substantial underestimation towards the mixing layer top. Below $z\,h_{\mathrm{m}}^{-1} = 0.8$ the TM DEGRAZIA performs best. At the top of the PBL the model decreases well below the expected concentration. All the tested TMs can be assumed as acceptable for simulations at very unstable atmospheric conditions but the partly large deviations of the concentration from the expected values at certain heights have to be taken into account when interpreting model results. At low-wind conditions ($1\,\mathrm{m\,s^{-1}}$ at 10 m height) the deviation from the uniform concentration is similar (see Fig. 4.15).

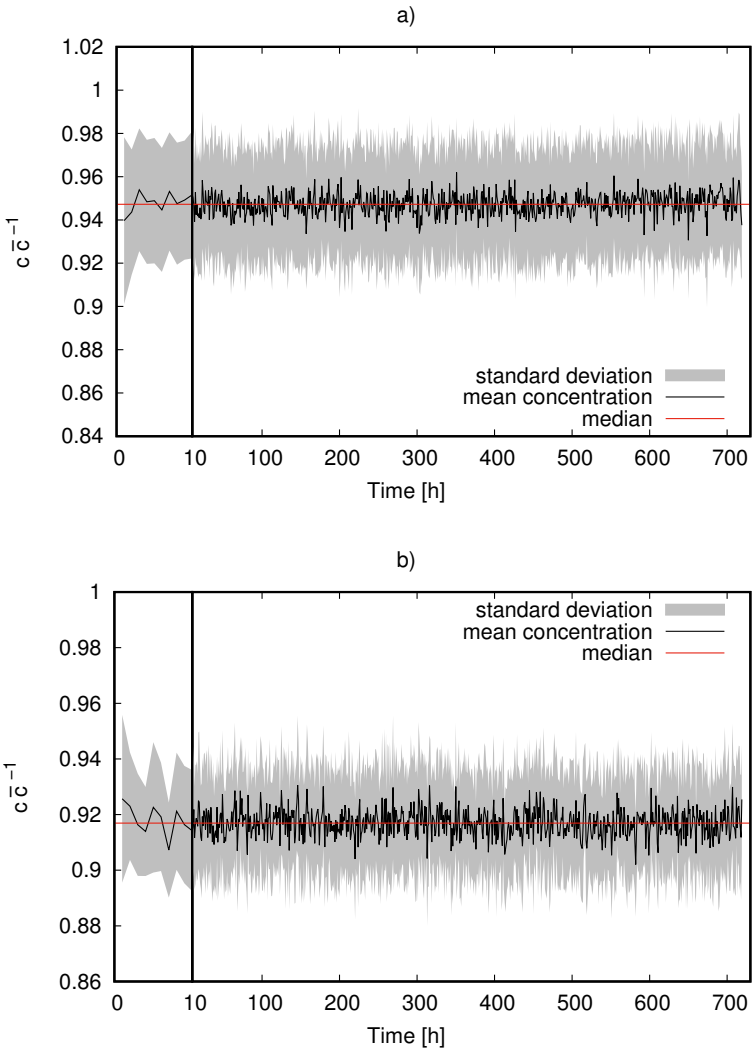

Figure 4.10: Time series of the normalised concentration for the ARTM2 turbulence model at a) $z\,h_{\mathrm{m}}^{-1} \approx 0$ (12.5 m agl) and b) $z\,h_{\mathrm{m}}^{-1} \approx 1$ (1 087.5 m agl) for 30 days (720 h). From Hanfland et al. (2023, Supplement).

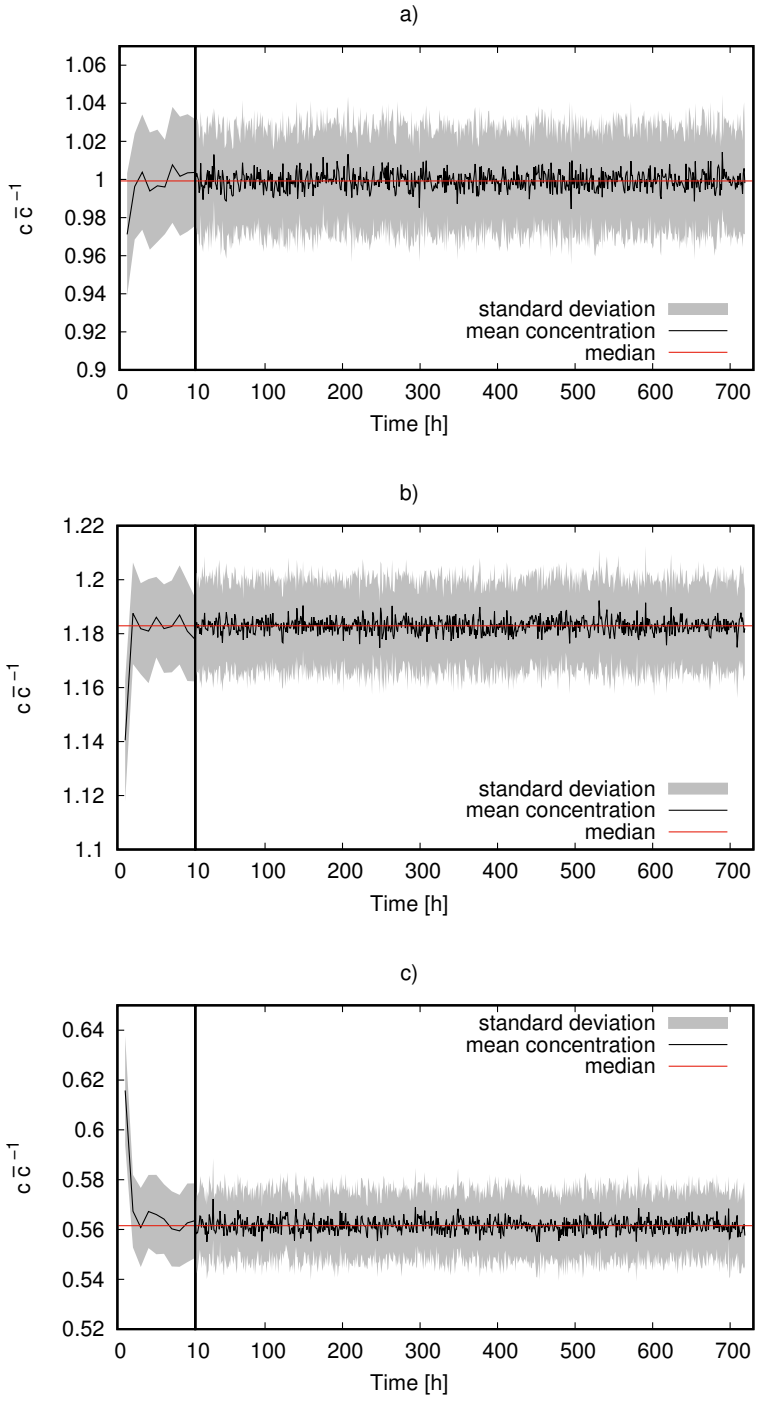

Figure 4.11: Time series of the normalised concentration for the ARTM3 turbulence model at a) $z\,h_{\mathrm{m}}^{-1} \approx 0$ (12.5 m agl), b) $z\,h_{\mathrm{m}}^{-1} \approx 0.3$ (337.5 m agl) and c) $z\,h_{\mathrm{m}}^{-1} \approx 1$ (1 087.5 m agl) for 30 days (720 h). From Hanfland et al. (2023, Supplement).

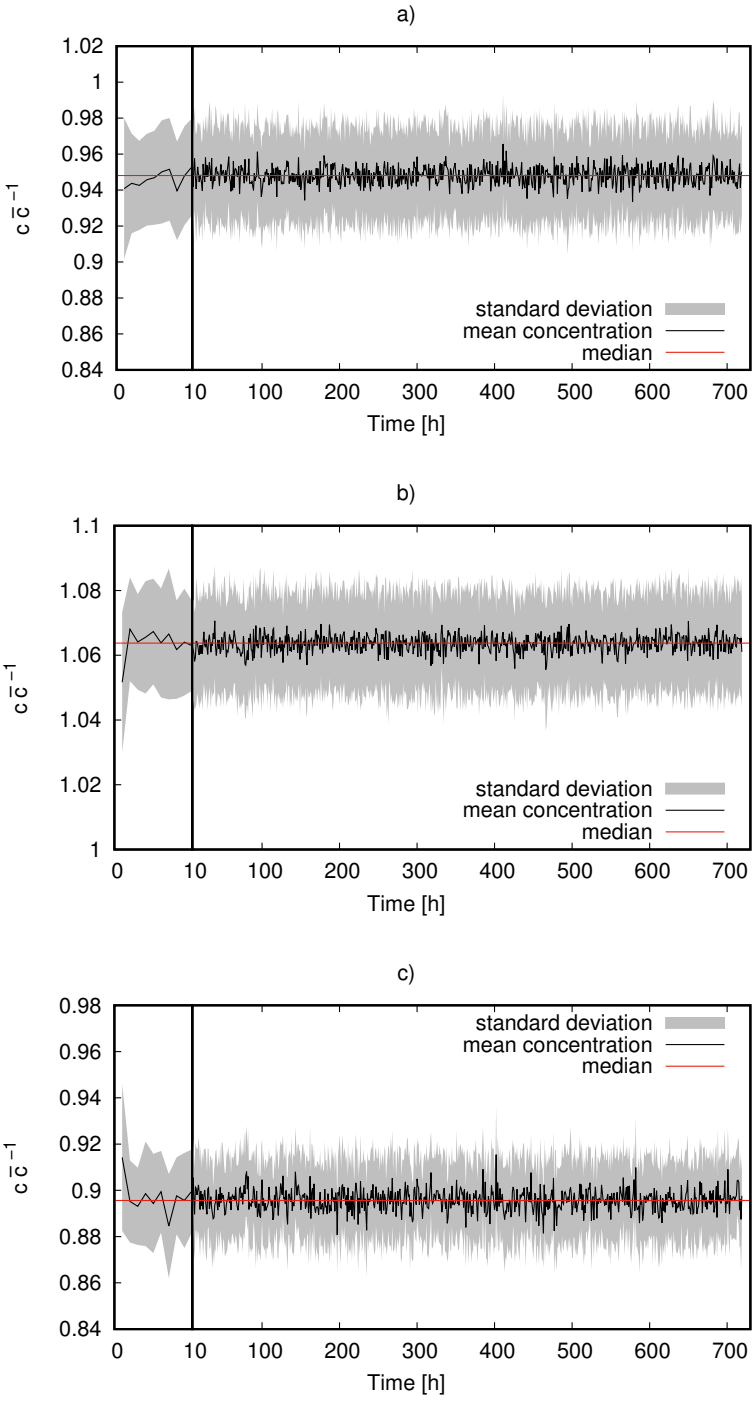

Figure 4.12: Time series of the normalised concentration for the PRFMOD turbulence model at a) $z\,h_{\mathrm{m}}^{-1} \approx 0$ (12.5 m agl), b) $z\,h_{\mathrm{m}}^{-1} \approx 0.3$ (337.5 m agl) and c) $z\,h_{\mathrm{m}}^{-1} \approx 1$ (1 087.5 m agl) for 30 days (720 h). From Hanfland et al. (2023, Supplement).

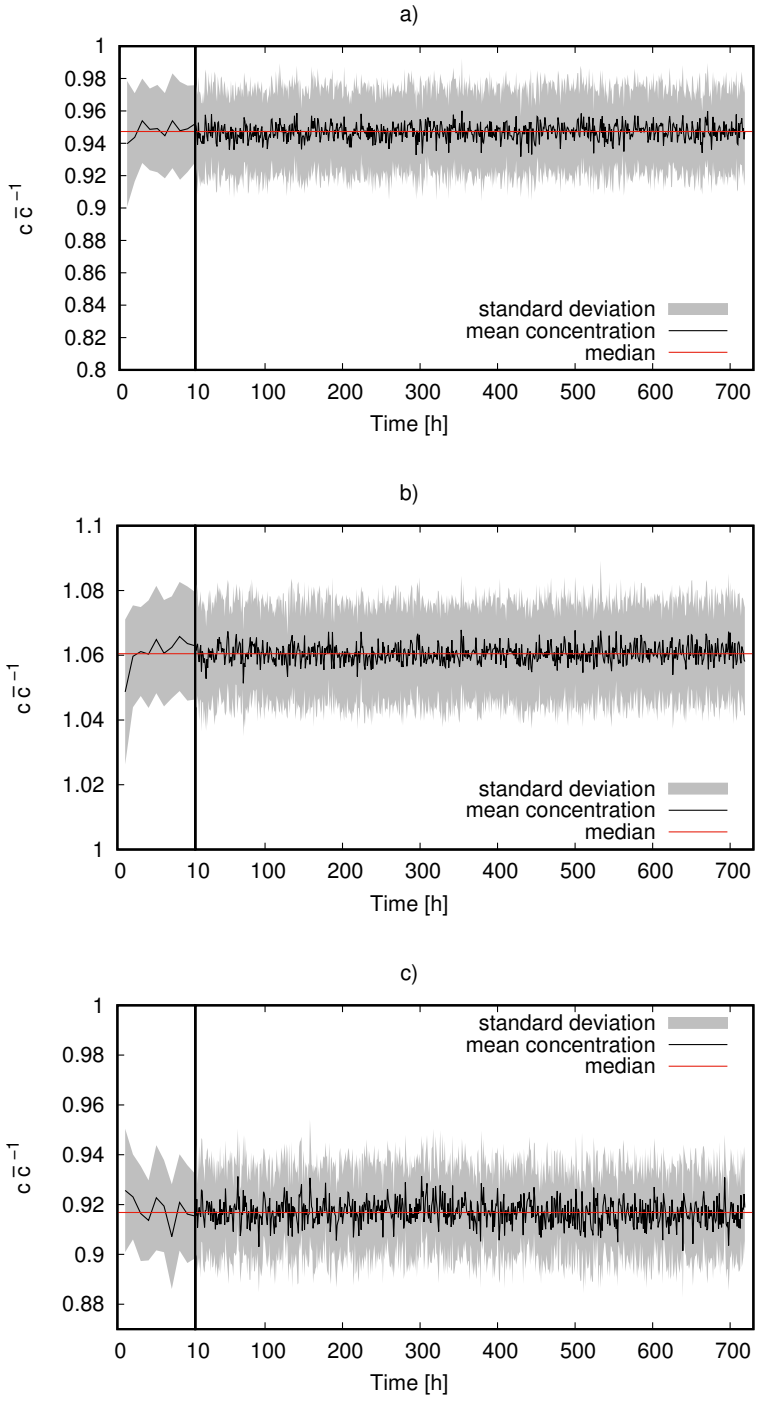

Figure 4.13: Time series of the normalised concentration for the MODHANNA turbulence model at a) $z\,h_{\mathrm{m}}^{-1} \approx 0$ (12.5 m agl), b) $z\,h_{\mathrm{m}}^{-1} \approx 0.3$ (337.5 m agl) and c) $z\,h_{\mathrm{m}}^{-1} \approx 1$ (1 087.5 m agl) for 30 days (720 h). From Hanfland et al. (2023, Supplement).

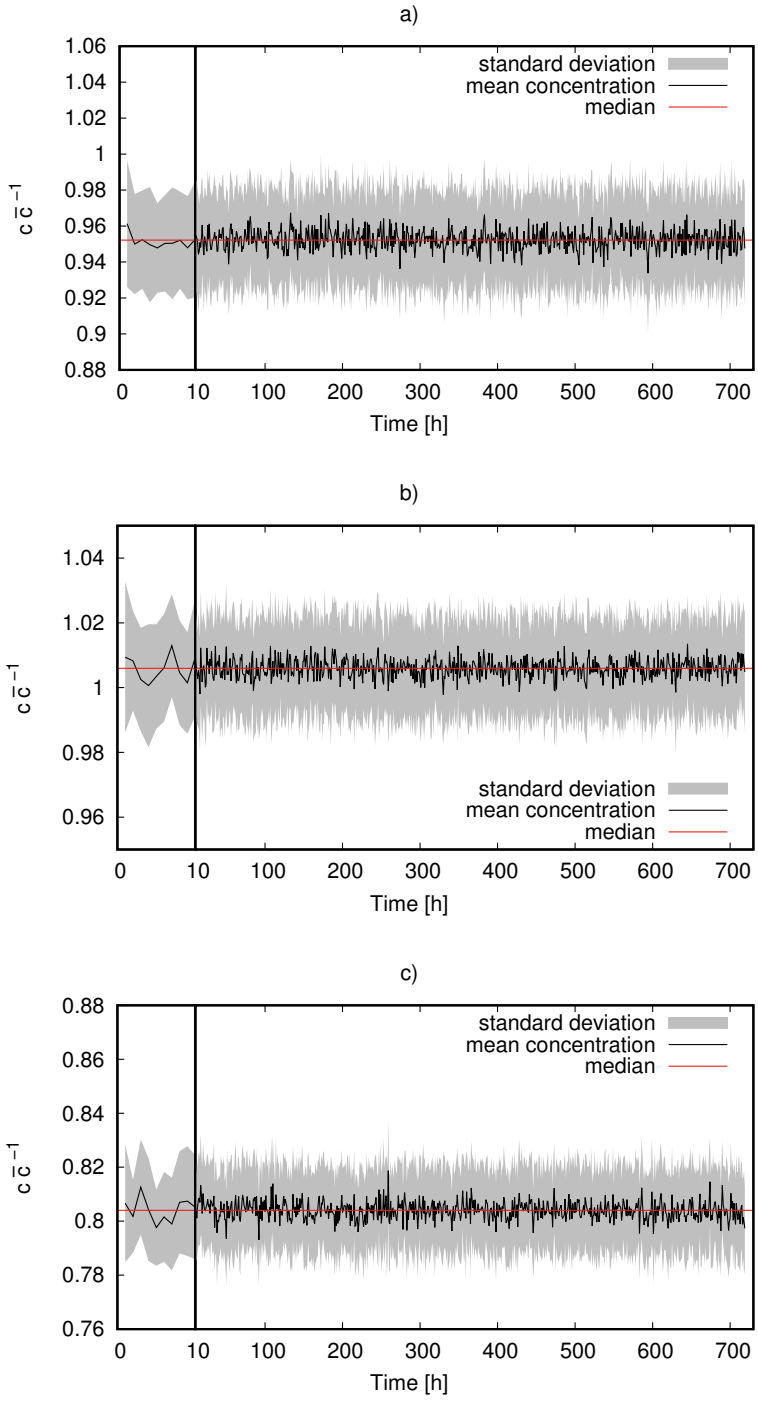

Figure 4.14: Time series of the normalised concentration for the DEGRAZIA turbulence model at a) $z\,h_{\mathrm{m}}^{-1} \approx 0$ (12.5 m agl), b) $z\,h_{\mathrm{m}}^{-1} \approx 0.3$ (337.5 m agl) and c) $z\,h_{\mathrm{m}}^{-1} \approx 1$ (1 087.5 m agl) for 30 days (720 h). From Hanfland et al. (2023, Supplement).

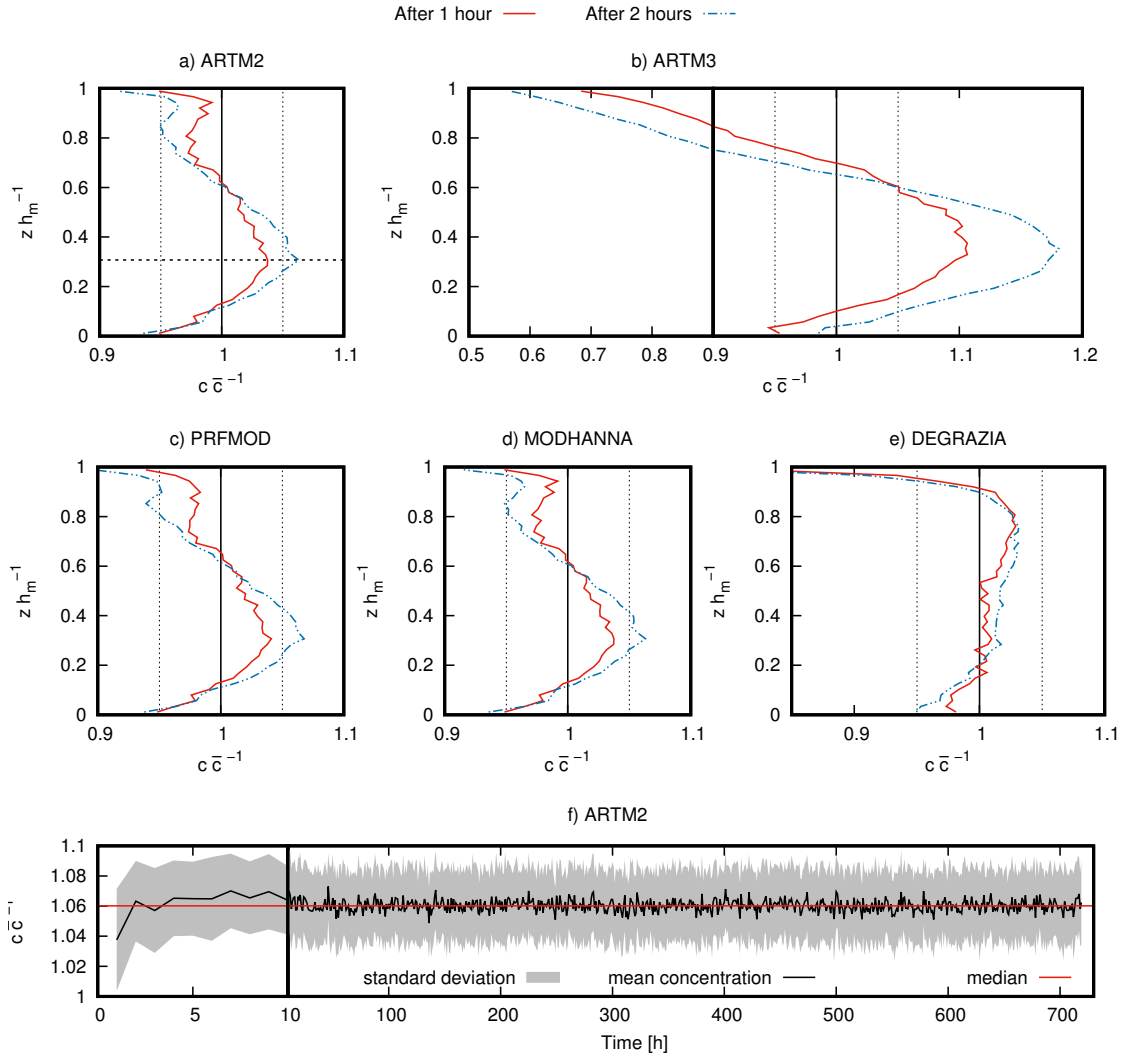

Figure 4.15: Profiles of the concentration normalised to the mean concentration $c\,\overline{c}^{-1}$ (a, b, c, d, e) of the different turbulence models ARTM2, ARTM3, PRFMOD, MODHANNA and DEGRAZIA after one hour (red lines) and two hours (blue dashed dotted lines) for periodic lateral simulation domain boundaries and reflecting bottom and top boundaries. The wind speed at 10 m height is $1\,\mathrm{m\,s^{-1}}$. In b) the x-axis scale changes at $c\,\overline{c}^{-1} = 0.9$. f) Time series of the normalised concentration at normalised height $z\,h_\mathrm{m}^{-1} \approx 0.3$ for the ARTM2 model, which is indicated by the dashed horizontal line in a). The x-axis scale changes at 10 hours. From Hanfland et al. (2023).

Chapter 5

Evaluation of ARTM

This chapter describes the comparison of simulation results of ARTM with measurement data and with other atmospheric transport model results. Parts of this chapter are published in Hanfland et al. (2023) and Brunner et al. (2023). Major parts of the Section 5.1 (Subsecs. 5.1.1, 5.1.2 and 5.1.3) are published in Hanfland et al. (2023) and are cited here. All analyses and findings of Section 5.2 (Subsecs. 5.2.1, 5.2.2, 5.2.3 and 5.2.4) are published in Brunner et al. (2023) and cited here. In order to simplify readability, there will be no further citations at the mentioned text parts in this chapter.

5.1 Comparison of ARTM simulation results with observations

The comparison of atmospheric dispersion simulation results with measurements near the ground is not sufficient to derive any conclusions about the three-dimensional structure of simulated emission plumes. To study the agreement of simulated and observed plume dispersion it is inevitable to use observations that resolve the three-dimensional structure of the real plume. Since ARTM simulates the emissions of nuclear facilities with source heights of mainly 100 m to 200 m, it is useful to choose observational data originating from similar height levels. In this section, I present a comparison of ARTM simulations with airborne in situ CO_2 observations within the PBL. In such a case, the comparison is challenging because of the turbulent character of the PBL. As pointed out by Brunner et al. (2023), observations only provide snap-shots of the real world while simulations provide one realisation of a multitude of stochastic representations of the real world. Simulations with slightly perturbed initial conditions could result in different dispersion patterns of the plume. Furthermore, simulation results and observations may have different spatial and temporal resolutions and uncertainties, which complicate the

comparison of simulations with observations (Farchi et al. 2016). Thus, in this section, the comparison of simulation results with observations for five TMs is given using rather general plume characteristics such as the plume width per transect and maximum mixing ratios (Hanfland et al. 2023).

5.1.1 Observational data

The aircraft observations used for this investigation originate from the Carbon Dioxide and Methane Mission (CoMet 1.0) (Fix et al. 2018; Luther et al. 2019; Fiehn et al. 2020; Gałkowski et al. 2021; Wolff et al. 2021; Krautwurst et al. 2021; Andersen et al. 2023; Brunner et al. 2023). The campaign took place in May and June 2018 and involved three aircraft, two from the German aerospace center (DLR) and one from the Freie Universität Berlin (FUB), performing in situ and remote sensing measurements. The objective was to study CO_2 and methane (CH_4) emissions from different sources in Europe including power plants, as well as to compare the different observational methods.

For the evaluation of ARTM, airborne in situ CO_2 measurements in the vicinity of the Bełchatów power plant in Poland were used (Fiehn et al. 2020; Kostinek et al. 2021). An overview map with the CO_2 mixing ratios along the flight path is shown in Fig. 5.1.

The in situ measurements had been performed on 7 June 2018 between 13:00 and 15:00 UTC aboard the DLR Cessna Grand Caravan 208B. One transect on

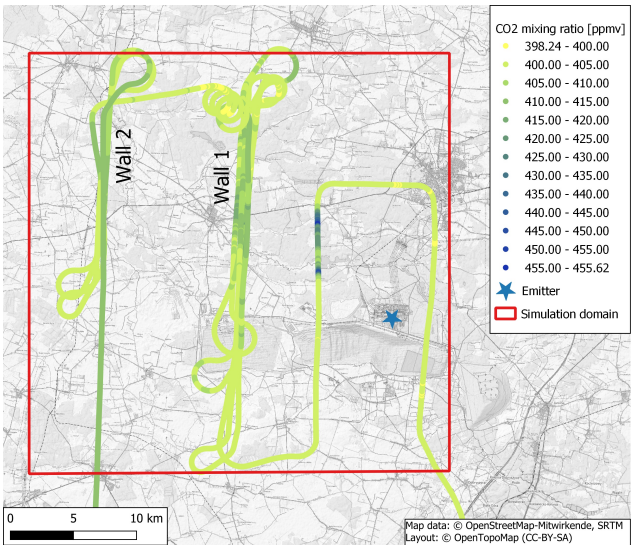

Figure 5.1: Map showing the flight path of the DLR Cessna aircraft in the vicinity of the Bełchatów lignite power plant (blue star), colour coded by the in situ measured CO_2 values. Transects were performed both east (upwind side) and west (downwind side) of the emitting power plant. The red box indicates the simulation domain. From Hanfland et al. (2023).

the upwind side of the emitter was performed at the beginning in order to derive the mean background CO_2 mixing ratio $\overline{c_{CO_2}} = 401.2$ ppmv. The exhaust plume of the power plant was probed during several transects on the downwind side at heights between 500 m and 1 700 m agl. They form two wall patterns at meridional distances of approx. 13 km (Wall 1) and 23 km (Wall 2) and a single transect at approx. 6 km from the source.

CO_2 was measured with a cavity ring-down spectroscopy analyser (G1301-m, Piccaro) specifically modified for the airborne deployment operating at 0.5 Hz. the CO_2 measurement uncertainty is ± 0.15 ppmv and the temporal resolution was increased to 1 s by interpolation to make the data comparable with other data collected during the campaign. Details of the measurement equipment and related uncertainties are described by Klausner et al. (2020). The sampling repetition and the velocity of the aircraft results in a spatial distance of about 140 m between the 0.5 Hz data points. The Picarro instrument measures CO_2, methane and water vapour sequentially and , thus, the values are representative for the last third of the measurement interval. Observational data for wind direction, wind speed and flight height is displayed in Fig. 5.2. The original data had been transformed to the height above ground level instead of the altitude above mean sea level (Hanfland et al. 2023).

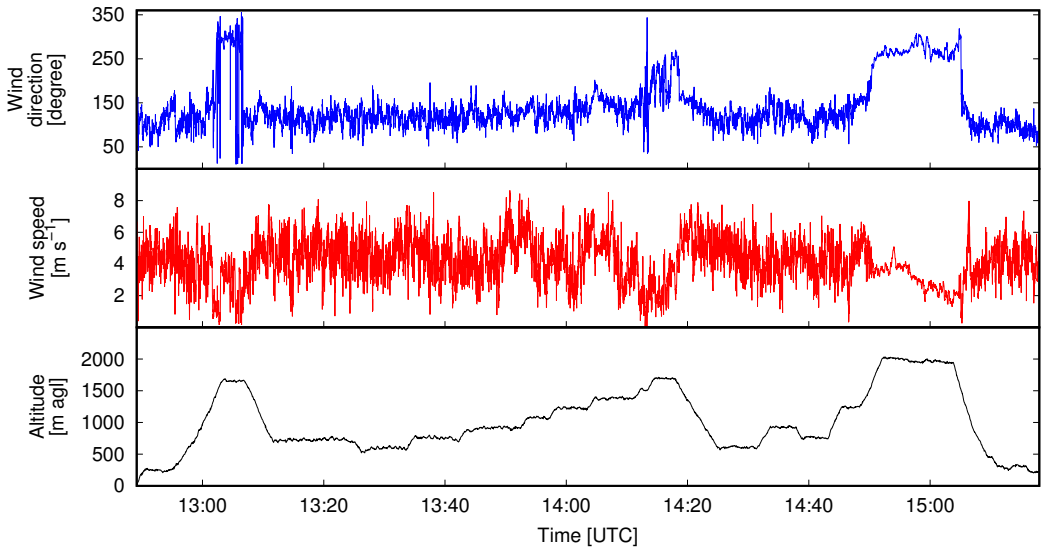

Figure 5.2: Wind direction, wind speed and flight height measured by the DLR Cessna during the measurement flight. From Hanfland et al. (2023, Supplement).

5.1.2 Simulation setups for the model evaluation

I set the simulation domain 33.3 km × 33.3 km × 1.9 km that covers the horizontal extent of the flight trajectory and vertically extends beyond the mixing layer depth by four simulation levels. The horizontal resolution was 150 m in both east and west direction. The extent of the simulation domain with the location of the emission source (two stacks in a distance of 300 m) is shown in Fig. 5.1. Vertically, the grid spacing gradually increases from 3 m to 35 m until 100 m height is reached. Above, 50 m level thickness was used. All level thicknesses are given in Tab. 5.1.

Table 5.1: Horizontal levels used for the simulations when comparing ARTM with observations. The height of the lower level boarder agl and the level thickness are given in meter. After Hanfland et al. (2023, Supplement)

level	lower boundary height [m]	thickness [m]	level	lower boundary height [m]	thickness [m]
41	1 800	100	20	650	50
40	1 750	50	19	600	50
39	1 700	50	18	550	50
38	1 650	50	17	500	50
37	1 600	50	16	450	50
36	1 550	50	15	400	50
35	1 400	50	14	350	50
34	1 350	50	13	300	50
33	1 300	50	12	250	50
32	1 250	50	11	200	50
31	1 200	50	10	150	50
30	1 150	50	9	100	50
29	1 100	50	8	65	35
28	1 050	50	7	40	25
27	1 000	50	6	25	15
26	950	50	5	16	9
25	900	50	4	10	6
24	850	50	3	6	4
23	800	50	2	3	3
22	750	50	1	0	3
21	700	50			

ARTM requires several input parameters: SC, z_0, d_0, orography, several source specific parameters as well as wind speed and direction at one location in the simulation domain. Since there were no stationary ground-based wind measurements available, wind direction and wind velocity as well as SC and mixing layer height were derived from the airborne measurements. The emission rates were unknown. However, Brunner et al. (2023) estimated the overall CO_2 emission rate according to the generated electrical power of the power plant resulting in $1503.0\,\mathrm{kg\,s^{-1}}$ during the measurement flight. This corresponds to 123% of the annual mean emission rate of the total 38.4 Mt CO_2 reported by the power plant to the European Pollutant Release and Transfer Register (E-PRTR) for the year 2018. The SC was determined according to the scheme given in KTA 1508 (2017) from the horizontal wind direction fluctuations measured on several transects at different height levels and was classified as "very unstable" during the observations (Klug 1969). For the determination of the roughness length z_0, the CORINE Land Cover Inventory of 2018 and the categorisation after TA Luft (2002) was used. The area is covered mainly by arable land, pastures, coniferous and mixed forest leading to a mean value of $z_0 = 0.5\,\mathrm{m}$ for the simulation domain. The zero-plane displacement was assumed to be $d_0 = 6 \cdot z_0$ (TA Luft 2002). The mixing layer height of 1650 m was derived from the observations by locating the abrupt decrease in the wind speed fluctuation (see Fig. 5.2). The elevation data originates from the Shuttle Radar Topography Mission version 3 (SRTM3) that has a spatial resolution of 3 arc-seconds ($\approx 90\,\mathrm{m}$) (Farr et al. 2007; Hanfland et al. 2023). The stacks are

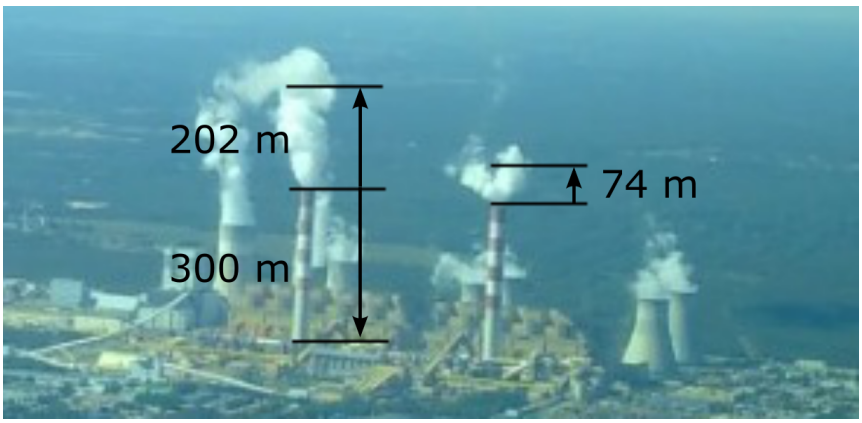

Figure 5.3: Photograph of the Bełchatów power plant taken by Alina Fiehn from the measuring aircraft during the measurement flight on 7 June 2018 at 13:13 UTC. The stack height as well as the plume rise for both stacks is given in the image. The photograph was taken from the south-south-east of the power plant. From Hanfland et al. (2023, Supplement).

assumed to have had different emission rates (two-thirds : one-third) because photographs (see Fig. 5.3) taken from the aircraft showed markedly different plume

rise heights for the two stacks. These plume rises are assumed to be 202 m and 74 m, respectively (Hanfland et al. 2023). The parameter values and the origin of the orography data are summarised in Tab. 5.2.

Table 5.2: Input parameters needed by ARTM that are constant during the simulation run. From Hanfland et al. (2023).

Parameter	Value	Reference
Stability class	very unstable	(KTA 1508 2017)
Roughness length	0.50 m	(TA Luft 2002)
Zero-plane displacement	$6 \cdot 0.50$ m	(TA Luft 2002)
Mixing layer height	1 650 m	-
Stack heights	300 m	(SkyscraperPage 2023)
Plume rise (western stack)	202 m	-
Plume rise (eastern stack)	74 m	-
Emission rate (western source)	1 002.0 kg s^{-1}	(Brunner et al. 2023)
Emission rate (eastern source)	501.0 kg s^{-1}	(Brunner et al. 2023)
Orography	SRTM3 data	(Farr et al. 2007)

ARTM requires radionuclide emission rates in Bq s^{-1}. As tracer CO_2 with the radioactive isotope ^{14}C is used. Its decay constant $\lambda = 5\,730 \pm 40$ years leads to a decay of 5.5×10^{-6} % within the simulation period, which is negligible. Thus, ARTM's internal emission rates in Bq s^{-1} can be used as an equivalent for a mass rate in kg s^{-1} and to convert activity concentration into mixing ratio.

The wind speed (4.4 m s^{-1}) and directions driving the simulation were derived from one flight transect (13:28:03 UTC to 13:33:14 UTC) at a distance of approx. 13 km to the west of the power plant at a height of approx. 600 m agl. This transect is located close to the middle of the simulation domain. The histogram of the wind directions of this transect is shown in Fig. 5.4. Based on this histogram, two different setups of the model were selected:

i) a single wind direction of 120° (mean of the distribution), assuming that the wind fluctuations are part of the turbulence spectrum and should therefore be represented by the turbulence parametrisation of ARTM; and

ii) two different wind directions were used alternatingly to drive ARTM, a direction of 106° (mean of all directions $< 120°$) and a direction of 134° (mean of all directions $> 120°$). This assumes that part of the wind variation is due to meso-scale variability that cannot be resolved by ARTM's turbulence scheme.

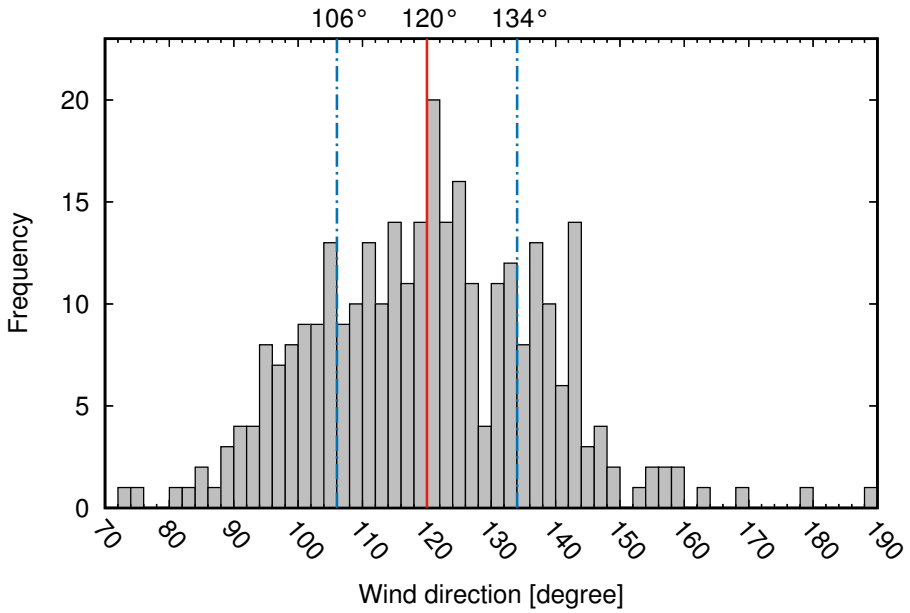

Figure 5.4: Histogram of the wind directions of the transect chosen for the determination of the wind direction and wind velocity. The transect covers a duration from 13:28:03 to 13:33:14 UTC with the mean position 53.31° N, 19.15° E. The mean measurement height is 599 m agl. The mean value of the wind direction is 120° (red line). The mean value for the wind directions below 120° is 106°, above 120° is 134° (blue dashed dotted lines), respectively. From Hanfland et al. (2023).

The first setup was applied for all TMs while the second setup was only tested for ARTM2. The hourly sequence of wind inputs for the model is summarised in Tab. 5.3. Additional spin-up time before the measurement flight is simulated to

Table 5.3: Hourly inputs for wind direction and wind velocity at 599 m height for the two cases: one mean wind direction; and two alternating wind directions for the time from 13:00 to 15:00 UTC. The time stamps describe the full hour before the time given in the time column. The measurement flight was performed during step 14:00 and 15:00 UTC and is marked with [1)]. Data from the ECMWF ERA5 data set for 925 hPa pressure level (≈ 600 m agl) are marked with [2)]. From Hanfland et al. (2023, Supplement).

	Single wind direction		Dual wind direction	
Time [UTC]	wind direction [degree]	wind velocity [m s^{-1}]	wind direction [degree]	wind velocity [m s^{-1}]
09:00	120	4.4	101 [2)]	7.1 [2)]
10:00	120	4.4	107 [2)]	6.1 [2)]
11:00	120	4.4	105 [2)]	5.7 [2)]
12:00	120	4.4	103 [2)]	5.6 [2)]
13:00	120	4.4	106	4.4
14:00 [1)]	120	4.4	134	4.4
15:00 [1)]	120	4.4	106	4.4

ensure a fully developed plume within the simulation domain. For the single wind direction case, the mean wind speed of 4.4 m s^{-1} from the reference transect was used for the simulation time period at approx. 600 m. For the dual wind direction case, reanalysis data from ERA5 were used for the spin-up at the 925 hPa pressure level (≈ 600 m).

5.1.3 Evaluation of the three-dimensional dispersion of simulated plumes

Horizontal dispersion

The mixing ratio maps simulated with the five TMs at a height of 750 m to 800 m are shown in Fig. 5.5 together with the observations between 700 m to 800 m. I subtracted the background CO_2 mixing ratio of 401 ppmv from the observation to get the excess mixing ratio and to make them comparable to the simulation results.

The simulated and observed mixing ratios of the plumes are in the same order of magnitude. The simulated plumes show the mean wind direction to be in agreement with the observed one, however, the meandering behaviour of the real

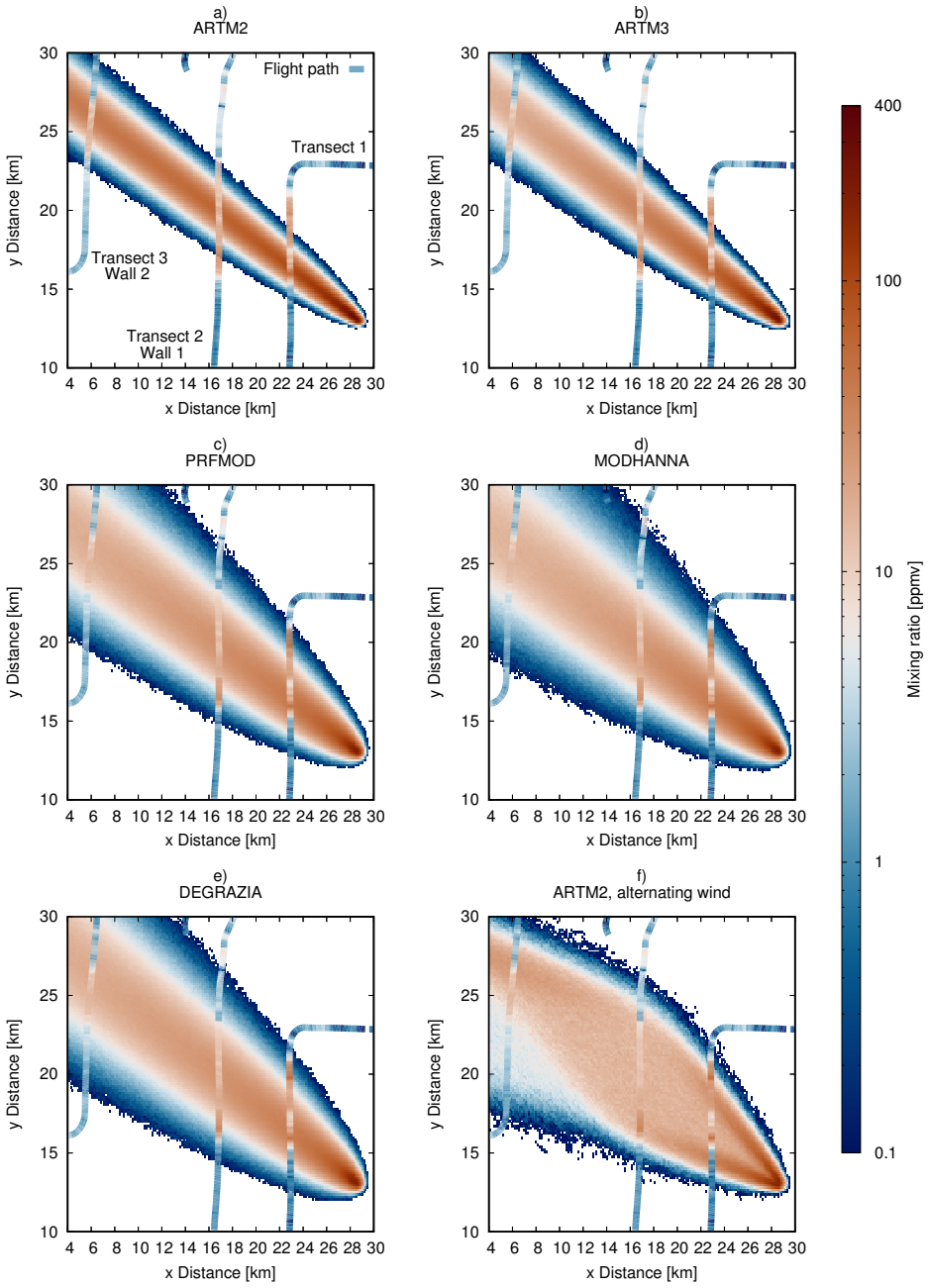

Figure 5.5: Modelled CO_2 mixing ratio averaged over the simulation time for the case of one wind direction for a) ARTM2, b) ARTM3, c) PRFMOD, d) MODHANNA and e) DEGRAZIA; and two wind directions for f) ARTM2 at heights between 750 m to 800 m. The wind directions and speeds are given in Tab. 5.3; the input parameters in Tab. 5.2. The in situ data along the flight path between 700 m to 800 m is shown in logarithmic scale in ppmv. f) The two wind direction case in f) shows the mean CO_2 mixing ratio of two subsequent hours for the duration of the measurement flight from 13:00 UTC to 15:00 UTC. The background CO_2 mixing ratio of 401 ppmv is subtracted from the observation. From Hanfland et al. (2023).

plume that shifts the plume in north-south direction can be observed at transect 1, 2 and 3 in Fig. 5.5 revealing that this behaviour is not covered by all TMs. The mixing ratio profile in lateral (crosswind) direction simulated by ARTM resembles a Gaussian distribution. This is expected for a constant wind direction and wind speed (Thykier-Nielsen et al. 1999).

The different TMs clearly have an influence on the shape of the simulated plume. ARTM2 TM simulates the narrowest plume. The ARTM3 model results in a slightly wider plume but compared to the observations they are too narrow. The PRFMOD and DEGRAZIA turbulence model show much broader plumes that cover the observed one better. The widest plume is simulated by the MODHANNA turbulence model and is in good agreement with the observed plume width. The width of the plumes of the TMs is mainly attributed to the horizontal wind speed fluctuations and Lagrangian correlation times displayed in Fig. 4.8. The highest values for σ_y and $T_{\mathrm{L}y}$ in the upper half of the PBL are simulated by MODHANNA, PRFMOD and DEGRAZIA followed by ARTM3 and ARTM2 in agreement with the simulated plume widths.

Fig. 5.6 shows the simulated and observed plumes of the different turbulence models together with the flight height agl along the flight path. Transects 1, 2 and 3 are shaded grey. Data above the simulated top of the boundary layer are excluded from the figures. In Fig. 5.6, the simulated maximum CO_2 mixing ratios of ARTM2 are at all transects larger compared to the observations. Within the simulated boundary layer this deviation reaches 300% at 14:08 UTC and is attributed to the too narrow simulated plume. With increasing plume width of the different TMs the maximum mixing ratios decrease (see Figs. 5.6 a – e). The turbulence model ARTM3, PRFMOD, MODHANNA and DEGRAZIA simulate mixing ratio peaks similar to or below the observed values. Due to dispersion the mixing ratio maximums decrease with increasing distance from the source for all models in agreement with the observation. It is important to point out that simulated mixing ratio values are highly dependent on the emission rates.

The model provides results in hourly resolution, which are expected as the mean of several realisations of meandering plumes. It is not expected that simulated values are much larger than the observed ones but this can occur if the width of the simulated plume or the mixing layer depth are underestimated or the emission rate is overestimated.

An alternative way to model the meandering behaviour via the turbulence is the usage of alternating wind directions for subsequent simulation hours for the ARTM2 turbulence model to explicitly simulate the meandering plume (see Figs. 5.5 f and 5.6 f). Simulation results from subsequent hours are combined by calculating the average concentrations. The wind direction derivation is explained in Sec. 5.1.2. This method generates the widest plume covering the observations

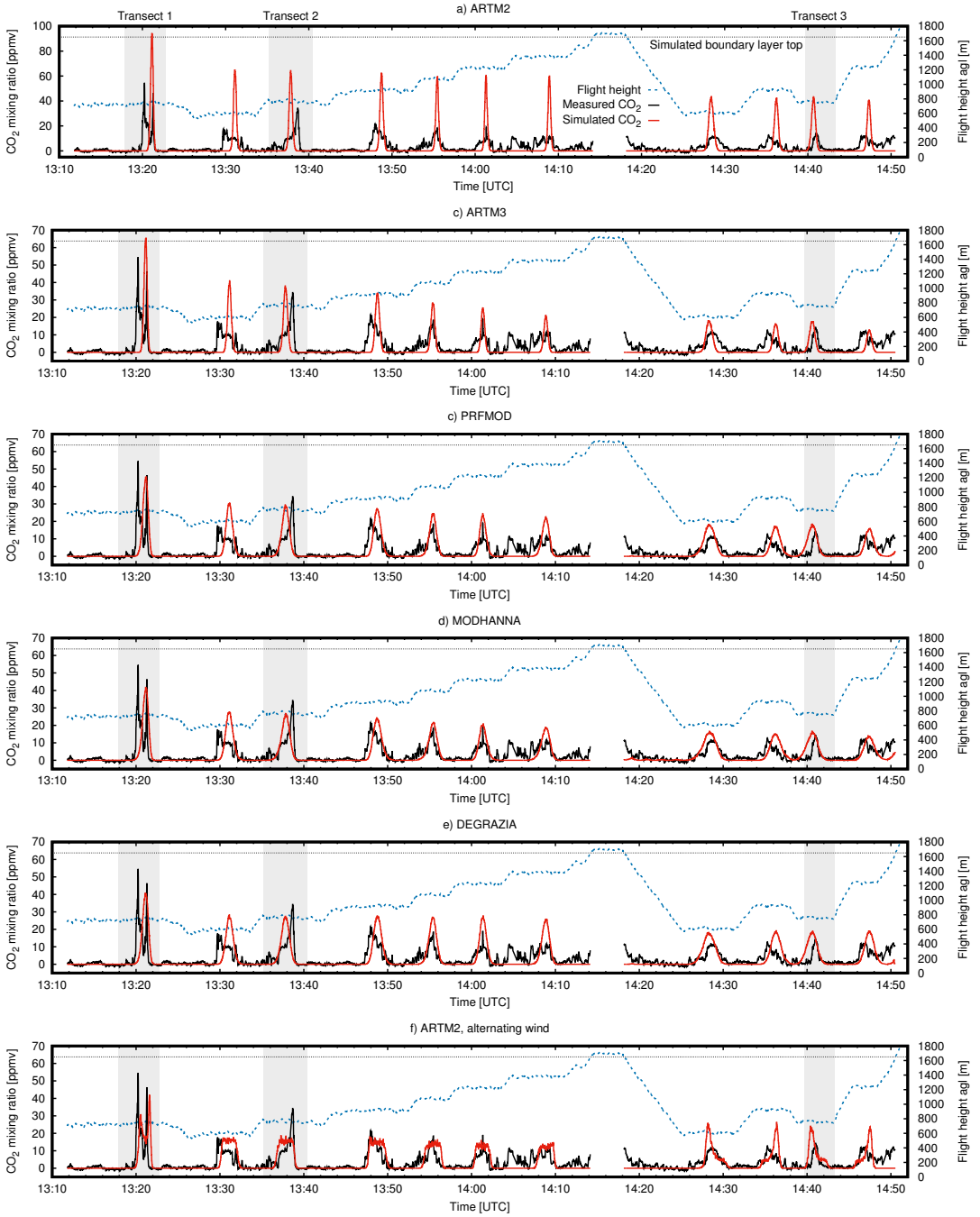

Figure 5.6: Simulated (red line) and measured (black line) CO_2 data along the flight path together with the flight height (blue dotted line) within the simulation domain. a) ARTM2, b) ARTM3, c) PRFMOD, d) MODHANNA, e) DEGRAZIA turbulence models and f) ARTM2 turbulence model with two alternating wind directions. The transects shown in Fig. 5.5 are shaded grey. From Hanfland et al. (2023).

and mimics the structure of two maximums at transect 1. However, these two observed maximums originate from snap-shots of the meandering plume and are not expected to be reproduced by the time-averaged simulation. Moreover, physically unrealistic plateaus of mixing ratios are simulated in wall 1 and a single narrow mixing ratio peak in wall 2, which is a result of the alternating wind directions. Mixing ratio maps of simulations and observations at selected heights from 550 m agl to 1 100 m agl are given in the Figs. 5.7 to 5.9, respectively.

Vertical dispersion

For the analysis of the vertical plume behaviour, the cross sections of the simulated plumes at wall 1 are presented in Fig. 5.10 at page 102. The narrowest simulated plume is obtained by the ARTM2 model and underestimates the width of the observed plume at heights from 600 m to 1 400 m agl. The plume of ARTM3 model is slightly wider throughout the PBL. In both, the ARTM3 and PRFMOD model, the values of σ_y ($T_{\mathrm{L}y}$) decrease (increase) with increasing height, respectively (see Fig. 4.8 on page 75). While these opposing trends cancel out each other for the ARTM3 model they lead to a slightly increase of lateral dispersion with height for the PRFMOD model. The vertical profiles of σ_y and $T_{\mathrm{L}y}$ of the MODHANNA model shown in Figs. 4.8 c) and d) appear to lead to a slightly increasing dispersion with increasing height, too. In contrast, σ_y and $T_{\mathrm{L}y}$ are not dependent from z in the DEGRAZIA model. Below 200 m the width of all five simulated plumes decrease towards the surface.

All TMs show a slightly decrease of the mixing ratio with increasing height at a constant distance from the source (see wall 1 and wall 2 in Fig. 5.6), which agrees with observations. From the cross sections at wall 1 (see Fig. 5.10) the average horizontal mixing ratio profiles are derived and shown in Fig. 5.11 at page 103. Except for the DEGRAZIA model, the decreasing mixing ratio with increasing height, above 600 m, can be recognised here as well. The average mixing ratio of the plume simulated from the DEGRAZIA model decreases only towards the very edge of the top of the simulated boundary layer. However, in Fig. 5.6 the highest maximum mixing ratios at wall 1 (13:25 UTC - 14:10 UTC) occur at transect 2 for the measurements. The simulations instead show very similar peaks at the two lowest transects in wall 1 having the highest concentration values.

In contrast to the Gaussian lateral mixing ratio distribution of the plume of Fig. 5.10 a, the ARTM2 turbulence model with two alternating wind directions (Fig. 5.10 f) shows the uniform mixing ratio distribution in the plume's core region (mixing ratio $>$ 1 ppmv) as it was already shown in Fig. 5.6 f.

Figure 5.12 at page 104 reveals that the cross sections of wall 2 show a similar behaviour of the plumes. The measured data show a large variation of the plume width on the different transects emphasising the meandering and turbulent char-

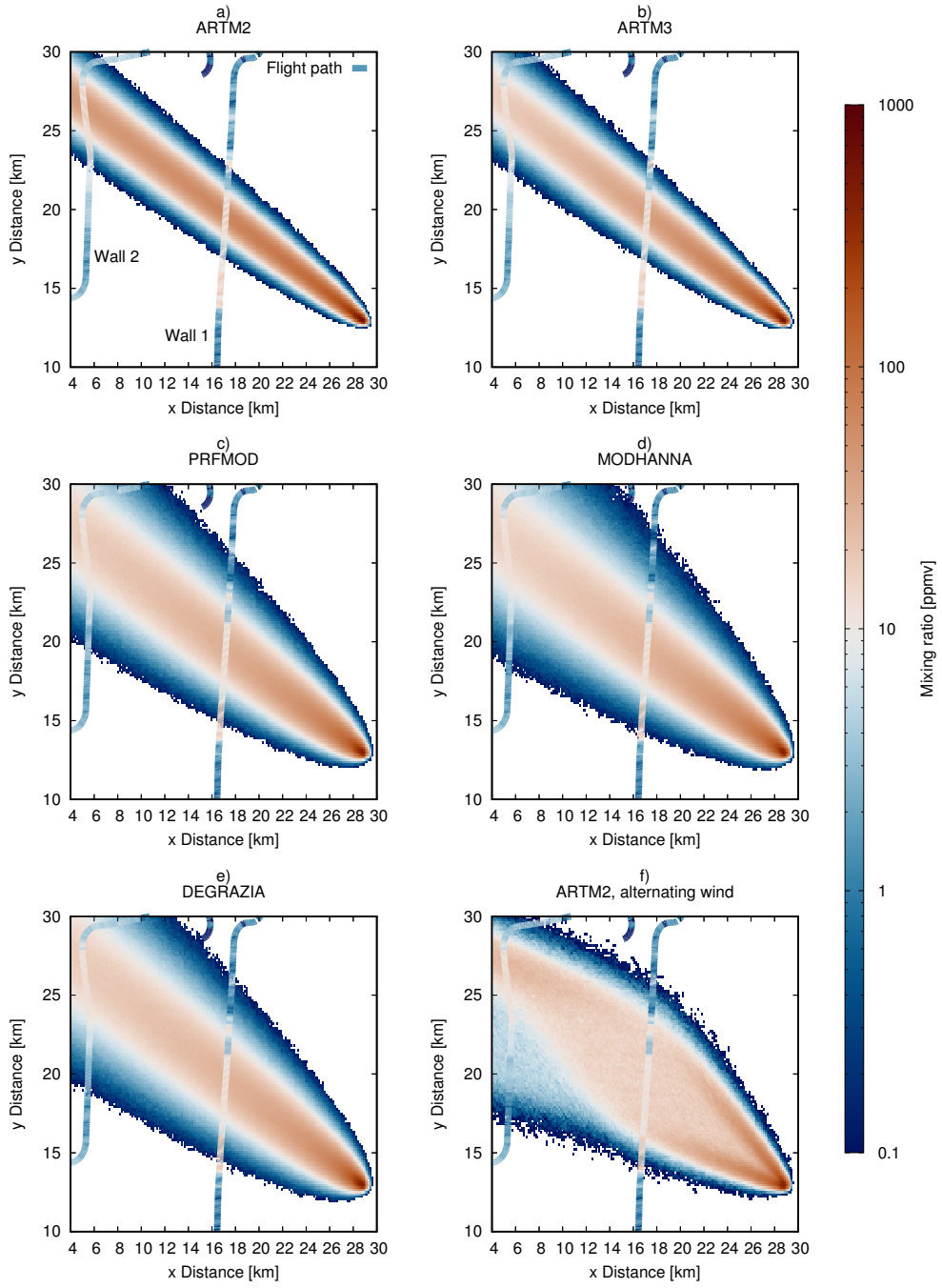

Figure 5.7: Comparison of the observed (550 m to 650 m agl) and the simulated CO_2 mixing ratio (600 m to 650 m agl). From Hanfland et al. (2023, Supplement).

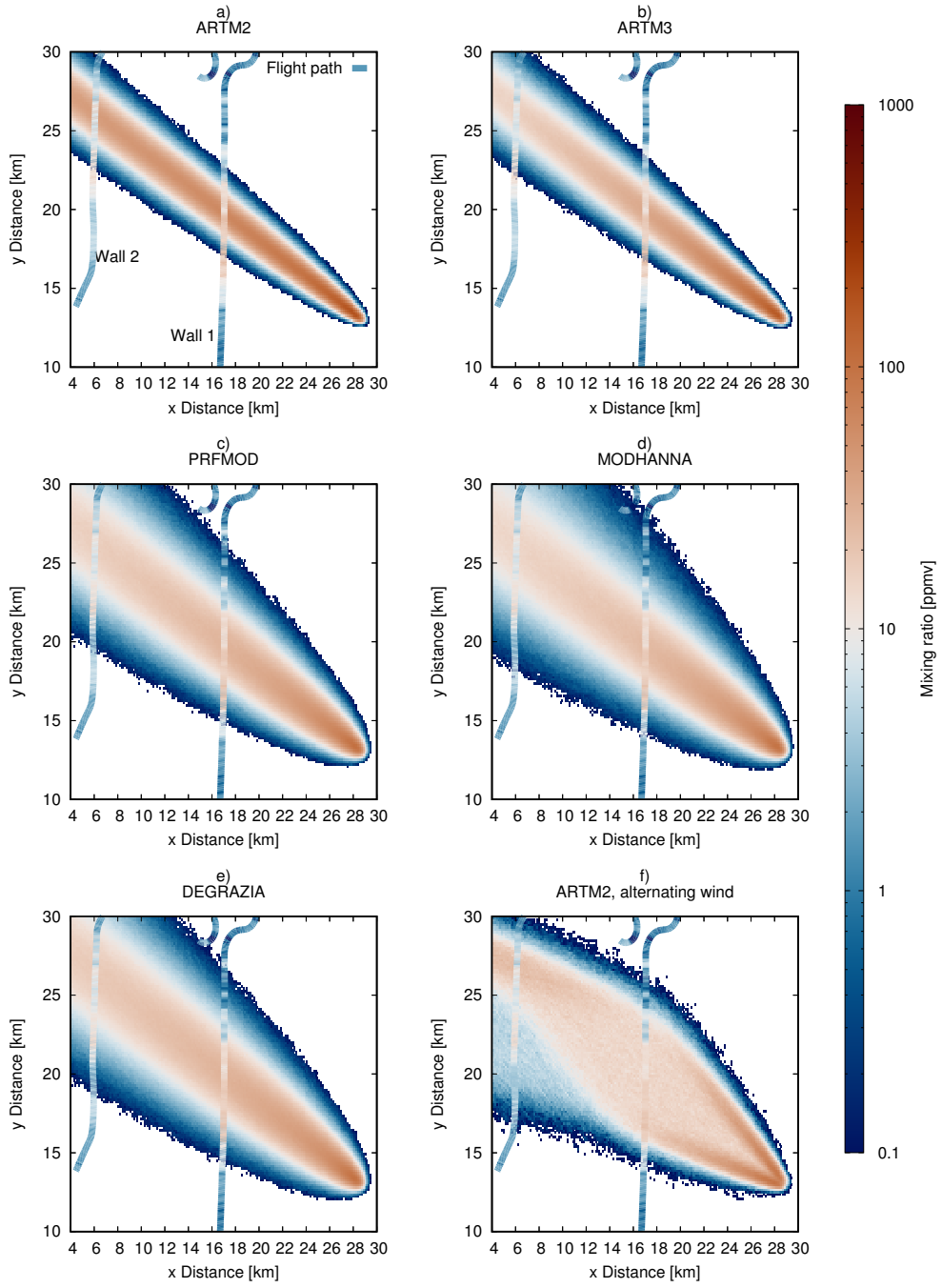

Figure 5.8: Comparison of the observed (850 m to 950 m agl) and the simulated CO_2 mixing ratio (900 m to 950 m agl). From Hanfland et al. (2023, Supplement).

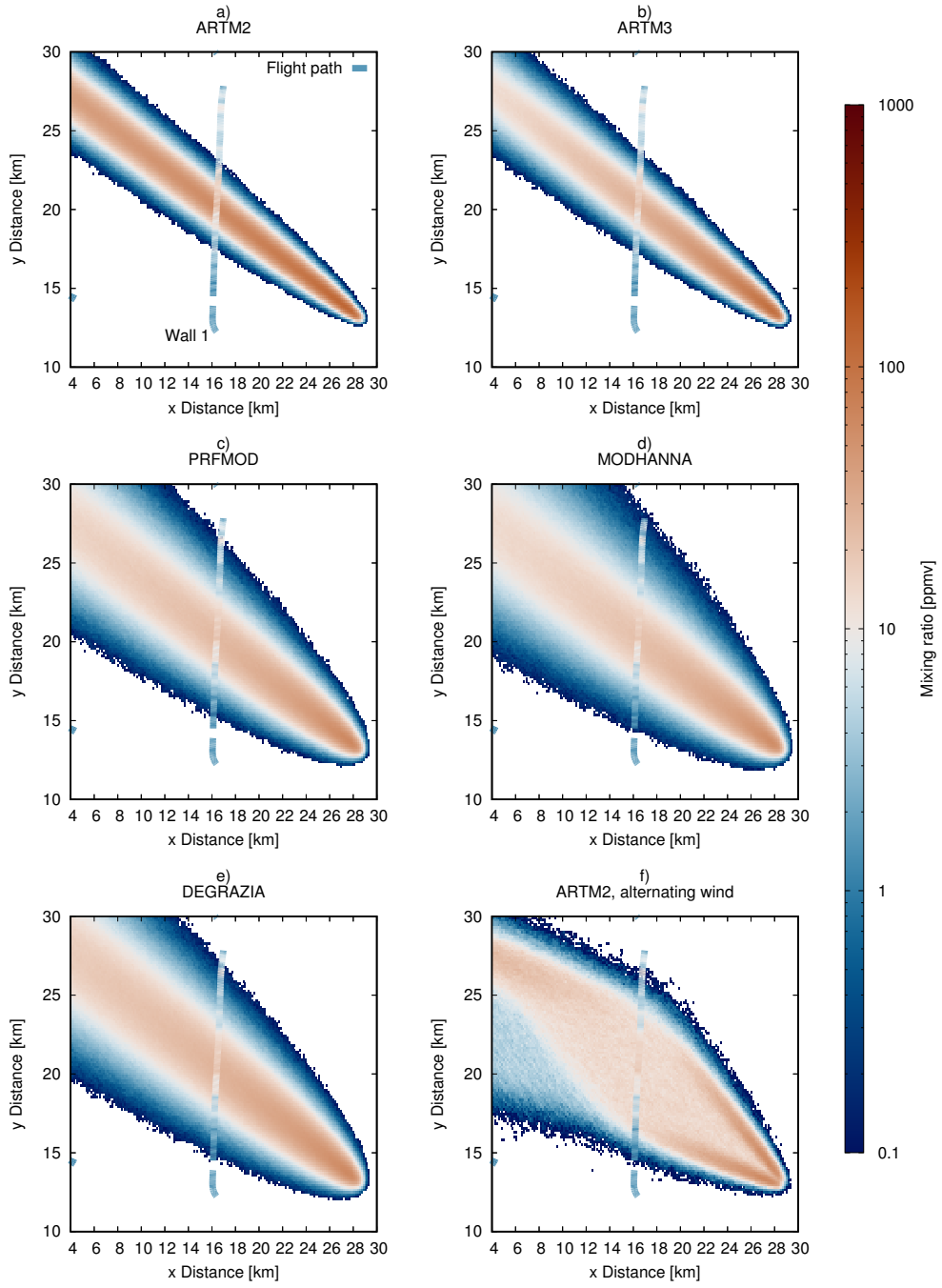

Figure 5.9: Comparison of the observed and the simulated CO_2 mixing ratio at the height of 1 050 m to 1 100 m agl. From Hanfland et al. (2023, Supplement).

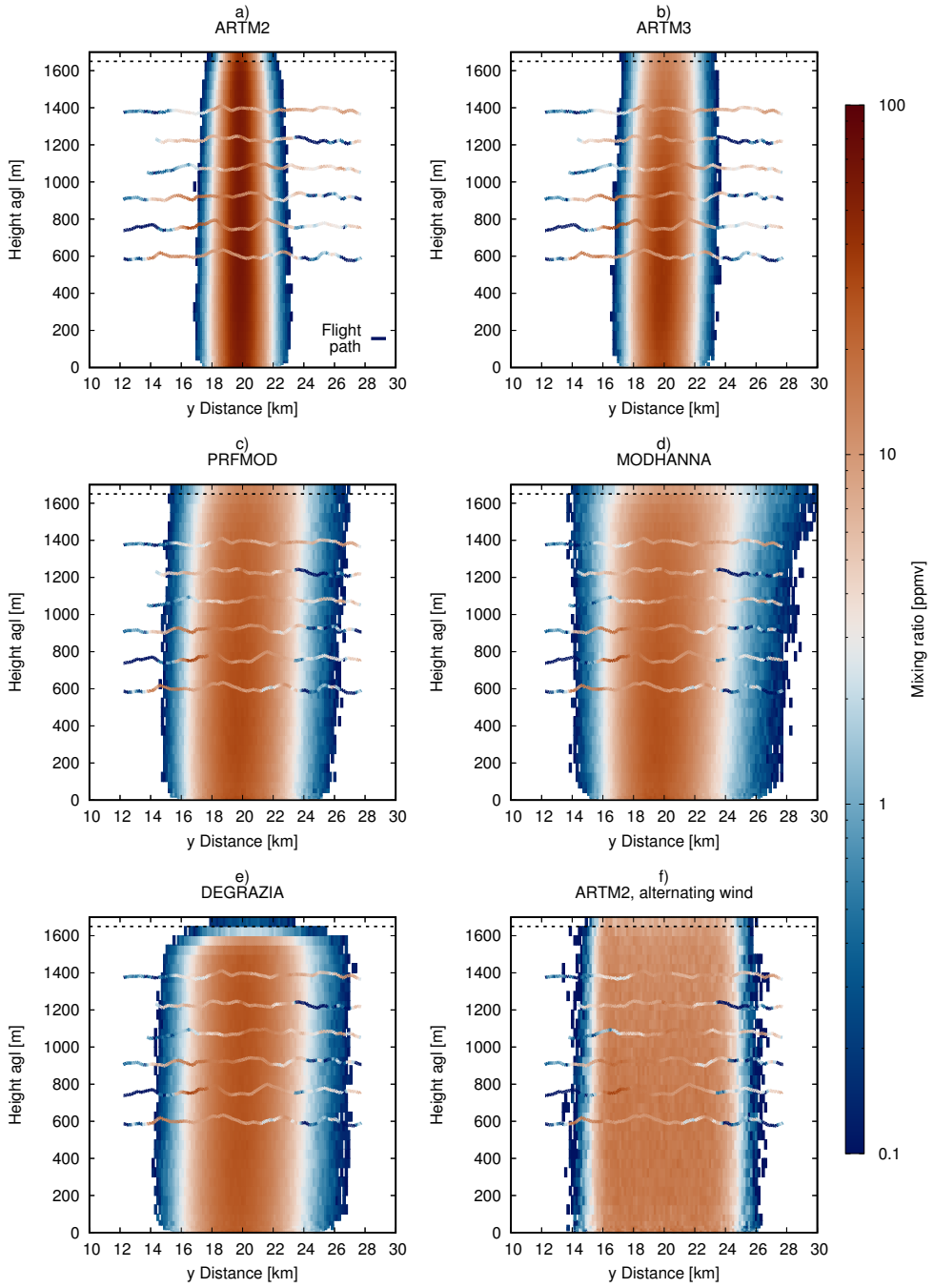

Figure 5.10: Cross section of the simulated plumes at wall 1 of the observations for the different TMs a) ARTM2, b) ARTM3, c)PRFMOD, d)MODHANNA and e) DEGRAZIA. f) the two wind directions case for ARTM2. The x-axis "y Distance" is in south-north orientation. The dashed line at 1 650 m agl marks the simulated mixing layer top. From Hanfland et al. (2023).

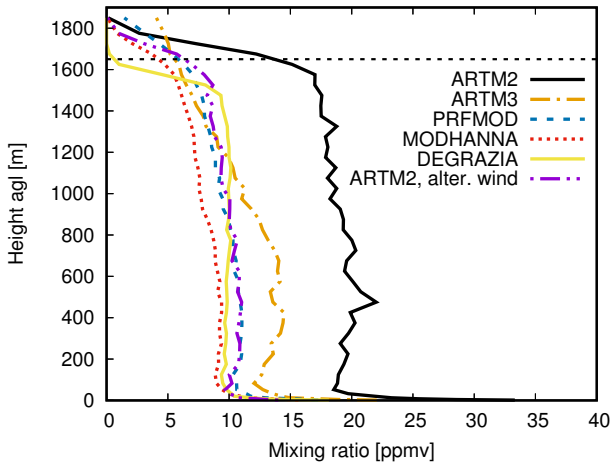

Figure 5.11: Profile of the average horizontal mixing ratio of the six simulation cases at wall 1 (see Fig. 5.10). The dashed line at 1 650 m agl marks the simulated mixing layer top. From Hanfland et al. (2023).

acter of the real plume. Furthermore, it can be recognised that the real plume is not entirely recorded; the transects are too short at wall 2.

Validation and uncertainty evaluation

In order to quantify the simulations uncertainty, I investigated the deviations of the simulated and the observed CO_2 mixing ratios in the plume by probability distributions (PDs), comparisons of integrated plume concentration and point-to-point mixing ratio comparisons.

The deviation of model results and measurements in a plume can be accessed by the comparison of the PDs and the cumulative probability distributions (CPDs) of simulated and observed CO_2 mixing ratios in the plume. This corresponds to the method described in the third criterion stated by De Visscher (2014) given at page 2. At this point it has to be mentioned that the third criterion is the only one that can be tested using the given data set because there are no data contained that would allow the calculation of average concentrations at one location over time. The PDs of simulation and measurement are normalised to the maximum mixing ratio of the measurements with the integrals of simulated and measured distributions being equal. To get rid of the mixing ratio fluctuation of the excess mixing ratio of the measurement, mixing ratio values below 1 ppmv are not taken into account. The PDs and CPDs of the five different TMs and the observations for all transects below the top of the simulated boundary layer are given in Fig. 5.13. The PDs of the simulated and measured plume show the occurrence of mixing ratio values relative to the maximum mixing ratio of the measurements. There is an

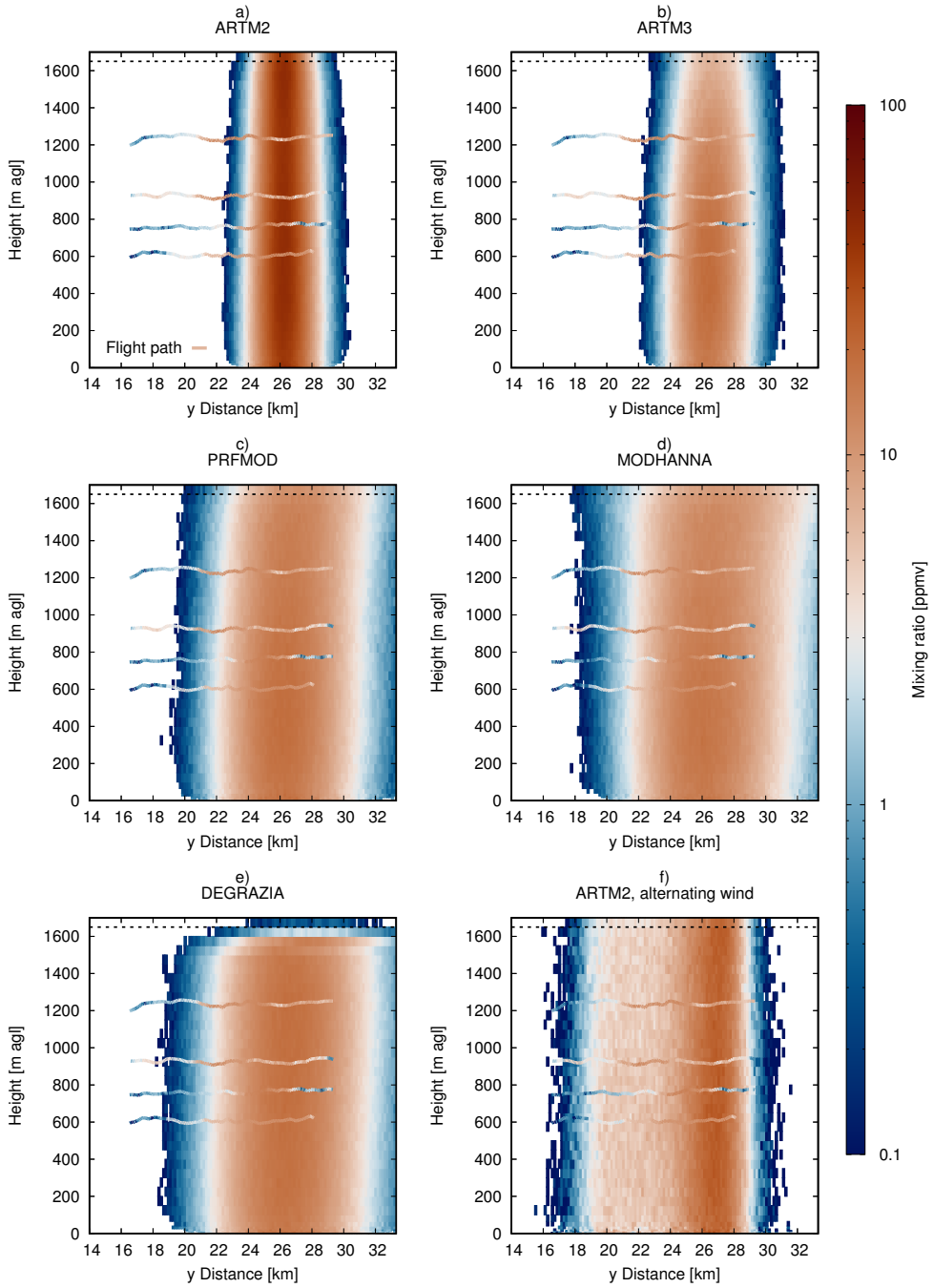

Figure 5.12: Cross section of wall 2 of the observed and simulated CO_2 plumes for the different turbulence models. The dotted line is the simulated PBL top. The right boarder of the graphs represent the northern simulation domain boarder. From Hanfland et al. (2023, Supplement).

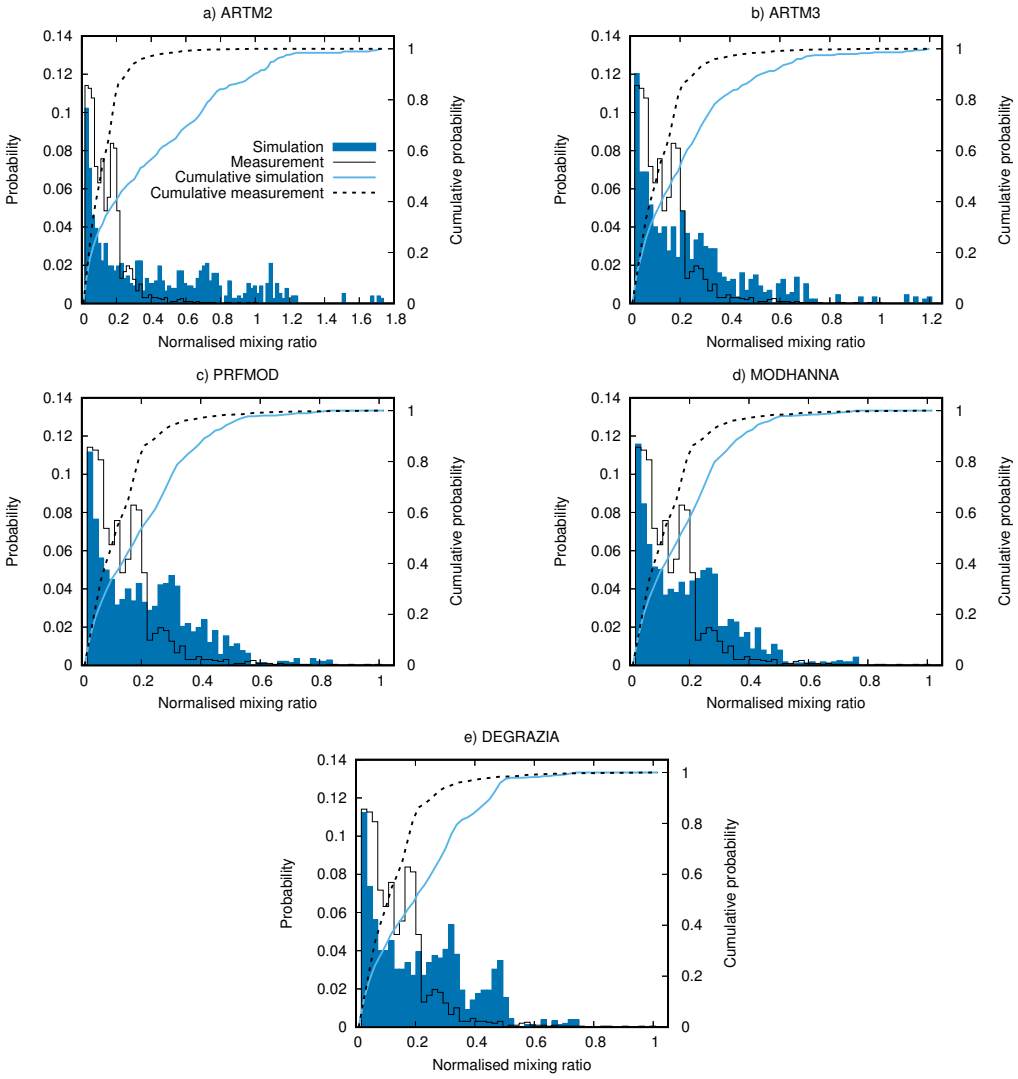

Figure 5.13: Probability distribution (bars) and cumulative probability distribution (lines) of simulated and measured mixing ratios of the five TMs. The PDs are normalised according to the maximum mixing ratio of the measurements and the integral of simulated and measured PDs are equal. Mixing ratio values below 1 ppmv are not considered in the PDs and CPDs. From Hanfland et al. (2023).

overestimation of simulated maximum mixing ratios for the ARTM2 and ARTM3 turbulence model. The high number of data points at approx. 20% of the maximum mixing ratio of the measurements is due to the fine structure, e.g. shoulders beside peaks and broad indistinct peaks of the plume not represented in the simulations. MODHANNA can be identified as the TM showing the best agreement with the observations concerning the PDs and CPDs, i.e. the occurrence of the mixing ratio values is most similar to those of the measurement. To quantify the similarity and to decide whether simulations and measurements are significantly different, three statistical tests were applied: the Z-test; the Kolmogorov-Smirnov (KS) test; and the Cramér-von Mises (CvM) test (Conover 1980; Wilks 2006; University of Oregon 2020). The Z statistic represents the distance between the means of two PDs normalised to the standard error. According to the following limits the Z statistic is interpreted as (University of Oregon 2020):

$$
\begin{aligned}
Z < 2.0 &\quad \text{two samples are the same;} \\
2.0 \leq Z < 2.5 &\quad \text{two samples are marginally different;} \\
2.5 \leq Z < 3.0 &\quad \text{two samples are significantly different;} \\
3.0 < Z &\quad \text{two samples are highly significantly different.}
\end{aligned}
$$

The KS statistic represents the supremum of the distance between two CPDs at the abscissa while the CvM statistic is proportional to the integral of the distances between two CPDs at the abscissa. For both I assumed a significance level of 0.05. The statistics and their p-values (in brackets) are summarised in Tab. 5.4. The three statistical tests show that all simulated mixing ratio distributions differ

Table 5.4: Z statistics, Kolmogorov-Smirnov (KS) statistics and Cramér-von Mises (CvM) statistics of the mixing ratio distributions of the five TMs. The p-values are given in brackets, respectively. The significance level is 0.05. From Hanfland et al. (2023).

Turbulence model	Z statistic	KS statistic	CvM statistic
ARTM2	16.8	0.45 (0.00)	25.1 (0.00)
ARTM3	11.5	0.23 (0.00)	12.8 (0.00)
PRFMOD	13.5	0.24 (0.00)	15.5 (0.00)
MODHANNA	10.2	0.20 (0.00)	9.8 (0.00)
DEGRAZIA	15.5	0.27 (0.00)	19.8 (0.00)

significantly from the observed one. Nevertheless, the statistics can be used to rank the models. MODHANNA shows the best agreement with the observations i.e. the distribution of mixing ratio values in the transects is most similar to those of the observations compared to the other TMs. The statistical tests rank ARTM3 second

but this may be biased by the statistical tests being very sensitive to deviations in the regions of the PDs with high numbers of low mixing ratio values. I want to point out that the results do not mean that the MODHANNA model produces mixing ratio peaks that are structured like the observed ones but the relative occurrence of mixing ratio values is most similar.

To compare the simulation results, the integral of the mixing ratio values along the flight path below the simulated boundary layer top (see Fig. 5.6) within the plume is shown in Tab. 5.5. I used the method mentioned above to get rid of the baseline fluctuations of the excess mixing ratios to calculate the integrals. This procedure is also applied to the simulations. Except for ARTM3, there is a good agreement between the modelled and the measured data: the deviation is less than 13%. Concerning ARTM3, there is a strong vertical gradient in the simulated mixing ratios of the plume above 700 m as it is illustrated in the Figs. 5.10 b and 5.11. Tracers are stronger diluted (accumulated) in the upper (lower) half of the PBL than for other TMs. This corresponds to the findings of Sec. 4.2. Since the flight path is mainly located in the upper half of the PBL, the integral along the flight path results in a lower value for ARTM3. The higher mixing

Table 5.5: Integrals of mixing ratio values (values below 1 ppmv are not considered) along the flight path for simulations A_{sim} and observations A_{obs} within the simulated PBL (see Fig. 5.6) given in ppmv × km as well as their ratio. From Hanfland et al. (2023).

Turbulence model	A_{obs}	A_{sim}	$A_{\text{sim}}\,A_{\text{obs}}^{-1}$
ARTM2	1 094	1 186	108.4%
ARTM3	1 094	742	67.8%
PRFMOD	1 094	1 194	109.2%
MODHANNA	1 094	1 114	101.8%
DEGRAZIA	1 094	1 236	112.9%

ratios in the lower half of the PBL might become important when simulations are used for radiation exposure assessment. The results suggest, that the original assumption of the emission rate may not deviate much from the actual value. However, observations below 600 m would be necessary to get a more complete comparison of simulated and actual plume.

The deviation between simulations of the five TMs and observation at a specific position can be assessed using density scatter-plots as given in Fig. 5.14. All mixing ratio values larger than 1 ppmv along the flight path below the top of the simulated boundary layer are considered. As a guide to the eye the regression with slope $m = 1$ is given as a dashed line and represents the equality of simulated and observed mixing ratios. The deviation from this equality by the factor two or less

is confined by the red dashed dotted lines. It is not expected to find a lot of data points at the regression $m = 1$ due to the fundamental differences of the data set properties of simulation and observation. However, a large amount of data points

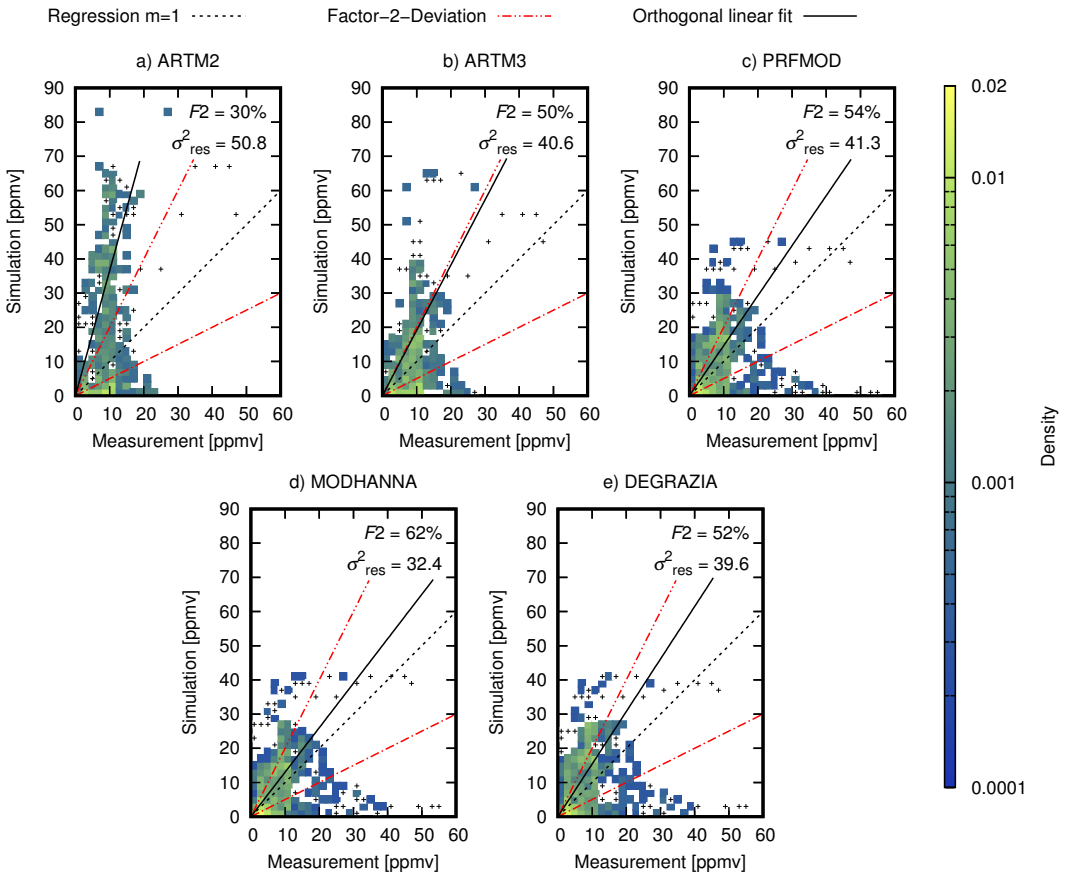

Figure 5.14: Density scatter-plots of the simulated mixing ratios of the five TMs a) ARTM2, b) ARTM3, c) PRFMOD, d) MODHANNA and e) DEGRAZIA against the observations. Single data points in a bin are indicated with (+), multiple data points in a bin are colour coded. The regression with slope $m = 1$ (dotted black line) represents the identity of simulation with measurement, the dotted dashed red line represents a deviation from the regression with $m = 1$ by a factor two and the solid black line represents the orthogonal linear fit to the data points. $F2$ gives the percentage of data points with deviations of not more than a factor two from the regression $m = 1$. The residual variance of the orthogonal fit is given by σ^2_{res}. From Hanfland et al. (2023).

within a deviation of a factor two decreases the uncertainty. The percentage of data points within these boarders is represented as $F2$ given in Fig. 5.14. Low $F2$ values can also be explained by the large number of measurement data points outside the simulated plume because it is too narrow. The smallest $F2$ is derived for the ARTM2 model. This coincide with the unbalanced distribution of the

data points around the regression $m = 1$ with the simulation overestimating the observed mixing ratios and simultaneously simulating too narrow plumes. This is represented by the orthogonal regression of data points (black line) given in the figure with a slope above three. The residual variance σ^2_{res} quantifies the scattering of data points. The large value for ARTM2 indicates a less compact data point distribution. ARTM3 shows a more balanced and compacter data but still distinctly overestimates mixing ratios and underestimates the plume width. PRFMOD, MODHANNA and DEGRAZIA show similar properties with $F2 > 50\,\%$, compacter, well balanced data and less overestimated mixing ratios and less underestimated plume widths, with the MODHANNA model performed slightly best for the given measurement and turbulence conditions.

The uncertainty of the CO_2 measurement device of $\pm 0.15\,\text{ppmv}$ is at least one order of magnitude smaller than the measured enhanced CO_2 concentrations. Thus, the measurement uncertainty has only a minor impact on the evaluation results.

5.2 Comparison of ARTM to five other atmospheric transport models

ARTM was also compared to five other atmospheric transport models and to measurements at a different site. Brunner et al. (2023) intercompared five Eulerian models and included ARTM as the only LPDM. Two of them, COSMO-GHG (Consortium for Small-scale Modeling-Greenhouse Gas) (Brunner et al. 2019; Jähn et al. 2020) and WRF-GHG (Weather Research and Forecasting-Greenhouse Gas) (Ahmadov et al. 2007; Beck et al. 2011), are meso-scale non-hydrostatic NWP models extended with the capability of modelling the emission, transport of greenhouse gases and atmosphere-biosphere exchange fluxes. Three models, WRF-LES (Weather Research and Forecasting-Large-Eddy Simulation) (Wolff et al. 2021), ICON-LEM (ICOsahedral Non-hydrostatic Large-Eddy Model) (Kern et al. 2016) and EULAG (Eulerian/semi-Lagrangian fluid solver) (Prusa et al. 2008) are LES models.

The overall aims of the intercomparison were: i) the evaluation of the model simulations against in situ and remote sensing measurements of two test cases; ii) the analysis of spatio-temporal variability and dispersion of the plumes of the different models with their individual range of resolution to derive recommendations for model setups; iii) the analysis of the quantification of CO_2 emissions for the future Copernicus Anthropogenic Carbon Dioxide Monitoring (CO2M) satellite observations using the cross-sectional flux (X-flux) method and the integrated mass enhancement (IME) method; and iv) to provide recommendations for fu-

ture measurement campaigns to support the validation of atmospheric simulation models and satellite observations.

According to the modelling protocol the participating research groups provided simulation results of their models in a blind intercomparison study. I conducted ARTM simulations and provided simulation results for two power plants. Furthermore, I provided a technical description of the model ARTM to the study by Brunner et al. (2023).

5.2.1 Observational data and modelling protocol

The observational data consists of exhaust CO_2 plumes of the two lignite power plants Jänschwalde and Bełchatów. All measurement data originate from the CoMet 1.0 campaign. The Jänschwalde data was collected on 23 May 2018 by two aircraft, the DLR HALO and the FUB Cessna, equipped with in situ and remote sensing instruments. Both flew at constant heights above the PBL and measured column mean dry air mixing ratios of CO_2 (XCO_2) with the CHARM-F lidar and the MAMAP spectrometer, respectively (Gerilowski et al. 2011; Krautwurst et al. 2021). The FUB Cessna also flew several transects in the PBL at a fixed distance from the source at different heights to measure in situ CO_2 mixing ratios with a Los Gatos Research greenhouse gas analyser. The measurements at the Bełchatów power plant were performed on 7 June 2018. Additional to the in situ data described in Sec. 5.1.1, CO_2 column concentrations from the two aircraft equipped with remote sensing instruments were measured.

The modelling protocol defined mandatory and optional input parameters such as the size of the simulation domains, the horizontal and vertical source positions, emission rates and simulation periods. In the modelling protocol the participants agreed to a minimum set of three passive CO_2 tracer simulations for each power plant. The simulation results were compared on a simulation domain of approx. 60 km × 60 km with a resolution of 200 m. ARTM was only able to simulate such a large domain with a coarser resolution of 290 m. The vertical resolution was not prescribed and was selected individually by the research groups. Optionally, a second, larger simulation domain with coarser grid resolution was simulated depending on the models' capabilities. The simulations had to cover at least the day of the measurement flight and the previous day. For the three mandatory simulation scenarios, different configurations of emission were chosen. In the low emission scenario, emissions were released at the height of the stacks without any plume rise. In the medium emission scenario, vertical emission profiles were calculated representing the plume rise considering stack height, flue gas temperature, volume flow and meteorological conditions taken from hourly COSMO-7 analysis of MeteoSwiss (Brunner et al. 2019). The high emission scenario was similar to the medium one but the highest plume rise profile of the day of the flight and the

previous day was selected for the entire simulation period. The research groups simulated with constant emission rates that correspond to the annual average CO_2 emissions reported to the E-PRTR, respectively. Since actual emission rates at the time of the measurement flights were different, Brunner et al. (2023) estimated the emissions by comparing the annual reported emission rates to the produced electrical power and rescaled the concentration fields afterwards. The concentration fields for Jänschwalde were rescaled by 128% and those for Bełchatów by 123% in order to represent the estimated CO_2 emissions during the measurements. The model output was reported on a prescribed latitude-longitude grid to make model comparisons easier.

5.2.2 ARTM simulations

For the simulations, ARTM 3.0.0 was used with the default turbulence model of ARTM 2.8.0 (VDI 3783 part 8 2002; Hanfland et al. 2022). In contrast to previous versions, it is possible in ARTM 3.0.0 to enter the mixing layer height manually instead of using a predefined value. Mixing layer heights were derived from the meteorological data and from the measurements. The meteorological input data originates from Consortium for Small-scale Modeling-Greenhouse Gas (COSMO-GHG) simulations provided by Stephan Henne from the Swiss Federal Laboratories for Material Science and Technology (Empa). For both power plants the provided meteorology was used except for the time of the measurement flight for the Bełchatów power plant, where in situ measurements of the DLR Cessna were used as described in Sec. 5.1.2 to derive wind direction, wind speed and SC data. It turned out that the boundary layer model of ARTM generated too narrow plumes at very unstable atmospheric conditions at the Belchatów power plant. Thus, the two wind directions derived from the measurements (see Sec. 5.1.2) were used alternatingly (14:00 UTC to 15:00 UTC) to cover the turbulence scales that are not covered by the turbulence parametrisation. For the Jänschwalde power plant only the meteorology from COSMO-GHG was applied.

5.2.3 Model performance assessment

For the simulation comparison statistical properties such as the plume width and the concentration amplitude are selected rather than a point-to-point comparison. Therefore, Brunner et al. (2023) fitted a Gaussian distribution to the CO_2 data of the individual transects. The background was subtracted from the in situ data while the XCO_2 data was already provided as excess CO_2 concentrations. The fit parameters of the Gaussians A (area integral), σ (standard deviation/width) and μ (plume position shift) are fitted using a non-linear least squares Levenberg-Marquardt minimisation method. Since the transects are not perfectly perpendic-

ular to the plume axis, a geometric correction factor cf is applied to estimate the real plume width $\sigma \cdot cf$. The maximum of a Gaussian curve is called the amplitude and represents the maximum plume concentration of the transect, respectively. The amplitude of the XCO_2 concentrations are converted to ppm to make them comparable with in situ concentrations and simulations.

5.2.4 Results and discussion

Qualitative comparison of simulations and observations

Concentration maps showing the simulated total XCO_2 are used for the intercomparison. For the comparison with the observations, four-dimensional CO_2 walls of the simulations as well as CO_2 timelines of the simulations along the flight path are compared with the in situ data of both power plants. For Bełchatów, curtains of the simulated potential temperatures are compared with the measurements. For Jänschwalde the potential temperature was not measured. Additionally, XCO_2 timelines of simulations and observations from the MAMAP spectrometer and the CHARM-F lidar are compared for Bełchatów and Jänschwalde.

All models show a development of the turbulence in the atmosphere with narrow plumes in the morning and wider plumes around noon. For ARTM, this development is less prominent than for other models but the day time plumes are much wider than at night time. All the models agree with simulating the atmosphere of the Jänschwalde case being less turbulent than the atmosphere for the Bełchatów case.

Comparisons of the simulated potential temperature curtains reveal that the mixing layer depth varies for the different models. Two models, Weather Research and Forecasting-Greenhouse Gas (WRF-GHG) and ICOsahedral Non-hydrostatic Large-Eddy Model (ICON-LEM), showed almost perfectly neutral profiles of the potential temperature and thus simulated insufficiently turbulent boundary layers for the Bełchatów case. Since ARTM does not use the potential temperature to constrain turbulent mixing it is excluded from this investigation.

The comparisons of the simulated and observed CO_2 concentrations along the flight paths show that all simulations deviate from the measurements, which is expected. However, high resolution simulations are in better agreement with the observations than their low resolution counterparts.

Deviations between simulated and observed XCO_2 are smaller because XCO_2 over the entire PBL is less sensitive to the exact vertical CO_2 distribution and to weaknesses in the vertical turbulent mixing.

Statistical evaluation of plume properties

The statistical evaluation of the plume width, amplitude and integral area of the Bełchatów case reveals that the width (amplitude) in general increase (decreases) with increasing distance from the source. The high-resolution models, including ARTM, tend to underestimate the plume width in the near-field (up to 8 km from the source). This might be caused by the horizontal spread during the plume rise that is not considered in the simulations or by the usage of one single source instead of two with a distance of 350 m from each other. The amplitudes seem to be more robust than the width as the amplitude shows less variations between the models. In the near field, the dispersion is stronger for the models with coarser resolution leading to comparatively wide plumes with low amplitudes. High-resolution models, conversely, overestimate the amplitudes in the near-field which corresponds to the narrow widths. At large distances from the source, the simulated amplitudes are more consistent with observations.

For Jänschwalde, the plumes are more compact due to less turbulence and larger wind speeds. The evolution of the plume width is quite consistent with Gaussian plume evolution but coarse resolution models overestimate the width in the near-field. ARTM is in good agreement with observations without mimicking additional turbulent motion by using alternating wind directions as it was used for the Bełchatów case. For Jänschwalde, the atmosphere is less turbulent than for Bełchatów. The plume width simulated by ARTM shows good agreement with the observations. Compared to the earlier findings, this result reveals that the lack of the turbulence model of ARTM 2.8.0 modelling too weak dispersion occurs not under all atmospheric stratifications. The area integrals of the fitted Gaussians of simulations and observations are consistent for both power plants. A summary of the statistical parameters is given in Fig. 5.15. Details about strengths and weaknesses of specific models are given by Brunner et al. (2023).

Emission quantification of synthetic satellite measurements

In order to assess the credibility of satellite missions that monitor the CO_2 emissions of point sources such as the CO2M mission, synthetic (i.e. simulated) emission plumes are used and evaluated. The simulations of the different models are used for the Bełchatów case to produce synthetic satellite images of the emission plume assuming that the simulations provide realistic plumes. Diurnal variations of the PBL and measurement noise are included to give a more comprehensive analysis. Two different Gaussian noise scenarios, low- (0.5 ppm) and high-noise (1.0 ppm), are evaluated using the cross-sectional flux (X-flux) and the integrated mass enhancement (IME) methods. The resolution of the simulated noisy plume data is reduced to 2 km $\times$ 2 km pixels to mimic the resolution of the CO2M satellite (Sierk

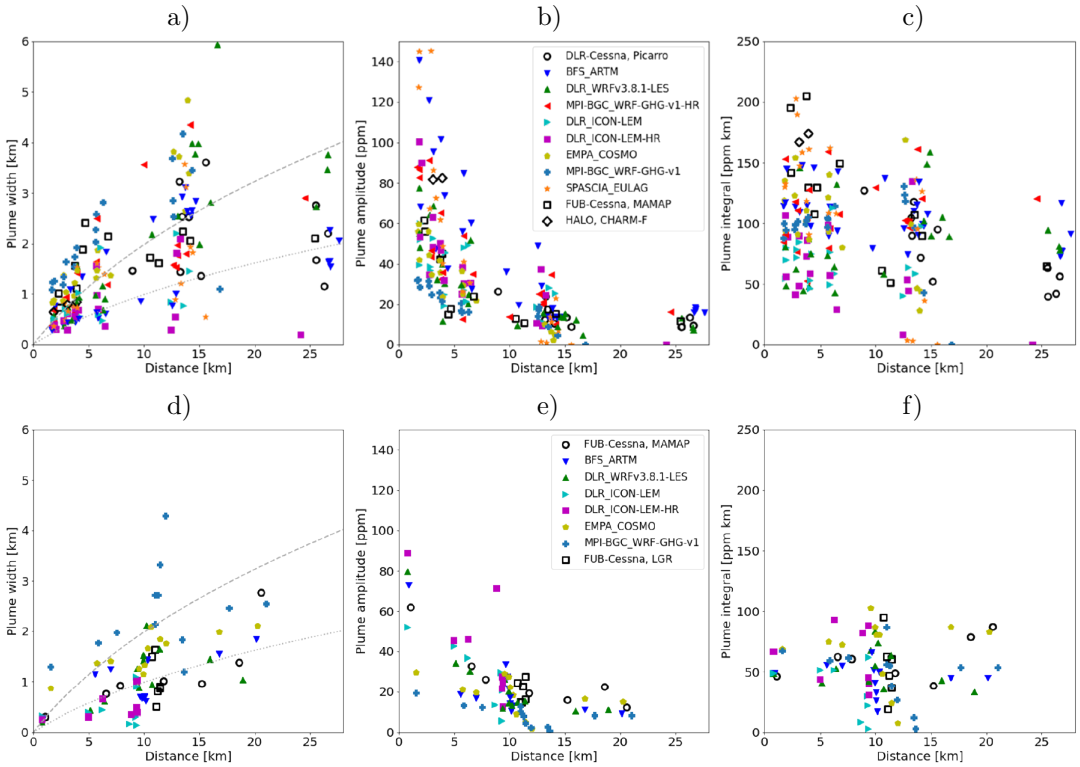

Figure 5.15: Comparison of statistical characteristics of simulated and observed CO_2 plumes as a function of the distance from the source. a), b), and c) show the plume width ($\sigma \cdot cf$), the plume amplitude (maximum of the fitted Gaussian) and the plume integral area A of the Bełchatów power plant on 7 June 2018. d), e) and f) show those for the Jänaschwalde power plant on 23 May 2018. The observations are shown as black empty symbols. The grey dotted and dashed lines represent the plume width of an analytical Gaussian plume model for weakly and highly unstable conditions, respectively (Briggs 1973). From Brunner et al. (2023).

et al. 2021).

The X-flux method integrates total column CO_2 in $\mathrm{kg\,m^{-2}}$ along a cross-section approximately perpendicular to the plume axis and calculates the emission as the product of this line density in $\mathrm{kg\,m^{-1}}$ with an effective wind speed parallel to the plume axis. The IME, i.e. the total mass of the CO_2 plume, is determined from all pixels above a predefined threshold. The emission is then calculated as

$$Q = \frac{U_{\mathrm{eff}}}{l_{\mathrm{c}}} IME \tag{5.1}$$

with the effective wind speed U_{eff} and the characteristic length l_{c} (Varon et al. 2018).

Figure 5.16 shows the results of the different models for both noise scenarios and both emission estimation methods. The strong vertical mixing at daytime reduces the scatter while at night the exact location of the derivation of the effective wind speed becomes a serious source of uncertainty. The midday-average (9:00 UTC to 15:00 UTC) reveals that uncertainties of $10\% - 20\%$ originating from turbulent fluctuations have to be expected from the satellite measurements. More details about the presented findings of this section are given by Brunner et al. (2023).

The present results in the context to the earlier findings

The findings of the comparisons of ARTM 2.8.0 simulation results with the results of other transport models, airborne in situ and remote sensing measurements and the usage of the simulation results for the estimation of emissions are in agreement with the findings of the sensitivity analysis and the validation presented in Sec. 5.1. ARTM 2.8.0 simulates dispersion plume concentrations in agreement with the airborne in situ and remote sensing measurements as well as with the simulated plume concentrations of the other transport models under very unstable and less unstable atmospheric stratifications. However, both investigations revealed the tendency of the default TM of ARTM 2.8.0 to simulate too narrow plumes compared to observations and the other transport models under very unstable stratification. For less unstable stratification, the TM of ARTM 2.8.0 simulates plume widths in agreement with observations and other transport models. This indicates that the turbulence formulation used in ARTM 2.8.0 underestimates the turbulent diffusion and the turbulent kinetic energy under very unstable atmospheric conditions. In the TM the difference of the Obukhov length is not sufficient to simulate appropriate turbulent diffusion. Other TM as presented earlier in this work might be promising.

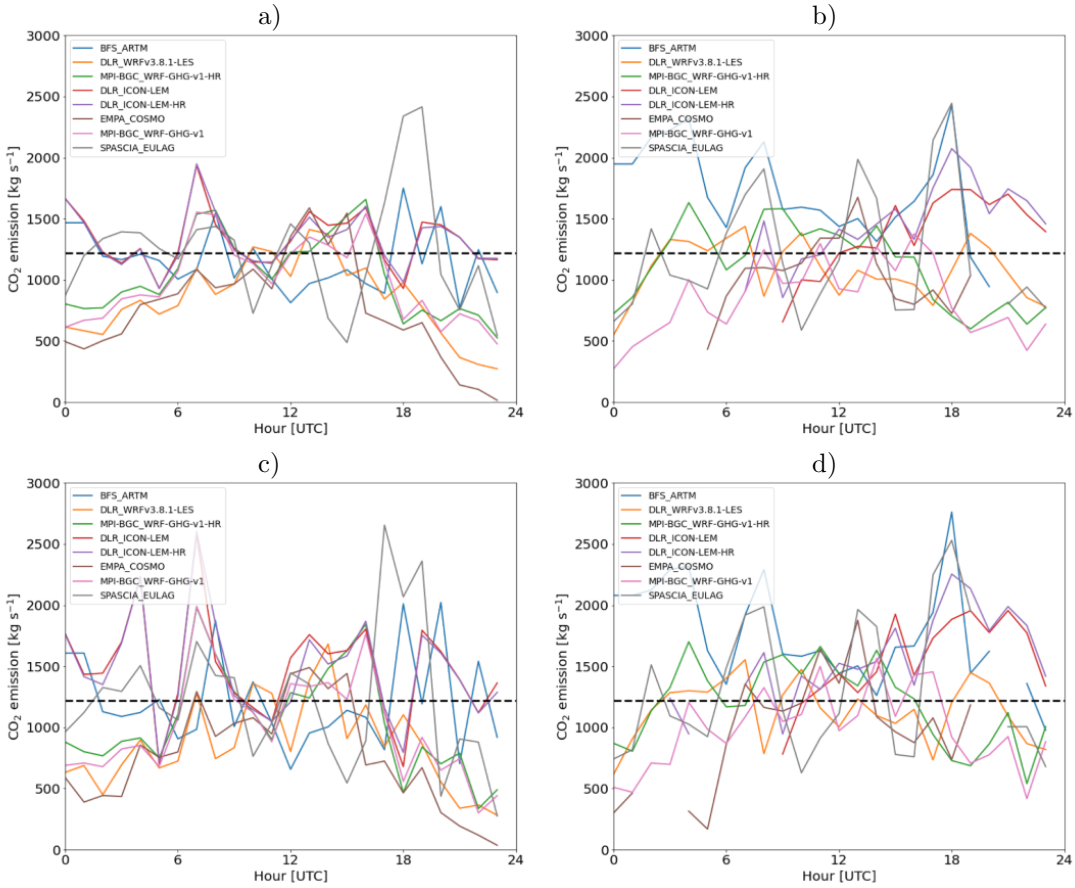

Figure 5.16: Quantified emissions of the synthetic CO_2 emissions of Bełchatów for all hours of 7 June 2018. a) and c) show the X-flux method; b) and d) show the IME method; a) and b) show the low-noise scenario (0.5 ppm); c) and d) show the high-noise scenario (1.0 ppm). The dashed line represents the true emission. From Brunner et al. (2023).

Chapter 6

Summary

This thesis contributes to the understanding of sub-grid turbulent motion of wind in the planetary boundary layer and its parametrisation in Lagrangian particle dispersion models. More specifically, I used a meso-γ-scale Lagrangian transport model in order to analyse the three-dimensional dispersion characteristics of tracers in a highly turbulent flow. As the Atmospheric Radionuclide Transport Model (ARTM) model, developed by Gesellschaft für Anlagen- und Reaktorsicherheit gGmbH (GRS), had not been presented in peer-reviewed literature yet, my first publication aimed at filling this gap by providing a comprehensive overview of the physical foundations and mathematical formulations of ARTM (Hanfland et al. 2022).

In order to provide guidance for the application of the model and for further model improvements, detailed sensitivity analysis and model evaluations were performed. Several different local and global sensitivity analysis methods were used to identify the dependencies of simulation results on input parameter variations in a structured way. Sensitivity analyses allow to estimate the influence of uncertainties of input parameters to the uncertainty of the simulation results. This information helps to identify input parameters, which have to be determined with special accuracy, e.g. by accurate measurements. An initial, more qualitative study on the dispersion characteristics of simulation results for gaseous and particulate matter tracers gave insights into the model's response to input parameter changes. I then performed a more detailed and more quantitative analysis where the dependencies of two output characteristics (target quantities) on input parameters were quantified and ranked. The two selected characteristics are the plume volume and the distance between source and the location of maximum concentration at the surface, which together comprehensively describe the three-dimensional structure of the dispersion of gas plumes. It could be shown that the stability class is in general the most influential input parameter followed by the roughness length, the source height and the zero-plane displacement height factor. However, this

ranking changes depending on the result characteristic. For the plume volume, the ranking from more to less important is stability class, roughness length z_0, zero-plane displacement height factor d and source height h_s while it is stability class, source height h_s, roughness length z_0 and zero-plane displacement factor d for the distance between source and the location of maximum concentration at the surface. This emphasises the importance of investigating not only a single output characteristic as done in previous studies. Furthermore, the influence of input parameters changes depending on the height. Although the roughness length has a larger influence on the plume volume than the zero-plane displacement factor, it is the opposite when considering only the volume in the three lowest layers (up to 10 m height). There are also cross-interactions between several input parameters possible that complicate the interpretation of model dependence. The uncertainty in the results depend most strongly on the uncertainties of those input parameters, which have the strongest influence on the target quantities. This is especially true for the input parameter stability class, which is a discrete quantity with only six classes. Thus, it is important that the input parameters are determined as precisely as possible to minimise simulation result uncertainties. The analysis revealed that there are large gaps in the continuous space of plume volume that originate from the usage of only six stability classes as turbulence parameters. This potentially causes uncertainties of about 15% in terms of plume volume and consequently in terms of concentration. The overestimation or underestimation of the plume width has a strong influence on the concentration uncertainty at the plume boarders. On the one hand, an overestimation of the simulates plume width results in concentration values at locations, where none is observed. On the other hand, an underestimation of the simulated plume width results in the absence of concentration values at locations, where the actual plume is observed. The usage of measured Obukhov lengths significantly reduces this uncertainty because it parametrises the turbulence with higher resolution.

The dispersion in a model like ARTM is critically determined by the formulation of turbulence, i.e. by the selected turbulence model. For the analysis of the turbulent motion and dispersion simulated by ARTM, five different turbulence models were studied under unstable stratification. Three turbulence models, ARTM2, PRFMOD and ARTM3, were already included in the ARTM 3.0.0 while two turbulence models, MODHANNA and DEGRAZIA, were additionally implemented in the framework of this thesis. The five turbulence models were first tested with respect to how well they preserve an initially well-mixed planetary boundary layer, or whether they tend to accumulate or deplete mass at certain altitudes in an unphysical way. Applying this well-mixed condition test under unstable atmospheric conditions revealed that all turbulence models had a tendency of unmixing, but to a variable extent. Except for the ARTM3 turbulence model,

all models stayed well below 6% deviation for heights up to 80% of the mixing layer depth ($z \leq 0.8\,h_{\mathrm{m}}$). ARTM3, instead, showed up to 18% deviations from the uniform distribution. In contrast to this, it performed best at the ground level showing only marginal deviations. The DEGRAZIA model showed a small and the most homogeneous deviation from the uniform distribution below $z \leq 0.8\,h_{\mathrm{m}}$. For all turbulence models, the deviations increased within the first two simulation hours but stayed constant afterwards. Given the rather small deviations from an ideal behaviour, all turbulence models can be used for the purpose of exposure estimation, but it should be kept in mind that errors of the order of 5% occur simply due to violations of the well-mixed condition.

In order to reveal how close ARTM simulates the dispersion of plumes to real world plume dispersion in the planetary boundary layer a case study was performed. The three-dimensional structure of simulated exhaust plumes was compared with airborne in situ observations under very unstable atmospheric conditions. Simulations with ARTM using the five different turbulence models were performed and analysed. The wind direction and the order of magnitude of the mixing ratios of the simulations of all turbulence models agreed well with the observations. However, the comparison of the simulated plumes of the turbulence models revealed significant differences of their three-dimensional structure, which also resulted in better or poorer agreement with the observations. The turbulence model ARTM2 (recommended by the Association of German Engineers until 2020) produced clearly too narrow plumes, which resulted in an overestimation of mixing ratio peaks. A workaround using the same turbulence model with subsequently alternating wind directions to mimic turbulent fluctuations not covered by the parametrisation resulted in a better agreement with the observations but at the expense of an unphysical rectangular mixing ratio distribution of the plume. The other turbulence models simulated wider plumes. The PRFMOD, MODHANNA and DEGRAZIA turbulence models showed plume width, mixing ratio peak values and mixing ratio integrals along the flight path in better agreement with the observations. ARTM3 resulted in only slightly wider plumes compared to ARTM2 still underestimating the observed plume width significantly. The probability distributions of the mixing ratio values along the flight path deviate significantly from the measurements for all the turbulence models, which is not surprising since ARTM only represents the mean turbulent dispersion but does not resolve individual eddies as seen in the observations. The observations are probably not sampled over a sufficient long period to produce a statistically representative and smooth probability distribution. Nevertheless, the statistical evaluation of the probability distributions and the point-to-point comparisons of simulations and observations indicated the MODHANNA turbulence model to perform slightly better than other turbulence models. However, without further comparison studies, the obtained

turbulence model ranking cannot be generalized to other stability conditions.

In order to put the validation of ARTM on a broader basis, the plume dispersion simulated by ARTM, using its default turbulence model ARTM2, was also compared to five different, more sophisticated atmospheric transport models under slightly unstable and very unstable atmospheric conditions. The intercomparison confirmed the same tendency of the ARTM2 turbulence model simulating too narrow dispersion plumes at very turbulent conditions. At less turbulent atmospheric conditions, the plume width simulated by ARTM was more comparable with observations as well as with simulated plumes from other state-of-the-art transport models. The simulated (synthetic) plumes were used to assess the applicability and the uncertainty of two methods, which are frequently used for the estimation of point source emissions from satellite observations. The two methods, called cross-sectional flux (X-flux) and integrated mass enhancement (IME) were applied to the ensemble of simulated CO_2 plumes converted to column mean dry air mixing ratios of CO_2 (XCO_2) as measured from satellites. This allows the evaluation of the methods and the estimation of their uncertainties. The evaluation of the two estimation methods for the emission rates from satellite CO_2 measurements showed deviations from the simulated emissions of up to 20% at daytime.

This work contributes to the validation of ARTM under unstable atmospheric conditions and improves the credibility of the simulation results. The findings of this study help to understand the impact of variations of input parameters on simulation results and to guide users of ARTM when interpreting the results of dispersion simulations. The study also reveals some shortcomings of ARTM and offers improvements to overcome these deficiencies. The results of this study demonstrate that ARTM is a useful tool that simulates the dispersion of tracers comparable to other computationally more expensive state-of-the-art transport models within the unstable and slightly unstable planetary boundary layer when choosing a proper turbulence model and turbulence parametrisation.

Chapter 7

Outlook

The analyses performed in this work resulted in new insights into the sensitivity of simulation results to the most important input parameters and the agreement of simulated dispersion plumes with observations. However, new questions arose that should be addressed in further studies.

The presented sensitivity analyses focused on gas as dispersion tracer while particulate matter was studied less because of the high quality of the filtering under routine operation of nuclear power plants. The occurrence of particulate matter with aerodynamic diameters larger than approx. 1 µm is massively reduced by filtering. Particulate matter smaller than 1 µm are assumed to show only weak deviations from the dispersion of gaseous tracers except for the influence of dry and wet deposition. However, the emissions of nuclear installations can contain a significant amount of particulate matter in the case of accidental releases. Particle size is an important characteristic that influences dispersion properties of tracers and thus is a source of simulation uncertainty. Further investigations about the impact of the particle size on the three-dimensional spread would result in a more complete knowledge about the most important parameters of ARTM.

The strong sensitivity of the dispersion on the selection of one of six stability classes results in large uncertainties in the case of an imprecise determination of the atmospheric stability. An alternative would be to determine the stability directly from the Obukhov length, which has the advantage of being a continuous quantity. However, the atmospheric stability is not linearly proportional to this parameter. For example, a variation of 50 m of the Obukhov length can cause the transition from very stable to less stable atmospheric conditions but at neutral conditions the atmosphere is insensitive to such a variation. This may lead to varying uncertainties when using poorly measured friction velocity and heat flux for the calculation of the Obukhov lengths as the turbulence parameter in ARTM. It is important to quantify these uncertainties and estimate their maximum contribution to the uncertainties of the simulation result. To do so, the application

of global sensitivity analysis methods such as the Sobol' indices and the δ-method seem to be promising.

Nevertheless, compared to the stability classes the usage of the continuous Obukhov length results in simulated plume volumes that better span the full range of possible plume volumes. However, the fact that some gaps were still present shows that the sampling of the Obukhov length values for simulations is not trivial and proper simulation experiments need to be designed. It is important to undertake further attempts to reveal whether the remaining gaps originate from the performed random sampling of the Obukhov length with uniform probability or whether they originate from the applied turbulence model. Additional sensitivity studies should also be performed with the alternative turbulence models proposed in this thesis. It cannot be ruled out that the sensitivity ranking depends on the selected turbulence model, though large changes in the ranking are unlikely.

The comparison of simulations with the five turbulence models with the measurements revealed substantial differences in the three-dimensional plume structure under very unstable atmospheric conditions. Unfortunately, similar observations for other atmospheric conditions were not available. Since a model has to simulate the dispersion close to real atmospheric dispersion under all atmospheric stabilities, more measurement data of plume dispersion under unstable, neutral and stable conditions are necessary. Measurements covering multiple transects and at multiple distances as performed during the CoMet 1.0 campaign are necessary to cover the plume structure in detail and to provide a sufficiently large statistical sample of situations thus enabling a meaningful evaluation. Furthermore, it is important that the observational data covers the whole depth of the planetary boundary layer. The data used in this study covered heights from 600 m up to the mixing layer top, thus it is not clear whether the simulations agree with observations below 600 m. Measurements below 600 m would be valuable since the simulations using different turbulence models differed significantly in this altitude range.

Another element that should be included in the design of a future measurement campaign is to perform repeated measurements at a given location within a time period of one hour. This would allow the calculation of hourly averaged concentration values at a location and account better for the statistical character of concentration measurements due to wind fluctuations. Such data sets could improve the evaluation of simulations by diminishing the temporal and spatial differences between simulation and observation. This would allow the evaluation of ARTM according to the first and the second criterion stated by De Visscher (2014) (see page 2) as well. The repeated measurement of in situ data at distinct locations within the entire planetary boundary layer is an enormous challenge for experimentalists but necessary for the derivation of time averaged concentration

values from measurements. One possible measurement campaign design is the usage of one or more aircraft that repeatedly fly along a planned flightpath. Another measurement design could be the application of a large number of unmanned aerial vehicles (UAVs) equipped with measurement devices. They could repeatedly hover at certain locations measuring the concentration of tracers. An extension of the measurements to several hours or days could extend the evaluation of ARTM beyond a short-term evaluation.

A further component for the success of a measurement campaign is to achieve the cooperation of providers of the emitting installations. They can provide temporally high resolution emission rates in order to strengthen the meaningfulness of comparison results by reducing source term uncertainties.

Furthermore, wind data are key parameters for atmospheric transport models. ARTM uses wind data at one arbitrary but fixed position in the simulation domain to model the wind and turbulence fields. The ground-based measurement of in situ wind data, e.g. from a weather pole, over the entire simulation period at a fixed location would be beneficial for the validation of ARTM. The extension of such measurements to times before the actual simulation period is even better because it allows the simulation of a fully evolved plume during that spin-off period based on one continuous wind data set.

Apart from the mentioned improvements concerning measurement data sets and campaign designs, the analyses showed also potential targets for the modelling. The five tested turbulence models are a selection of possible turbulence models discussed by the scientific community. Interestingly, the turbulence model MODHANNA that uses parts of the turbulence parametrisation presented by Hanna (1982) performed particularly well. It might be worth using the complete turbulence parametrisation of Hanna (1982) to compare it to the measurement data. This would make a direct comparison between the turbulence models of Hanna (1982) and Degrazia et al. (2000) under unstable conditions at large heights within the planetary boundary layer possible and would extend the analyses presented by Carvalho et al. (2002). There might also be other promising turbulence models that can be tested to further improve the accuracy of simulated plume dispersion compared to observations.

This outlook does not claim to mention all the questions that arise from the presented study. Nevertheless, it may help to guide future attempts to complete the understanding of the parametrisation of turbulent diffusion in computer models. It may also help to improve the modelling of the dispersion of tracers in the planetary boundary layer by using different turbulence models.

List of abbreviations

ADI	Alternating-Directions Implicit
ADM	atmospheric dispersion model
agl	above ground level
ARTM	Atmospheric Radionuclide Transport Model
BfS	Federal Office for Radiation Protection
BLM	boundary layer model
CFD	computational fluid dynamic
CoMet 1.0	Carbon Dioxide and Methane Mission
COSMO-GHG	Consortium for Small-scale Modeling-Greenhouse Gas
CH_4	methane
CO	carbon monoxide
CO_2	carbon dioxide
CO2M	Copernicus Anthropogenic Carbon Dioxide Monitoring
CPD	cumulative probability distribution
DLR	German aerospace center
Empa	Swiss Federal Laboratories for Material Science and Technology
E-PRTR	European Pollutant Release and Transfer Register
EULAG	Eulerian/semi-Lagrangian fluid solver
FUB	Freie Universität Berlin
GRS	Gesellschaft für Anlagen- und Reaktorsicherheit gGmbH
ICON-LEM	ICOsahedral Non-hydrostatic Large-Eddy Model
IME	integrated mass enhancement
LES	Large-Eddy-Simulation
LPDM	Lagrangian particle dispersion model

NO_2	nitrogen dioxides
NO_x	nitrogen oxides
NPP	Nuclear Power Plant
NWP	numerical weather prediction
PBL	planetary boundary layer
PD	probability distribution
PDF	probability density function
PM	particulate matter
PMAC	position of maximum activity concentration
RANS	Reynolds-averaged Navier-Stokes
SA	sensitivity analysis
SC	stability class
SRTM3	Shuttle Radar Topography Mission version 3
SO_2	sulphur dioxide
TM	turbulence model
UAV	unmanned aerial vehicle
VDI	Association of German Engineers
WRF-GHG	Weather Research and Forecasting-Greenhouse Gas
WRF-LES	Weather Research and Forecasting-Large-Eddy Simulation
XCO_2	column mean dry air mixing ratios of CO_2
X-flux	cross-sectional flux

Bibliography

Ahmadov, R., C. Gerbig, R. Kretschmer, S. Koerner, B. Neininger, A. J. Dolman, and C. Sarrat (2007). "Mesoscale covariance of transport and CO2 fluxes: Evidence from observations and simulations using the WRF-VPRM coupled atmosphere-biosphere model". In: *J. Geophys. Res.-Atmos.* 112.D22. ISSN: 0148-0227. DOI: 10.1029/2007JD008552 (cit. on p. 109).

Albergel, A., D. Martin, B. Strauss, and J.-M. Gros (1988). "The chernobyl accident: Modelling of dispersion over europe of the radioactive plume and comparison with air activity measurements". In: *Atmos Environ* 22.11, pp. 2431–2444. ISSN: 0004-6981. DOI: 10.1016/0004-6981(88)90475-1 (cit. on p. 21).

AMS (29 October 2022). *Glossary of Meteorology*. American Meteorological Society. URL: https://glossary.ametsoc.org/wiki/Dispersion. last update 25 April 2012 (cit. on p. 19).

Andersen, T., Z. Zhao, M. de Vries, J. Necki, J. Swolkien, M. Menoud, T. Röckmann, A. Roiger, A. Fix, W. Peters, and H. Chen (2023). "Local-to-regional methane emissions from the Upper Silesian Coal Basin (USCB) quantified using UAV-based atmospheric measurements". In: *Atmos. Chem. Phys.* 23.9, pp. 5191–5216. ISSN: 1680-7324. DOI: 10.5194/acp-23-5191-2023 (cit. on p. 88).

Anfossi, D., E. Ferrero, G. Brusasca, A. Marzorati, and G. Tinarelli (1993). "A Simple Way of Computing Buoyant Plume Rise in Lagrangian Stochastic Dispersion Models". In: *Atmos. Environ. A-Gen.* 27.9, pp. 1443–1451. ISSN: 0960-1686. DOI: 10.1016/0960-1686(93)90130-Q (cit. on p. 25).

Apsimon, H. M., A. J. H. Goddard, and J. Wrigley (1985). "Long-range atmospheric dispersion of radioisotopes—i. The MESOS model". In: *Atmos Environ* 19.1, pp. 99–111. ISSN: 0004-6981. DOI: 10.1016/0004-6981(85)90141-6 (cit. on p. 21).

Arnold, D., C. Maurer, G. Wotawa, R. Draxler, K. Saito, and P. Seibert (2015). "Influence of the Meteorological Input on the Atmospheric Transport Modelling with FLEXPART of Radionuclides from the Fukushima Daiichi Nuclear Accident". In: *J. Environ. Radioactiv.* 139, pp. 212–225. ISSN: 0265-931X. DOI: 10.1016/j.jenvrad.2014.02.013 (cit. on p. 22).

Arnold, D., P. Seibert, H. Nagai, G. Wotawa, P. Skomorowski, K. Baumann-Stanzer, E. Polreich, M. Langer, A. Jones, M. Hort, S. Andronopoulos, J. G. Bartzis, E. Davakis, P. Kaufmann, and A. Vargas (2012). "Lagrangian Models for Nuclear Studies: Examples and Applications". In: *Lagrangian Modeling of the Atmosphere*. Geophysical Monograph Series, pp. 329–348. ISBN: 9781118704578. DOI: 10.1029/2012GM001294 (cit. on p. 21).

AVV (2012). *Allgemeine Verwaltungsvorschrift zu § 47 Strahlenschutzverordnung: Ermittlung der Strahlenexposition durch die Ableitung radioaktiver Stoffe aus kerntechnischen Anlagen oder Einrichtungen*. Government Document. Bundesministerium für Umwelt, Naturschutz und Reaktorsicherheit. URL: https://www.verwaltungsvorschriften-im-internet.de/bsvwvbund_28082012_RSII.htm (cit. on pp. 22, 44–46).

AVV Tätigkeiten (2020). *Allgemeine Verwaltungsvorschrift zur Ermittlung der Exposition von Einzelpersonen der Bevölkerung durch genehmigungs- oder anzeigebedürftige Tätigkeiten (AVV Tätigkeiten)*. Government Document. Köln: Bundesministerium für Umwelt, Naturschutz und nukleare Sicherheit. URL: http://www.verwaltungsvorschriften-im-internet.de/bsvwvbund_08062020_SII51148301.htm (cit. on p. 22).

Bahlali, M. L., C. Henry, and B. Carissimo (2020). "On the Well-Mixed Condition and Consistency Issues in Hybrid Eulerian/Lagrangian Stochastic Models of Dispersion". In: *Bound.-Lay. Meteorol.* 174.2, pp. 275–296. ISSN: 1573-1472. DOI: 10.1007/s10546-019-00486-9 (cit. on pp. 27, 73).

Barnicki, J., A. Foss, and J. Saltbones (1996). "Severe Nuclear Accident Program (SNAP) - An Operational Dispersion Model". In: *WIT Transon Ecol Envir* 16, p. 10. URL: https://www.witpress.com/elibrary/wit-transactions-on-ecology-and-the-environment/16/9062 (cit. on p. 21).

Beck, V., T. Koch, R. Kretschmer, J. Marshall, R. Ahmadov, C. Gerbig, D. Pillai, and M. Heimann (2011). *The WRF Greenhouse Gas Model (WRF-GHG)*. Report. Max Planck Institute for Biogeochemistry. URL: https://www.bgc-jena.mpg.de/bgc-systems/pmwiki2/uploads/Download/Wrf-ghg/WRF-GHG_Techn_Report.pdf (cit. on p. 109).

Becker, A., G. Wotawa, L.-E. De Geer, P. Seibert, R. R. Draxler, C. Sloan, R. D'Amours, M. Hort, H. Glaab, P. Heinrich, Y. Grillon, V. Shershakov, K. Katayama, Y. Zhang, P. Stewart, M. Hirtl, M. Jean, and P. Chen (2007). "Global backtracking of anthropogenic radionuclides by means of a receptor oriented ensemble dispersion modelling system in support of Nuclear-Test-Ban Treaty verification". In: *Atmos. Environ.* 41.21, pp. 4520–4534. ISSN: 1352-2310. DOI: 10.1016/j.atmosenv.2006.12.048 (cit. on p. 22).

Beevers, S. D. and M. L. Williams (2020). "Chapter 6 - Traffic-related air pollution and exposure assessment". In: *Traffic-Related Air Pollution*. Ed. by H. Khreis,

M. Nieuwenhuijsen, J. Zietsman, and T. Ramani. Elsevier, pp. 137–162. ISBN: 978-0-12-818122-5. DOI: 10.1016/B978-0-12-818122-5.00006-5. URL: https://www.sciencedirect.com/science/article/pii/B9780128181225000065 (cit. on p. 19).

Berchet, A., K. Zink, D. Oettl, J. Brunner, L. Emmenegger, and D. Brunner (2017). "Evaluation of High-Resolution GRAMM–GRAL (v15.12/v14.8) NOx Simulations over the City of Zürich, Switzerland". In: *Geosci. Model Dev.* 10.9, pp. 3441–3459. ISSN: 1991-9603. DOI: 10.5194/gmd-10-3441-2017 (cit. on p. 22).

Borgonovo, E. (2007). "A New Uncertainty Importance Measure". In: *Reliab. Eng. Syst. Safe.* 92.6, pp. 771–784. ISSN: 0951-8320. DOI: 10.1016/j.ress.2006.04.015 (cit. on pp. 57, 68).

Borgonovo, E. and E. Plischke (2016). "Sensitivity Analysis: A Review of Recent Advances". In: *Eur. J. Oper. Res.* 248.3, pp. 869–887. ISSN: 0377-2217. DOI: 10.1016/j.ejor.2015.06.032 (cit. on p. 55).

Borrego, C., O. Tchepel, A. M. Costa, J. H. Amorim, and A. I. Miranda (2003). "Emission and dispersion modelling of Lisbon air quality at local scale". In: *Atmos. Environ.* 37.37, pp. 5197–5205. ISSN: 1352-2310. DOI: 10.1016/j.atmosenv.2003.09.004 (cit. on p. 22).

Briggs, G. A. (1971). "ME 8E - Some Recent Analysis of Plume Rise Observasion". In: *Proceedings of the Second International Clean Air Congress*. Ed. by H. M. Englund and W. T. Beery. Academic Press, pp. 1029–1032. ISBN: 978-0-12-239450-8. DOI: 10.1016/B978-0-12-239450-8.50183-0 (cit. on pp. 40, 41).

— (May 1973). *Diffusion Estimation for Small Emissions. Preliminary Report.* Report. DOI: 10.2172/5118833 (cit. on p. 114).

Brunner, D., G. Kuhlmann, S. Henne, E. Koene, B. Kern, S. Wolff, C. Voigt, P. Jöckel, C. Kiemle, A. Roiger, A. Fiehn, S. Krautwurst, K. Gerilowski, H. Bovensmann, J. Borchardt, M. Galkowski, C. Gerbig, J. Marshall, A. Klonecki, P. Prunet, R. Hanfland, M. Pattantyús-Ábrahám, A. Wyszogrodzki, and A. Fix (2023). "Evaluation of simulated CO2 power plant plumes from six high-resolution atmospheric transport models". In: *Atmos. Chem. Phys.* 23.4, pp. 2699–2728. ISSN: 1680-7324. DOI: 10.5194/acp-23-2699-2023 (cit. on pp. 87, 88, 91, 92, 109–111, 113–116).

Brunner, D., G. Kuhlmann, J. Marshall, V. Clément, O. Fuhrer, G. Broquet, A. Löscher, and Y. Meijer (2019). "Accounting for the Vertical Distribution of Emissions in Atmospheric CO2 Simulations". In: *Atmos. Chem. Phys.* 19.7, pp. 4541–4559. ISSN: 1680-7324. DOI: 10.5194/acp-19-4541-2019 (cit. on pp. 109, 110).

Bullin, J. A. and A. E. Dukler (1974). "Stochastic modeling of turbulent diffusion with hybrid computer". In: *Environ Sci Tech* 8.2, pp. 156–165. ISSN: 0013-936X. DOI: 10.1021/es60087a003 (cit. on p. 20).

Burgin, L., M. Ekström, and S. Dessai (2017). "Combining dispersion modelling with synoptic patterns to understand the wind-borne transport into the UK of the bluetongue disease vector". In: *Int. J. Biometeorol.* 61.7, pp. 1233–1245. ISSN: 1432-1254. DOI: 10.1007/s00484-016-1301-1 (cit. on p. 21).

Businger, J. A., J. C. Wyngaard, Y. Izumi, and E. F. Bradley (1971). "Flux-Profile Relationships in the Atmospheric Surface Layer". In: *J. Atmos. Sci.* 28.2, pp. 181–189. DOI: 10.1175/1520-0469(1971)028<0181:FPRITA>2.0.CO;2 (cit. on p. 16).

Carvalho, J. C., D. Anfossi, S. Trini Castelli, and G. A. Degrazia (2002). "Application of a model system for the study of transport and diffusion in complex terrain to the TRACT experiment". In: *Atmos Environ* 36.7, pp. 1147–1161. ISSN: 1352-2310. DOI: 10.1016/S1352-2310(01)00559-3 (cit. on p. 123).

Chen, W. R. and L. R. Zhao (2015). "Review – Volcanic Ash and its Influence on Aircraft Engine Components". In: *Procedia Engineer.* 99, pp. 795–803. ISSN: 1877-7058. DOI: 10.1016/j.proeng.2014.12.604 (cit. on p. 21).

Chino, M., H. Nakayama, H. Nagai, H. Terada, G. Katata, and H. Yamazawa (2011). "Preliminary Estimation of Release Amounts of 131I and 137Cs Accidentally Discharged from the Fukushima Daiichi Nuclear Power Plant into the Atmosphere". In: *J. Nucl. Sci. Technol.* 48.7, pp. 1129–1134. ISSN: 0022-3131. DOI: 10.1080/18811248.2011.9711799 (cit. on p. 22).

Cohen, I. M. and P. K. Kundu (2007). *Fluid Mechanics*. Vol. 4. Burlington, United States: Elsevier Science & Technology. ISBN: 9780080555836 (cit. on pp. 24, 25).

Conover, W. J. (1980). *Practical Nonparametric Statistics*. 2nd ed. New York: Wiley & Sons. ISBN: 0-471-02867-3 (cit. on p. 106).

De Meutter, P., J. Camps, A. Delcloo, and P. Termonia (2017). "Assessment of the announced North Korean nuclear test using long-range atmospheric transport and dispersion modelling". In: *Sci. Rep.-UK* 7.1, p. 8762. ISSN: 2045-2322. DOI: 10.1038/s41598-017-07113-y (cit. on p. 22).

De Visscher, A. (2014). *Air Dispersion Modeling*. Hoboken, New Jersey: John Wiley & Sons, Inc. ISBN: 9781118723074 (cit. on pp. 1, 2, 19, 23, 24, 103, 122).

Degrazia, G. A., D. Anfossi, J. C. Carvalho, C. Mangia, T. Tirabassi, and H. F. Campos Velho (2000). "Turbulence Parameterisation for PBL Dispersion Models in All Stability Conditions". In: *Atmos. Environ.* 34.21, pp. 3575–3583. ISSN: 1352-2310. DOI: 10.1016/S1352-2310(00)00116-3 (cit. on pp. 4, 73, 77, 123).

Devenish, B. J., P. N. Francis, B. T. Johnson, R. S. J. Sparks, and D. J. Thomson (2012). "Sensitivity Analysis of Dispersion Modeling of Volcanic Ash from

Eyjafjallajökull in May 2010". In: *J. Geophys. Res.-Atmos.* 117.D20. ISSN: 0148-0227. DOI: 10.1029/2011jd016782 (cit. on p. 21).

Doms, G. and B. M. (Nov. 2013). *A Description of the Nonhydrostatic Regional COSMO-Model Part I: Dynamics and Numerics*. Report. Consortium for Small-Scale Modelling. DOI: 10.5676/DWD_pub/nwv/cosmo-doc_5.00_I (cit. on p. 29).

Draxler, R. R. and G. D. Hess (1998). "An overview of the HYSPLIT_4 modelling mystem for trajectories, dispersion and deposition". In: *Aust. Meteorol. Mag.* 47.4, pp. 295–308 (cit. on p. 29).

Dyer, A. J. (1974). "A review of flux-profile relationships". In: *Bound.-Lay. Meteorol.* 7.3, pp. 363–372. ISSN: 1573-1472. DOI: 10.1007/BF00240838 (cit. on p. 16).

Eichhorn, J. and A. Kniffka (2010). "The numerical flow model MISKAM: State of development and evaluation of the basic version". In: *Meteorol. Z.* 19.1, pp. 81–90. DOI: 10.1127/0941-2948/2010/0425 (cit. on p. 29).

Etling, D. (2008). *Theroretische Meteorologie*. 3. Berlin Heidelberg New York: Springer-Verlag. ISBN: 978-3-540-75978-2 (cit. on pp. 8, 13–15, 17, 18, 24, 25).

Farchi, A., M. Bocquet, Y. Roustan, A. Mathieu, and A. Quérel (2016). "Using the Wasserstein distance to compare fields of pollutants: application to the radionuclide atmospheric dispersion of the Fukushima-Daiichi accident". In: *Tellus B* 68.1, p. 31682. DOI: 10.3402/tellusb.v68.31682 (cit. on p. 88).

Farr, T. G., P. A. Rosen, E. Caro, R. Crippen, R. Duren, S. Hensley, M. Kobrick, M. Paller, E. Rodriguez, L. Roth, D. Seal, S. Shaffer, J. Shimada, J. Umland, M. Werner, M. Oskin, D. Burbank, and D. Alsdorf (2007). "The Shuttle Radar Topography Mission". In: *Rev. Geophys.* 45.2. ISSN: 8755-1209. DOI: https://doi.org/10.1029/2005RG000183 (cit. on pp. 91, 92).

Fiehn, A., J. Kostinek, M. Eckl, T. Klausner, M. Gałkowski, J. Chen, C. Gerbig, T. Röckmann, H. Maazallahi, M. Schmidt, P. Korbeń, J. Nęçki, P. Jagoda, N. Wildmann, C. Mallaun, R. Bun, A. L. Nickl, P. Jöckel, A. Fix, and A. Roiger (2020). "Estimating CH4, CO2 and CO emissions from coal mining and industrial activities in the Upper Silesian Coal Basin using an aircraft-based mass balance approach". In: *Atmos. Chem. Phys.* 20.21, pp. 12675–12695. ISSN: 1680-7324. DOI: 10.5194/acp-20-12675-2020 (cit. on p. 88).

Fix, A., A. Amediek, H. Bovensmann, G. Ehret, C. Gerbig, K. Gerilowski, K. Pfeilsticker, A. Roiger, and M. Zöger (2018). "CoMet: An Airborne Mission to Simultaneously Measure CO2 and CH4 Using Lidar, Passive Remote Sensing, and In-Situ Techniques". In: *EPJ Web Conf.* 176, p. 02003. DOI: 10.1051/epjconf/201817602003 (cit. on p. 88).

Foken, T. (2016). *Angewandte Meteorologie: Mikrometeorologische Methoden*. 3rd ed. Berlin, Heidelberg: Springer Spektrum, pp. XXII, 394. ISBN: 978-3-642-25525-0. DOI: 10.1007/978-3-642-25525-0 (cit. on pp. 11, 13).

Frey, H. C. and S. R. Patil (2002). "Identification and Review of Sensitivity Analysis Methods". In: *Risk Anal.* 22.3, pp. 553–578. ISSN: 0272-4332. DOI: 10.1111/0272-4332.00039 (cit. on pp. 27, 53).

Gal-Chen, T. and R. C. J. Somerville (1975). "On the use of a coordinate transformation for the solution of the Navier-Stokes equations". In: *J. Comput. Phys.* 17.2, pp. 209–228. ISSN: 0021-9991. DOI: 10.1016/0021-9991(75)90037-6 (cit. on p. 38).

Gałkowski, M., A. Jordan, M. Rothe, J. Marshall, F. T. Koch, J. Chen, A. Agusti-Panareda, A. Fix, and C. Gerbig (2021). "In situ observations of greenhouse gases over Europe during the CoMet 1.0 campaign aboard the HALO aircraft". In: *Atmos. Meas. Tech.* 14.2, pp. 1525–1544. ISSN: 1867-8548. DOI: 10.5194/amt-14-1525-2021 (cit. on p. 88).

Gariazzo, C., V. Papaleo, A. Pelliccioni, G. Calori, P. Radice, and G. Tinarelli (2007). "Application of a Lagrangian particle model to assess the impact of harbour, industrial and urban activities on air quality in the Taranto area, Italy". In: *Atmos. Environ.* 41.30, pp. 6432–6444. ISSN: 1352-2310. DOI: 10.1016/j.atmosenv.2007.06.005 (cit. on p. 22).

Garratt, J. R. (1992). *The atmospheric boundary layer*. Cambridge: Cambridge University Press, p. 316. ISBN: 0-521-38052-9 (cit. on pp. 9, 10).

Gerilowski, K., A. Tretner, T. Krings, M. Buchwitz, P. P. Bertagnolio, F. Belemezov, J. Erzinger, J. P. Burrows, and H. Bovensmann (2011). "MAMAP – a new spectrometer system for column-averaged methane and carbon dioxide observations from aircraft: instrument description and performance analysis". In: *Atmos. Meas. Tech.* 4.2, pp. 215–243. ISSN: 1867-8548. DOI: 10.5194/amt-4-215-2011 (cit. on p. 110).

Gesellschaft für Anlagen- und Reaktorsicherheit (GRS) gGmbH (2007). *Entwicklung, Validierung und Bereitstellung eines Atmosphärischen Ausbreitungsmodells für Luftgetragene Radioaktive Stoffe der Basis des Ausbreitungsmodells AUSTAL 2000 der neuen TA Luft*. Government Document. Bonn: Bundesministerium für Umwelt, Naturschutz und Reaktorsicherheit. URL: https://www.bmuv.de/download/bmu-2007-710-entwicklung-validierung-und-bereitstellung-eines-atmosphaerischen-ausbreitungsmodells-fuer-luftgetragene-radioaktive-stoffe-auf-der-basis-des-ausbreitungsmodells-austal2000-der-neuen-ta-luft (cit. on p. 30).

— (2015). *ARTM Atmospheric Radionuclide-Transport-Model*. Computer Program. Version 2.8.0. Source Code. Lagrangian Particle Disperion Model (cit. on pp. 40–42, 47, 52, 74).

Gloster, J., A. Jones, A. Redington, L. Burgin, J. H. Sørensen, R. Turner, M. Dillon, P. Hullinger, M. Simpson, P. Astrup, G. Garner, P. Stewart, R. D'Amours, R. Sellers, and D. Paton (2010). "Airborne spread of foot-and-mouth disease – Model intercomparison". In: *Vet. J.* 183.3, pp. 278–286. ISSN: 1090-0233. DOI: 10.1016/j.tvjl.2008.11.011 (cit. on p. 21).

Gospodarczyk, M. M. (July 2022). *Amid Global Crisis, Nuclear Power Provides Energy security with Increased Electricity Generation*. Vienna: International Atomic Energy Agency IAEA. URL: https://www.iaea.org/newscenter/news/amid-global-crises-nuclear-power-provides-energy-security-with-increased-electricity-generation-in-2021. 9 July (cit. on p. 1).

Gryning, S. E., A. A. M. Holtslag, J. S. Irwin, and B. Sivertsen (1987). "Applied Dispersion Modelling Based on Meteorological Scaling Parameters". In: *Atmos. Environ.* 21.1, pp. 79–89. ISSN: 0004-6981. DOI: 10.1016/0004-6981(87)90273-3 (cit. on pp. 4, 74).

Gudiksen, P. H., T. F. Harvey, and R. Lange (1989). "Chernobyl Source Term, Atmospheric Dispersion, and Dose Estimation". In: *Health Phys.* 57.5, pp. 697–706. ISSN: 0017-9078. URL: https://journals.lww.com/health-physics/Fulltext/1989/11000/Chernobyl_Source_Term,_Atmospheric_Dispersion,_and.1.aspx (cit. on p. 22).

Hallenbeck, W. H. (1994). *Radiation Protection*. Boca Raton, London, New York: CRC Press. ISBN: 0-87371-996-4 (cit. on p. 45).

Hamby, D. M. (1994). "A Review of Techniques for Parameter Sensitivity Analysis of Environmental Models". In: *Environ. Monit. Assess.* 32.2, pp. 135–154. ISSN: 1573-2959. DOI: 10.1007/BF00547132 (cit. on pp. 27, 53–55).

— (1995). "A Comparison of Sensitivity Analysis Techniques". In: *Health Phys.* 68.2, pp. 195–204. ISSN: 0017-9078. URL: https://journals.lww.com/health-physics/Fulltext/1995/02000/A_Comparison_of_Sensitivity_Analysis_Techniques.5.aspx (cit. on p. 54).

Hanfland, R., D. Brunner, C. Voigt, A. Fiehn, A. Roiger, and M. Pattantyús-Ábrahám (2023). "The Lagrangian Atmospheric Radionuclide Transport Model (ARTM) - Sensitivity studies and evaluation using airborne measurements of power plant emissions". In: *EGUsphere [preprint]* 2023, pp. 1–35. DOI: 10.5194/egusphere-2023-245 (cit. on pp. 27, 29, 53, 54, 67, 68, 73, 75, 79, 81–95, 97, 99–108).

Hanfland, R., M. Pattantyús-Ábrahám, C. Richter, D. Brunner, and C. Voigt (2022). "The Lagrangian Atmospheric Radionuclide Transport Model (ARTM) - Development, Description and Sensitivity Analysis". In: *Air Qual. Atmos. Health*. DOI: 10.1007/s11869-022-01188-x (cit. on pp. 3, 25, 29, 32, 42, 43, 46, 53, 58–60, 62, 64–66, 74, 78, 111, 117).

Hanna, S. R. (1982). "Applications in Air Pollution Modeling". In: *Atmospheric Turbulence and Air Pollution Modelling: A Course held in The Hague, 21–25 September, 1981*. Ed. by F. T. M. Nieuwstadt and H. van Dop. Dordrecht: Springer Netherlands, pp. 275–310. ISBN: 978-94-010-9112-1. DOI: 10.1007/978-94-010-9112-1_7 (cit. on pp. 4, 73, 76, 123).

Hayes, E. T., T. P. Curran, and V. A. Dodd (2006). "A dispersion modelling approach to determine the odour impact of intensive poultry production units in Ireland". In: *Bioresource Technol.* 97.15, pp. 1773–1779. ISSN: 0960-8524. DOI: 10.1016/j.biortech.2005.09.019 (cit. on p. 21).

Henne, S., D. Brunner, B. Oney, M. Leuenberger, W. Eugster, I. Bamberger, F. Meinhardt, M. Steinbacher, and L. Emmenegger (2016). "Validation of the Swiss methane emission inventory by atmospheric observations and inverse modelling". In: *Atmos. Chem. Phys.* 16.6, pp. 3683–3710. ISSN: 1680-7324. DOI: 10.5194/acp-16-3683-2016 (cit. on p. 22).

Herman, J. and W. Usher (2017). "SALib: An Open-Source Python Library for Sensitivity Analysis". In: *J. Open Source Softw.* 2.9, p. 97. DOI: 10.21105/joss.00097 (cit. on p. 57).

— (2023). *SALib: Basics*. URL: https://salib.readthedocs.io/en/latest/user_guide/basics.html. last access 5 December 2023 (cit. on pp. 57, 68).

Hettrich, S. (2017). "Validation and Verification of the Atmospheric Radionuclide Transport Model (ARTM)". Phd-Thesis (cit. on pp. 3, 4).

Hicks, B. B. (1985). "Behavior of Turbulence Statistics in the Convective Boundary Layer". In: *J Appl Meteorol Clim* 24.6, pp. 607–614. DOI: 10.1175/1520-0450(1985)024<0607:BOTSIT>2.0.CO;2 (cit. on p. 74).

Hoffman, F. O. and R. H. Gardner (1983). "Evaluation of Uncertainties in Environmental Radiological Assessment Models". In: *Radiological Assessment, A Textbook on Environmental Dose Analysis*. Ed. by J. E. Till and H. R. Meyer. Washington: U.S. Nuclear Regulatory Commission. Chap. 11. URL: https://www.nrc.gov/docs/ML0917/ML091770419.pdf (cit. on p. 55).

Holmes, N. S. and L. Morawska (2006). "A review of dispersion modelling and its application to the dispersion of particles: An overview of different dispersion models available". In: *Atmos. Environ.* 40.30, pp. 5902–5928. ISSN: 1352-2310. DOI: 10.1016/j.atmosenv.2006.06.003 (cit. on pp. 19, 23, 26).

Homicz, G. F. (2002). *Three-Dimensional Wind Filed Modeling: A Review*. Report. Sandia National Laboratories. DOI: 10.2172/801406 (cit. on p. 36).

Iman, R. L. and J. C. Helton (1988). "An Investigation of Uncertainty and Sensitivity Analysis Techniques for Computer Models". In: *Risk Anal.* 8.1, pp. 71–90. ISSN: 0272-4332. DOI: 10.1111/j.1539-6924.1988.tb01155.x (cit. on p. 54).

Ionov, D. V., M. V. Makarova, F. Hase, S. C. Foka, V. S. Kostsov, C. Alberti, T. Blumenstock, T. Warneke, and Y. A. Virolainen (2021). "The CO2 Integral Emission by the Megacity of St Petersburg as Quantified from Ground-Based FTIR Measurements Combined with Dispersion Modelling". In: *Atmos. Chem. Phys.* 21.14, pp. 10939–10963. ISSN: 1680-7324. DOI: 10.5194/acp-21-10939-2021 (cit. on p. 22).

Jacob, P. and H. G. Paretzke (1985). "Air-ground Interface Correction Factors for Gamma Emitters in Air". In: *Health Phys.* 48.2, pp. 183–191. ISSN: 0017-9078. DOI: 10.1097/00004032-198502000-00005 (cit. on p. 46).

Jacob, P., H. G. Paretzke, and J. Wölfel (1984). "Monte Carlo Calculation and Analytical Approximation of Gamma-Ray Buildup Factors in Air". In: *Nucl. Sci. Eng.* 88.2, pp. 113–122. ISSN: 0029-5639. DOI: 10.13182/NSE84-A28405 (cit. on p. 45).

Jähn, M., G. Kuhlmann, Q. Mu, J. M. Haussaire, D. Ochsner, K. Osterried, V. Clément, and D. Brunner (2020). "An online emission module for atmospheric chemistry transport models: implementation in COSMO-GHG v5.6a and COSMO-ART v5.1-3.1". In: *Geosci. Model Dev.* 13.5, pp. 2379–2392. ISSN: 1991-9603. DOI: 10.5194/gmd-13-2379-2020 (cit. on p. 109).

Janicke, L. (1985). "Particle Simulation of Dust Transport and Deposition and Comparison with Conventional Models". In: *Air Pollution Modeling and Its Application IV*. Ed. by C. De Wispelaere. Boston, MA: Springer US, pp. 759–769. ISBN: 978-1-4613-2455-3. DOI: 10.1007/978-1-4613-2455-3_41 (cit. on p. 43).

— (Aug. 2000). *A random walk model for turbulent diffusion*. Report. Janicke Consulting. URL: http://www.janicke.de/data/bzu/bzu-001-01.pdf (cit. on p. 40).

Janicke, L. and U. Janicke (Feb. 2003). *Entwicklung eines modellgestützen Beurteilungssystems für den anlagenbezogenen Immissionsschutz*. Report. Janicke Consulting. URL: https://www.umweltbundesamt.de/sites/default/files/medien/2338/dokumente/a2k-1.0.6-report_de.pdf (cit. on pp. 30, 36).

Janicke, U. (July 2022a). *Statistical Uncertainty estimated by AUSTAL2000*. Personal Communication (cit. on p. 52).

— (Jan. 2022b). *Statistische Unsicherheit*. Personal Communication (cit. on p. 52).

Janicke, U. and L. Janicke (Oct. 2004). *Weiterentwicklung eines diagnostischen Windfeldmodells für den anlagenbezogenen Immissionsschutz (TA Luft)*. Report UBA-FB000842. Janicke Consulting (cit. on p. 30).

— (Feb. 2011). *Some aspects of the definition of meteorological boundary layer profiles and comparisons with measurements*. Report. Janicke Consulting. URL: https://www.janicke.de/data/bzu/bzu-007-01.pdf (cit. on pp. 4, 73, 74).

Janicke Consulting (2014). *Austal2000 - Programmbeschreibung zu Version 2.6*. Dessau-Roßlau: Umweltbundesamt (cit. on pp. 34–39, 47).
— (Feb. 2022). *Dispersion Model LASAT Version 3.4. Reference Book*. Überlingen: Janicke Consulting (cit. on pp. 47, 51, 52).
Janicke Consulting and Gesellschaft für Anlagen- und Reaktorsicherheit mbH (2015). *TALdia*. Computer Program. Version 2.2.2. Source Code. Diagnostic Wind Field Model (cit. on pp. 31, 34).
Joe, S. and F. Y. Kuo (2008). "Constructing Sobol' Sequences with Better Two-Dimensional Projections". In: *SIAM J. Sci. Comput.* 30.5, pp. 2635–2654. DOI: 10.1137/070709359 (cit. on p. 57).
Jones, A., D. Thomson, M. Hort, and B. Devenish (2007). "The U.K. Met Office's Next-Generation Atmospheric Dispersion Model, NAME III". In: *Air Pollution Modeling and Its Application XVII*. Ed. by C. Borrego and A.-L. Norman. Springer US, pp. 580–589. ISBN: 978-0-387-68854-1. DOI: 10.1007/978-0-387-68854-1_62 (cit. on p. 21).
Karppinen, A., J. Kukkonen, T. Elolähde, M. Konttinen, T. Koskentalo, and E. Rantakrans (2000). "A modelling system for predicting urban air pollution: model description and applications in the Helsinki metropolitan area". In: *Atmos. Environ.* 34.22, pp. 3723–3733. ISSN: 1352-2310. DOI: 10.1016/S1352-2310(00)00074-1 (cit. on p. 22).
Katharopoulos, I., D. Brunner, L. Emmenegger, M. Leuenberger, and S. Henne (2022). "Lagrangian Particle Dispersion Models in the Grey-Zone of Turbulence: Adaptions to FLEXPART-COSMO for Simulations at 1 km Grid Resolution". In: *Bound.-Lay. Meteorol.* DOI: 10.1007/s10546-022-00728-3 (cit. on p. 73).
Keller, L. and A. Friedmann (1924). "Differentialgleichungen für die turbulente Bewegung einer kompressiblen Flüssigkeit". In: *Proc. First. Int. Congr. Appl. Mech*, pp. 395–405 (cit. on p. 13).
Kern, B. and P. Jöckel (2016). "A diagnostic interface for the ICOsahedral Non-hydrostatic (ICON) modelling framework based on the Modular Earth Submodel System (MESSy v2.50)". In: *Geosci. Model Dev.* 9.10, pp. 3639–3654. ISSN: 1991-9603. DOI: 10.5194/gmd-9-3639-2016 (cit. on p. 109).
Kerschgens, M. J., C. Nölle, and R. Martens (2000). "Comments on Turbulence Parameters for the Calculation of Dispersion in the Atmospheric Boundary Layer". In: *Meteorol. Z.* 9.3, pp. 155–163. DOI: 10.1127/metz/9/2000/155 (cit. on pp. 4, 74).
Klausner, T., M. Mertens, H. Huntrieser, M. Gałkowski, G. Kuhlmann, R. Baumann, A. Fiehn, P. Jöckel, M. Pühl, and A. Roiger (2020). "Urban Greenhouse Gas Emissions from the Berlin Area: A Case Study Using Airborne CO2 and

CH4 In Situ Observations in Summer 2018". In: *Elementa Sci. Anthropoc.* 8.1. DOI: 10.1525/elementa.411 (cit. on p. 89).

Kleijnen, J. P. C. (1995). "Verification and validation of simulation models". In: *Eur. J. Oper. Res.* 82.1, pp. 145–162. ISSN: 0377-2217. DOI: 10.1016/0377-2217(94)00016-6 (cit. on pp. 2, 3, 27).

Klug, W. (1969). "Ein Verfahren zur Bestimmung der Ausbreitungsbedingungen aus synoptischen Beobachtungen". In: *Staub Reinhalt. Luft* 29.4, pp. 143–147. ISSN: 0039-0771 (cit. on pp. 31, 91).

Kostinek, J., A. Roiger, M. Eckl, A. Fiehn, A. Luther, N. Wildmann, T. Klausner, A. Fix, C. Knote, A. Stohl, and A. Butz (2021). "Estimating Upper Silesian Coal Mine Methane Emissions from Airborne In Situ Observations and Dispersion Modeling". In: *Atmos. Chem. Phys.* 21.11, pp. 8791–8807. ISSN: 1680-7324. DOI: 10.5194/acp-21-8791-2021 (cit. on p. 88).

Kraichnan, R. H. and D. Montgomery (1980). "Two-dimensional turbulence". In: *Rep. Prog. Phys.* 43.5, p. 547. ISSN: 0034-4885. DOI: 10.1088/0034-4885/43/5/001 (cit. on p. 10).

Krautwurst, S., K. Gerilowski, J. Borchardt, N. Wildmann, M. Gałkowski, J. Swolkień, J. Marshall, A. Fiehn, A. Roiger, T. Ruhtz, C. Gerbig, J. Necki, J. P. Burrows, A. Fix, and H. Bovensmann (2021). "Quantification of CH4 coal mining emissions in Upper Silesia by passive airborne remote sensing observations with the Methane Airborne MAPper (MAMAP) instrument during the CO2 and Methane (CoMet) campaign". In: *Atmos. Chem. Phys.* 21.23, pp. 17345–17371. ISSN: 1680-7324. DOI: 10.5194/acp-21-17345-2021 (cit. on pp. 88, 110).

KTA 1508 (Nov. 2017). *Instrumentation for Determining the Dispersion of Radioactive Substances in the Atmosphere*. Report. Nuclear Safety Standards Commission (KTA) (cit. on pp. 37, 91, 92).

Lang, N., W. Jetz, K. Schindler, and J. D. Wegner (2022). "A high-resolution canopy height model of the Earth". In: *arXiv [preprint]*. DOI: 10.48550/arXiv.2204.08322 (cit. on p. 60).

Lauritzen, B. and T. Mikkelsen (1999). "A probabilistic dispersion model applied to the long-range transport of radionuclides from the Chernobyl accident". In: *Atmos. Environ.* 33.20, pp. 3271–3279. ISSN: 1352-2310. DOI: 10.1016/S1352-2310(99)00108-9 (cit. on p. 22).

Lee, U., C. Lee, M. Kim, and H. R. Kim (2019). "Analysis of the influence of nuclear facilities on environmental radiation by monitoring the highest nuclear power plant density region". In: *Nucl. Eng. Technol.* 51.6, pp. 1626–1632. ISSN: 1738-5733. DOI: 10.1016/j.net.2019.04.007 (cit. on p. 22).

Leelőssy, Á., I. Lagzi, A. Kovács, and R. Mészáros (2018). "A review of numerical models to predict the atmospheric dispersion of radionuclides". In: *J. Environ.*

Radioact. 182, pp. 20–33. ISSN: 1879-1700 (Electronic) 0265-931X (Linking). DOI: 10.1016/j.jenvrad.2017.11.009 (cit. on pp. 20, 26).

Leelőssy, Á., F. Molnár, F. Izsák, Á. Havasi, I. Lagzi, and R. Mészáros (2014). "Dispersion Modeling of Air Pollutants in the Atmosphere: A Review". In: *Open Geosci.* 6.3, pp. 257–278. ISSN: 2391-5447. DOI: 10.2478/s13533-012-0188-6 (cit. on pp. 23, 24).

Lenschow, D. H., J. C. Wyngaard, and W. T. Pennell (1980). "Mean-Field and Second-Moment Budgets in a Baroclinic, Convective Boundary Layer". In: *Journal of Atmospheric Sciences* 37.6, pp. 1313–1326. ISSN: 0022-4928. DOI: 10.1175/1520-0469(1980)037<1313:Mfasmb>2.0.Co;2 (cit. on p. 74).

Lilly, D. K. (1983). "Stratified Turbulence and the Mesoscale Variability of the Atmosphere". In: *Journal of Atmospheric Sciences* 40.3, pp. 749–761. DOI: 10.1175/1520-0469(1983)040<0749:STATMV>2.0.CO;2 (cit. on p. 10).

Lin, J. C. (2013). "Lagrangian Modeling of the Atmosphere: An Introduction". In: *Lagrangian Modeling of the Atmosphere*. Ed. by J. Lin, D. Brunner, C. Gerbig, A. Stohl, A. Luhar, and P. Webley. Geophysical Monograph Series. Washington, DC: American Geophysical Union, pp. 1–11. ISBN: 0875904904. DOI: 10.1029/2012GM001376 (cit. on pp. 24, 25).

Lin, J. C., C. Gerbig, S. C. Wofsy, A. E. Andrews, B. C. Daube, K. J. Davis, and C. A. Grainger (2003). "A Near-Field Tool for Simulating the Upstream Influence of Atmospheric Observations: The Stochastic Time-Inverted Lagrangian Transport (STILT) Model". In: *J. Geophys. Res.-Atmos.* 108.D16. ISSN: 0148-0227. DOI: 10.1029/2002JD003161 (cit. on pp. 22, 26, 29).

Lin, J. C. and C. Gerbig (2013). "How can we satisfy the well-mixed criterion in highly inhomogeneous flows? A practical approach". In: *Lagrangian Modeling of the Atmosphere*. Ed. by J. Lin, D. Brunner, C. Gerbig, A. Stohl, A. Luhar, and P. Webley. Geophysical Monograph Series. Washington, DC: American Geophysical Union, pp. 59–70. ISBN: 0875904904. DOI: 10.1029/2012GM001232 (cit. on pp. 26, 27, 73).

Lin, W., L. Chen, W. Yu, H. Ma, Z. Zeng, J. Lin, and S. Zeng (2015). "Radioactivity Impacts of the Fukushima Nuclear Accident on the Atmosphere". In: *Atmos. Environ.* 102, pp. 311–322. ISSN: 1352-2310. DOI: 10.1016/j.atmosenv.2014.11.047 (cit. on pp. 8, 22).

Link, K. G., M. T. Stobb, J. Di Paola, K. B. Neeves, A. L. Fogelson, S. S. Sindi, and K. Leiderman (2018). "A Local and Global Sensitivity Analysis of a Mathematical Model of Coagulation and Platelet Deposition Under Flow". In: *PLOS ONE* 13.7, pp. 1–38. DOI: 10.1371/journal.pone.0200917 (cit. on p. 56).

Luhar, A. K. (2013). "Lagrangian Particle Modeling of Dispersion in Light Winds". In: *Lagrangian Modeling of the Atmosphere*. Ed. by J. Lin, D. Brunner, C. Gerbig, A. Stohl, A. Luhar, and P. Webley. Geophysical Monograph Series.

Washington, DC: American Geophysical Union, pp. 37–51. ISBN: 0875904904. DOI: 10.1029/2012GM001264 (cit. on p. 25).

Luhar, A. K. and R. E. Britter (1989). "A Random Walk Model for Dispersion in Inhomogeneous Turbulence in a Convective Boundary Layer". In: *Atmos. Environ.* 23.9, pp. 1911–1924. ISSN: 0004-6981. DOI: 10.1016/0004-6981(89)90516-7 (cit. on p. 76).

Luther, A., R. Kleinschek, L. Scheidweiler, S. Defratyka, M. Stanisavljevic, A. Forstmaier, A. Dandocsi, S. Wolff, D. Dubravica, N. Wildmann, J. Kostinek, P. Jöckel, A. L. Nickl, T. Klausner, F. Hase, M. Frey, J. Chen, F. Dietrich, J. Necki, J. Swolkień, A. Fix, A. Roiger, and A. Butz (2019). "Quantifying CH4 emissions from hard coal mines using mobile sun-viewing Fourier transform spectrometry". In: *Atmos. Meas. Tech.* 12.10, pp. 5217–5230. ISSN: 1867-8548. DOI: 10.5194/amt-12-5217-2019 (cit. on p. 88).

Martens, R., W. Bruecher, C. Richter, F. Sentuc, M. Sogalla, and H. Thielen (2012). *Extension and validation of ARTM (atmospheric radionuclide transportation model) for the application as dispersion calculation model in AVV (general administrative provision) and SBG (incident calculation bases); Erweiterung und Validierung von ARTM für den Einsatz als Ausbreitungsmodell in AVV und SBG*. Report. Gesellschaft für Anlagen- und Reaktorsicherheit mbH (GRS), Koeln (Germany) (cit. on p. 4).

Mayall, A. (2003). "Modelling the dispersion of radionuclides in the atmosphere". In: *Modelling Radioactivity in the Environment*. Ed. by E. Marian Scott. 1st. Vol. 4. Elsevier. Chap. 2, pp. 13–54 (cit. on p. 22).

Mazzeo, N. A. and L. E. Venegas (2008). "Design of an Air-Quality Surveillance System for Buenos Aires City Integrated by a NOx Monitoring Network and Atmospheric Dispersion Models". In: *Environ. Model. Assess.* 13.3, pp. 349–356. ISSN: 1573-2967. DOI: 10.1007/s10666-007-9101-y (cit. on p. 22).

Mesinger, F. and A. Arakawa (July 1976). *Numerical Methods Used In Atmospheric Models*. Report. World Meteorological Organization. URL: https://oceanrep.geomar.de/40278/1/Mesinger_ArakawaGARP.pdf (cit. on p. 39).

Monin, A. S. and A. M. Obukhov (1954). "Basic Laws of Turbulent Mixing in the Surface Layer of the Atmosphere". In: *Contrib. Geophys. Inst. Acad. Sci. USSR* 151.163, p. 187. URL: https://gibbs.science/teaching/efd/handouts/monin_obukhov_1954.pdf (cit. on p. 16).

Morio, J. (2011). "Global and Local Sensitivity Analysis Methods for a Physical System". In: *Eur. J. Phys.* 32.6, pp. 1577–1583. ISSN: 0143-0807 1361-6404. DOI: 10.1088/0143-0807/32/6/011 (cit. on pp. 54, 55).

Moses, H. and J. E. Carson (1968). "Stack Design Parameters Influencing Plume Rise". In: *JAPCA J. Air Waste Ma.* 18.7, pp. 454–457. ISSN: 0002-2470. DOI: 10.1080/00022470.1968.10469155 (cit. on p. 41).

Murith, C., H. Völkle, and O. Huber (1986). "Radioactivity measurements in the vicinity of Swiss nuclear power plants". In: *Nucl. Instrum. Meth. A* 243.2, pp. 549–560. ISSN: 0168-9002. DOI: 10.1016/0168-9002(86)90994-0 (cit. on p. 22).

Oertel, H. j. and L. Prandtl (2017). *Prandtl - Führer durch die Strömungslehre : Grundlagen und Phänomene*. 14. Auflage. Springer Reference Technik. Wiesbaden: Springer Vieweg. ISBN: 978-3-658-08626-8. DOI: 10.1007/978-3-658-08627-5 (cit. on p. 13).

Oettl, D. (2015). "A multiscale modelling methodology applicable for regulatory purposes taking into account effects of complex terrain and buildings on pollutant dispersion: a case study for an inner Alpine basin". In: *Environ. Sci. Pollut. R.* 22.22, pp. 17860–17875. ISSN: 1614-7499. DOI: 10.1007/s11356-015-4966-9 (cit. on p. 29).

Ohera, M., E. Fiala, and J. Valasek (1993). "The Use of Thermoluminescence Dosemeters for Determining Doses in the Vicinity of the Dukovany Nuclear Power Plant". In: *Radiat. Prot. Dosim.* 46.3, pp. 189–194. ISSN: 0144-8420. DOI: 10.1093/oxfordjournals.rpd.a081674 (cit. on p. 22).

Panofsky, H. A., H. Tennekes, D. H. Lenschow, and J. C. Wyngaard (1977). "The Characteristics of Turbulent Velocity Components in the Surface Layer Under Convective Conditions". In: *Bound.-Lay. Meteorol.* 11.3, pp. 355–361. ISSN: 1573-1472. DOI: 10.1007/BF02186086 (cit. on pp. 4, 74).

Pasquill, F. (1961). "The estimation of the dispersion of windborne material". In: *Meteoro. Mag.* 90, pp. 20–49 (cit. on p. 20).

Pisso, I., E. Sollum, H. Grythe, N. I. Kristiansen, M. Cassiani, S. Eckhardt, D. Arnold, D. Morton, R. L. Thompson, C. D. Groot Zwaaftink, N. Evangeliou, H. Sodemann, L. Haimberger, S. Henne, D. Brunner, J. F. Burkhart, A. Fouilloux, J. Brioude, A. Philipp, P. Seibert, and A. Stohl (2019). "The Lagrangian particle dispersion model FLEXPART version 10.4". In: *Geosci. Model Dev.* 12.12, pp. 4955–4997. ISSN: 1991-9603. DOI: 10.5194/gmd-12-4955-2019 (cit. on p. 26).

Plischke, E., E. Borgonovo, and C. L. Smith (2013). "Global Sensitivity Measures from Given Data". In: *Eur. J. Oper. Res.* 226.3, pp. 536–550. ISSN: 0377-2217. DOI: 10.1016/j.ejor.2012.11.047 (cit. on p. 57).

Prandtl, L. (1925). "7. Bericht über Untersuchungen zur ausgebildeten Turbulenz". In: *Z. Angew. Math. Mech.* 5.2, pp. 136–139. ISSN: 0044-2267. DOI: 10.1002/zamm.19250050212 (cit. on p. 14).

Press, W. H., S. A. Teukolsky, W. T. Vetterling, and B. P. Flannery (2002). *Numerical Recipes in C: The Art of Scientific Computing*. 2nd ed. Cambridge University Press. ISBN: 0-521-43108-5 (cit. on pp. 36, 47, 49).

Prusa, J. M., P. K. Smolarkiewicz, and A. A. Wyszogrodzki (2008). "EULAG, a computational model for multiscale flows". In: *Comput. Fluids* 37.9, pp. 1193–1207. ISSN: 0045-7930. DOI: 10.1016/j.compfluid.2007.12.001 (cit. on p. 109).

Pudykiewicz, J. (1989). "Simulation of the Chernobyl dispersion with a 3-D hemispheric tracer model". In: *Tellus B* 41.4, pp. 391–412. DOI: 10.3402/tellusb.v41i4.15096 (cit. on p. 21).

Ragland, K. W. (1973). "Multiple Box Model for Dispersion of Air Pollutants from Area Sources". In: *Atmos. Environ.* 7.11, pp. 1017–1032. ISSN: 0004-6981. DOI: 10.1016/0004-6981(73)90213-8 (cit. on p. 17).

Rao, K. S. (2005). "Uncertainty Analysis in Atmospheric Dispersion Modeling". In: *Pure Appl. Geophys.* 162.10, pp. 1893–1917. ISSN: 0033-4553-1420-9136. DOI: 10.1007/s00024-005-2697-4 (cit. on pp. 27, 54).

Ratto, C. F. (1996). "An Overview of Mass-Consistent Models". In: *Modelling of Atmospheric Flow Fields*. Ed. by D. Lalas and C. F. Ratto. Singapore: World Scientific Publishing Co Pte Ltd, pp. 379–400. ISBN: 9810225091 (cit. on pp. 35, 37, 38).

Ratto, C. F., R. Festa, C. Romeo, O. A. Frumento, and M. Galluzzi (1994). "Mass-Consistent Models for Wind Fields Over Complex Terrain: The State of the Art". In: *Environ. Softw.* 9.4, pp. 247–268. ISSN: 0266-9838. DOI: 10.1016/0266-9838(94)90023-X (cit. on pp. 34–36, 38).

Reynolds, O. (1895). "IV. On the Dynamical Theory of Incompressible Viscous Fluids and the Determination of the Criterion". In: *Philos. T. Roy. Soc. A* 186, pp. 123–164. DOI: 10.1098/rsta.1895.0004 (cit. on p. 10).

Reynolds, S. D., P. M. Roth, and J. H. Seinfeld (1973). "Mathematical modeling of photochemical air pollution—I: Formulation of the model". In: *Atmos Environ* 7.11, pp. 1033–1061. ISSN: 0004-6981. DOI: 10.1016/0004-6981(73)90214-X (cit. on p. 20).

Richardson, L. F. (1922). *Weather Prediction by Numerical Process*. 1st ed. London: Cambridge University Press. URL: https://archive.org/details/weatherpredictio00richrich/weatherpredictio00richrich/ (cit. on p. 20).

Richter, C., M. Sogalla, H. Thielen, and R. Martens (2015a). *ARTM Atmosphärisches Radionuklid-Transport-Modell mit Radon Prozessor und SBG-Modul. Modellbeschreibung zu Version 2.8.0*. Köln: Gesellschaft für Anlagen- und Reaktorsicherheit (GRS) mbH (cit. on pp. 31, 32, 39, 44–47).

— (2015b). *Atmosphärisches Radionuklid-Transport-Modell mit der graphischen Benutzeroberfläche GO-ARTM. Programmbeschreibung zu Version 2.8.0 (GO-ARTM Version 2.0)*. Köln: Gesellschaft für Anlagen- und Reaktorsicherheit (GRS) mbH (cit. on pp. 30, 35, 36, 43, 59).

Richter, C., H. Thielen, K. Spieker, and A. Günther (2020). *ARTM Atmosphärisches Radionuclid-Transport-Modell mit graphischer Benutzeroberfläche GO-ARTM. Handbuchzu Version 3.0.0 (GO-ARTM Version 2.0)*. Köln: Gesellschaft für Anlagen- und Reaktorsicherheit (GRS) gGmbH (cit. on p. 32).

Ryall, D. B. and R. H. Maryon (1998). "Validation of the UK Met. Office's NAME Model Against the ETEX Dataset". In: *Atmos. Environ.* 32.24, pp. 4265–4276. ISSN: 1352-2310. DOI: 10.1016/S1352-2310(98)00177-0 (cit. on pp. 21, 29).

Saltelli, A., M. Ratto, T. Andres, F. Campolongo, J. Cariboni, D. Gatelli, M. Saisana, and S. Tarantola (2008). *Global Sensitivity Snalysis: the Primer*. Chichester: John Wiley & Sons, Ltd. ISBN: 0470725176 (cit. on pp. 27, 53, 54, 56, 57, 69).

Sasaki, Y. (1958). "An Objective Analysis Based on the Variational Method". In: *J. Meteorol. Soc. Jap. Ser. II* 36.3, pp. 77–88. DOI: 10.2151/jmsj1923.36.3_77 (cit. on p. 35).

— (1970). "Some Basic Formalisms in Numerical Variational Analysis". In: *Mon. Weather Rev.* 98.12, pp. 875–883. ISSN: 0027-0644. DOI: 10.1175/1520-0493(1970)098<0875:sbfinv>2.3.co;2 (cit. on p. 35).

Sato, Y., T. T. Sekiyama, S. Fang, M. Kajino, A. Quérel, D. Quélo, H. Kondo, H. Terada, M. Kadowaki, M. Takigawa, Y. Morino, J. Uchida, D. Goto, and H. Yamazawa (2020). "A model intercomparison of atmospheric 137Cs concentrations from the Fukushima Daiichi Nuclear Power Plant accident, phase III: Simulation with an identical source term and meteorological field at 1-km resolution". In: *Atmos. Environ. X* 7, p. 100086. ISSN: 2590-1621. DOI: 10.1016/j.aeaoa.2020.100086 (cit. on p. 22).

Sawford, B. L. (1986). "Generalized random forcing in random-walk turbulent dispersion models". In: *Phys. Fluids* 29.11, pp. 3582–3585. DOI: 10.1063/1.865784 (cit. on p. 27).

Schmidt, W. (1925). *Der Massenaustausch in freier Luft und verwandte Erscheinungen*. Vol. 7. Probleme in der Kosmischen Physik (cit. on p. 20).

Schorling, M. (1995). "Lagrangian dispersion model and its application to monitor nuclear power plants". In: *Environ. Sci. Pollut. Res. Int.* 2.2, pp. 105–6. ISSN: 0944-1344 (Print) 0944-1344 (Linking). DOI: 10.1007/BF02986731 (cit. on p. 22).

Schumann, U., B. Weinzierl, O. Reitebuch, H. Schlager, A. Minikin, C. Forster, R. Baumann, T. Sailer, K. Graf, H. Mannstein, C. Voigt, S. Rahm, R. Simmet, M. Scheibe, M. Lichtenstern, P. Stock, H. Rüba, D. Schäuble, A. Tafferner, M. Rautenhaus, T. Gerz, H. Ziereis, M. Krautstrunk, C. Mallaun, J. F. Gayet, K. Lieke, K. Kandler, M. Ebert, S. Weinbruch, A. Stohl, J. Gasteiger, S. Groß, V. Freudenthaler, M. Wiegner, A. Ansmann, M. Tesche, H. Olafsson, and K. Sturm (2011). "Airborne Observations of the Eyjafjalla Volcano Ash Cloud

Over Europe During Air Space Closure in April and May 2010". In: *Atmos. Chem. Phys.* 11.5, pp. 2245–2279. ISSN: 1680-7324. DOI: 10.5194/acp-11-2245-2011 (cit. on p. 21).

Seibert, P. and A. Frank (2004). "Source-receptor matrix calculation with a Lagrangian particle dispersion model in backward mode". In: *Atmos. Chem. Phys.* 4.1, pp. 51–63. ISSN: 1680-7324. DOI: 10.5194/acp-4-51-2004 (cit. on p. 22).

Seinfeld, J. H. (1986). *Atmospheric Chemistry and Physics of Air Pollution*. New York: John Wiley & Sons. ISBN: 0-471-82857-2 (cit. on p. 31).

Seinfeld, J. H. and S. N. Pandis (2016). *Atmospheric Chemistry and Physics: From Air Pollution to Climate Change*. Vol. 3. Hoboken: John Wiley & Sons. ISBN: 9781119221166 (cit. on p. 9).

Sheridan, B. A., E. T. Hayes, T. P. Curran, and V. A. Dodd (2004). "A dispersion modelling approach to determining the odour impact of intensive pig production units in Ireland". In: *Bioresource Technol.* 91.2, pp. 145–152. ISSN: 0960-8524. DOI: 10.1016/S0960-8524(03)00179-2 (cit. on p. 21).

Sherman, C. A. (1978). "A Mass-Consistent Model for Wind Fields Over Complex Terrain". In: *J. Appl. Meteorol.* 17.3, pp. 312–319. ISSN: 0021-8952. URL: https://www.jstor.org/stable/26178005 (cit. on pp. 35–37).

Sierk, B., V. Fernandez, J.-L. Bézy, Y. Meijer, Y. Durand, G. Bazalgette Courrèges-Lacoste, C. Pachot, A. Löscher, H. Nett, K. Minoglou, L. Boucher, R. Windpassinger, A. Pasquet, D. Serre, and F. te Hennepe (2021). *The Copernicus CO2M mission for monitoring anthropogenic carbon dioxide emissions from space*. Vol. 11852. International Conference on Space Optics — ICSO 2021. SPIE. DOI: 10.1117/12.2599613 (cit. on p. 113).

Simmonds, J., G. Lawson, and A. Mayall (1995). *Methodology for assessing the radiological consequences of routine releases of radionuclides to the environment*. Report. National Radiological Protection Board (UK). URL: https://op.europa.eu/en/publication-detail/-/publication/1078584c-9e21-40d1-9104-82939f315f25 (cit. on pp. 21, 22).

SkyscraperPage (2023). *Drawing of Belchatow Power Station Units 1-6*. Skyscraper Source Media. URL: https://skyscraperpage.com/diagrams/?buildingID=6131. last access 4 October 2003 (cit. on p. 92).

Slade David, H. (July 1968). *Meteorology and Atomic Energy 1968*. Report. Air Resources Laboratories. DOI: 10.2172/4492043 (cit. on p. 21).

Smith, J., A. Bexon, F. Boyer, M. Harvey, A. Jones, T. Kindler, J. Mercer, S. Haywood, N. Verhoef, B. Hverkante, and A. Artmann (2002). *Assessment of the Radiological Impact on the Population of the European Union of Discharges from European Union Nuclear Sites between 1987 and 1996*. Report. European Commission. URL: https://energy.ec.europa.eu/system/files/2014-11/128_1.pdf (cit. on p. 22).

Sobol', I. M. (1993). "Sensitivity Estimates for Nonlinear Mathematical Models". In: *Math. Model. Comput. Experim.* 4, pp. 407–414 (cit. on p. 56).

Sørensen, J. H., C. Ø. Jensen, T. Mikkelsen, D. K. J. Mackay, and A. I. Donaldson (2001). "Modelling the atmospheric dispersion of foot-and-mouth disease virus for emergency preparedness". In: *Phys. Chem. Earth. Pt. B* 26.2, pp. 93–97. ISSN: 1464-1909. DOI: 10.1016/S1464-1909(00)00223-9 (cit. on p. 21).

Stockie, J. M. (2011). "The Mathematics of Atmospheric Dispersion Modeling". In: *SIAM Review* 53.2, pp. 349–372. ISSN: 0036-1445. DOI: 10.1137/10080991X (cit. on p. 19).

Stohl, A., C. Forster, A. Frank, P. Seibert, and G. Wotawa (2005). "Technical note: The Lagrangian particle dispersion model FLEXPART version 6.2". In: *Atmos. Chem. Phys.* 5.9, pp. 2461–2474. ISSN: 1680-7324. DOI: 10.5194/acp-5-2461-2005 (cit. on pp. 21, 29, 76).

Stohl, A., A. J. Prata, S. Eckhardt, L. Clarisse, A. Durant, S. Henne, N. I. Kristiansen, A. Minikin, U. Schumann, P. Seibert, K. Stebel, H. E. Thomas, T. Thorsteinsson, K. Tørseth, and B. Weinzierl (2011). "Determination of Time- and Height-Resolved Volcanic Ash Emissions and their Use for Quantitative Ash Dispersion Modeling: the 2010 Eyjafjallajökull Eruption". In: *Atmos. Chem. Phys.* 11.9, pp. 4333–4351. ISSN: 1680-7324. DOI: 10.5194/acp-11-4333-2011 (cit. on p. 21).

StrlSchV (29.11.2018 2018). *Verordnung zum Schutz vor der schädlichen Wirkung ionisierender Strahlung (Strahlenschutzverordnung - StrlSchV)*. URL: http://www.gesetze-im-internet.de/strlschv_2018/StrlSchV.pdf (cit. on pp. 21, 22).

Stull, R. B. (1988). *An Introduction to Boundary Layer Meteorology*. Vol. 13. Atmospheric Sciences Library. Dordrecht: Kluwer. ISBN: 9027727686. DOI: 10.1007/978-94-009-3027-8 (cit. on pp. 8, 10, 11, 13, 15, 31, 77).

— (2006). "The Atmospheric Boundary Layer". In: *Atmospheric Science An Introductory Survey*. Ed. by R. Dmowska, D. Hartmann, and H. T. Rossby. 2nd ed. London: Elseveir Inc. Chap. 9, pp. 375–417. ISBN: 9780-1273-2951-2 (cit. on pp. 8–11).

Sutton, O. G. (1947a). "The problem of diffusion in the lower atmosphere". In: *Q. J. Roy. Meteor. Soc.* 73.317-318, pp. 257–281. ISSN: 0035-9009. DOI: 10.1002/qj.49707331704 (cit. on p. 20).

— (1947b). "The theoretical distribution of airborne pollution from factory chimneys". In: *Q. J. Roy. Meteor. Soc.* 73.317-318, pp. 426–436. ISSN: 0035-9009. DOI: 10.1002/qj.49707331715 (cit. on p. 20).

Sutton, O. G. and G. C. Simpson (1932). "A theory of eddy diffusion in the atmosphere". In: *P. R. Soc. Lond. A-Conta* 135.826, pp. 143–165. DOI: 10.1098/rspa.1932.0025 (cit. on p. 20).

Sutton, O. G. and G. C. Simpson (1934). "Wind structure and evaporation in a turbulent atmosphere". In: *Proc R Soc Lond* 146.858, pp. 701–722. DOI: 10.1098/rspa.1934.0183 (cit. on p. 20).

TA Luft (2002). *Erste Allgemeine Verwaltungsvorschrift zum Bundes-Immissionsschutzgesetz (Technische Anleitung zur Reinhaltung der Luft–TA Luft). Technical Instruction on Air Quality*. Government Document. Bundesministerium für Umwelt, Naturschutz und Reaktorsicherheit (cit. on pp. 31, 33, 59, 60, 91, 92).

Taylor, G. I. (1921). "Diffusion by Continuous Movements". In: *P. Lond. Math. Soc.* s2-20.1, pp. 196–212. ISSN: 0024-6115. DOI: 10.1112/plms/s2-20.1.196 (cit. on p. 20).

Taylor, G. I. and W. N. Shaw (1915). "I. Eddy motion in the atmosphere". In: *Philos T R Soc Lond* 215.523-537, pp. 1–26. DOI: 10.1098/rsta.1915.0001 (cit. on p. 20).

Taylor, J. R. (1997). *An Introduction to Error Analysis*. 2nd ed. Sausalito, California: University Science Books. ISBN: 0-935702-42-3 (cit. on pp. 47–49).

Thaning, L. and A. Baklanov (1997). "Simulation of the atmospheric transport and deposition on a local/meso- and regional scale after hypothetical accidents at the Kola nuclear power plant". In: *Sci Total Environ* 202.1, pp. 199–210. ISSN: 0048-9697. DOI: 10.1016/S0048-9697(97)00116-2 (cit. on p. 21).

Thomson, D. J. (1987). "Criteria for the selection of stochastic models of particle trajectories in turbulent flows". In: *J. Fluid Mech.* 180, pp. 529–556. ISSN: 0022-1120. DOI: 10.1017/S0022112087001940 (cit. on pp. 21, 25–27, 73).

Thomson, D. J. and J. D. Wilson (2012). "History of Lagrangian Stochastic Models for Turbulent Dispersion". In: *Lagrangian Modeling of the Atmosphere*. Geophysical Monograph Series, pp. 19–36. ISBN: 9781118704578. DOI: 10.1029/2012GM001238 (cit. on p. 20).

Thykier-Nielsen, S., S. Deme, and T. Mikkelsen (Apr. 1999). *Description of the Atmospheric Dispersion Module RIMPUFF*. Report. Risø National Laboratory. URL: https://www.researchgate.net/publication/228741276_Description_of_the_atmospheric_dispersion_module_RIMPUFF (cit. on p. 96).

Trini Castelli, S., P. Armand, G. Tinarelli, C. Duchenne, and M. Nibart (2018). "Validation of a Lagrangian Particle Dispersion Model with Wind Tunnel and Field Experiments in Urban Environment". In: *Atmos. Environ.* 193, pp. 273–289. ISSN: 1352-2310. DOI: 10.1016/j.atmosenv.2018.08.045 (cit. on p. 26).

Turner, D. B. (1964). "A diffusion model for an urban area". In: *J. Appl. Meteorol. Clim.* 3.1, pp. 83–91. ISSN: 0021-8952. DOI: 10.1175/1520-0450(1964)003<0083:ADMFAU>2.0.CO;2 (cit. on pp. 20, 23).

University of Oregon (2020). *Comparing Distributions: Z Test*. URL: http://homework.uoregon.edu/pub/class/es202/ztest.html. last access 23 Nov. 2022 (cit. on p. 106).

Van der Hoven, I. (1957). "Power Spectrum of Horizontal Wind Speed in the Frequency Range From 0.0007 to 900 Cycles Per Hour". In: *J. Atmos. Sci.* 14.2, pp. 160–164. ISSN: 0095-9634. DOI: 10.1175/1520-0469(1957)014<0160:Psohws>2.0.Co;2 (cit. on p. 11).

Varon, D. J., D. J. Jacob, J. McKeever, D. Jervis, B. O. A. Durak, Y. Xia, and Y. Huang (2018). "Quantifying methane point sources from fine-scale satellite observations of atmospheric methane plumes". In: *Atmos. Meas. Tech.* 11.10, pp. 5673–5686. ISSN: 1867-8548. DOI: 10.5194/amt-11-5673-2018 (cit. on p. 115).

VDI 3782 part 3 (1985). *Berechnung der Abgasfahnenüberhöhung*. Determination of Plume Rise. VDI-Handbuch Reinhaltung der Luft, Band 1. Verein Deutscher Ingenieure, URL: https://www.beuth.de/de/technische-regel/vdi-3782-blatt-3/635897. VDI 3782 Blatt 3 (cit. on pp. 39, 41, 42).

VDI 3783 part 8 (Dec. 2002). *Messwertgestützte Turbulenzparametrisierung für Ausbreitungsmodelle. Umweltmeteorologie*. Turbulent parameters for dispersion models supported by measurement data. VDI-Handbuch Reinhaltung der Luft, Band 1b. Verein Deutscher Ingenieure, URL: https://www.beuth.de/de/technische-regel/vdi-3783-blatt-8/59262605. VDI 3783 Blatt 8 (cit. on pp. 4, 31, 33, 34, 62, 74, 111).

— (Apr. 2017). *Messwertgestützte Turbulenzparametrisierung für Ausbreitungsmodelle. Umweltmeteorologie*. Turbulence parameters for dispersion models supported by measurement data. VDI-Handbuch Reinhaltung der Luft, Band 1b. Verein Deutscher Ingenieure, URL: https://www.beuth.de/de/technische-regel/vdi-3783-blatt-8/261571914?websource=vdin. VDI 3783 Blatt 8 (cit. on pp. 4, 60, 73, 76, 77).

VDI 3945 part 3 (Sept. 2000). *Atmosphärische Ausbreitungsmodelle - Partikelmodell. Umweltmeteorologie*. Atmospheric dispersion models - Particle model. VDI/DIN-Handbuch Reinhaltung der Luft, Band 1b. Verein Deutscher Ingenieure. URL: https://www.beuth.de/de/technische-regel/vdi-3945-blatt-3/36552631. VDI 3945 Blatt 3 (cit. on pp. 39, 40, 42–45).

WHO (2022). *Air pollution*. World Health Organisation. URL: https://www.who.int/health-topics/air-pollution#tab=tab_1. last access 3 April 2023 (cit. on p. 19).

Wilks, D. S. (2006). *Statistical Methods in the Atmospheric Sciences*. 2nd ed. Vol. 91. International Geophysics Series. Amsterdam: Elsevier. ISBN: 978-0-12-751966-1 (cit. on p. 106).

Wilson, J. D. and B. L. Sawford (1996). "Review of Lagrangian Stochastic Models for Trajectories in the Turbulent Atmosphere". In: *Bound.-Lay. Meteorol.* 78.1, pp. 191–210. ISSN: 1573-1472. DOI: 10.1007/BF00122492 (cit. on p. 26).

Wolff, S., G. Ehret, C. Kiemle, A. Amediek, M. Quatrevalet, M. Wirth, and A. Fix (2021). "Determination of the emission rates of CO2 point sources with airborne lidar". In: *Atmos. Meas. Tech.* 14.4, pp. 2717–2736. ISSN: 1867-8548. DOI: 10.5194/amt-14-2717-2021 (cit. on pp. 88, 109).

Zagayevskiy, Y. and C. V. Deutsch (2015). "A Methodology for Sensitivity Analysis Based on Regression: Applications to Handle Uncertainty in Natural Resources Characterization". In: *Nat. Resour. Res.* 24.3, pp. 239–274. ISSN: 1573-8981. DOI: 10.1007/s11053-014-9241-0 (cit. on p. 54).

Zannetti, P. (1991). *Air Pollution Modeling : Theories, Computational Methods and Available Software*. New York, NY: Springer. ISBN: 978-1-4757-4465-1. DOI: 10.1007/978-1-4757-4465-1 (cit. on pp. 23, 24).

Declaration of authenticity

I hereby declare that I wrote the submitted dissertation without any unauthorized external assistance and used only sources acknowledged in the work. All textual passages taken verbatim or paraphrased from published and unpublished texts are appropriately indicated and listed in accordance with bibliographical rules. In carrying out this research, I complied with the rules of standard scientific practice as formulated in the statutes of Johannes Gutenberg-University Mainz to insure standard scientific practice. This dissertation or parts of it have never been previously submitted in its current or similar form as part in any other qualification.

Author contributions

In this dissertation, I derived the detailed description of the physical and mathematical concepts of the ARTM dispersion model based on the source code and the manual of version 2.8.0. The source code has been written by GRS and is based on AUSTAL2000. In chapter 3, I gave a description of ARTM model version 2.8.0 and compare to 3.0.0.

I further planed and performed the sensitivity analysis presented in chapter 4.1. This includes the preparation and performing of the necessary simulations, the review of literature for appropriate evaluation methods and the evaluation of the simulation results using evaluation toolsets. For the study of the mixing properties of different turbulence models in chapter 4.2, I reviewed the literature and implemented two additional turbulence models to ARTM. I planned, performed and evaluated the simulations that were necessary to analyse the mixing abilities of the models according to the well-mixed criterion.

The comparison of the ARTM simulations using the five different turbulence models presented in chapter 5.1 was planned, performed and evaluated by me. This includes the preparation and derivation of input parameters from the measurement data. The measurement data were collected and provided by Alina Fiehn and Anke Roiger.

The intercomparison of six atmospheric transport models, including ARTM, in chapter 5.2 was chaired by Dominik Brunner. All participants collaborated on the modelling protocol. According to this protocol I carried out the ARTM simulations, provided the ARTM results to the study and contributed to the interpretation of the results.

Acknowledgments/Danksagung

The Acknowlegements are removed from the electronic version of this thesis due to privacy policy laws.

Curriculum vitae/Lebenslauf

The curriculum vitae is removed from this electronic version of the thesis due to privacy policy laws.

The curriculum vitae is removed from this electronic version of the thesis due to privacy policy laws.